School of Physics and Astronomy

Laser machining of strain defects to control excitons in cuprous oxide

Sam Gavin-Pitt

School of Physics and Astronomy
Cardiff University

June 24, 2025

Contents

Summary of thesis

The purpose of this project was to investigate the feasibility of infrared picosecond laser machining of cuprous oxide (Cu_2O) by two-photon absorption and to determine the effects that this has on its optical properties, specifically those of its excitons.

Machining was achieved for pulse energies exceeding 0.4 µJ for mid-sample-only machining, and 0.2 µJ for machining on the surface. The latter was invariably found to occur much more readily than the former. SEM images of the damage revealed evidence of laser filamentation due to nonlinear self-focusing which is known to result in multi-photon absorption - the absorption mechanism for laser machining. The filament-like damage extended through to depths within the samples on the scale of 10s of µm and demonstrated widths as low as 30 nm. SEM images of the surface effects of laser machining show apparent sample melting which is consistent with the energy of the laser pulses given the volume of melted material. Shifts in the exciton absorption peaks (on the scale of 10s of µeV), and the introduction of birefringence in the crystal both occurred anisotropically in the material surrounding the machinings suggesting the presence of an asymmetric strain field caused by the damage. The phase difference induced by birefringence was indicative of a shift in the refractive index of the material of up to about $\Delta n = 2 \times 10^{-3}$. Raman spectrometry revealed an increase in the presence of split copper vacancies (or Cu_3O_2) in the material surrounding the damage as evidenced by changes in the Raman activity and photoluminescence. The damage absorbed light for a broad range of frequencies, though transmission imaging of the machinings showed that the most significant change in transmission was not this absorption and was attributed to variations in n surrounding the damage or increased scattering due to surface damage.

Acknowledgements

The greatest thanks goes to my supervisor, Wolfgang Langbein, whose guidance and expertise have been vital to me throughout this project. Special thanks go to Chris Hodges, Vikram Singh and, from our partner group in Durham, Liam Gallagher and Jon Pritchett all of whom have given their time to assist me practically. Thanks also to Stephen Lynch, Matt Jones, and Freeke van de Voort for their help and encouragement. Finally, thank-you to Anesha Hamood whose significant support did not go unrecognised.

Chapter 1

Introduction

As the physics of semiconductors was becoming better understood from early to mid-20$^{\text{th}}$ century, one of the very first materials that was used in semiconductor electronics was cuprous oxide (Cu_2O) [1]. As other semiconductors like silicon (Si) and gallium arsenide (GaAs) grew in popularity due to their use in the booming world of electronics, the research into other materials, like Cu_2O, was sidelined. More recently, however, the spotlight has begun to swing in Cu_2O's favour as it attracts interest for a variety of potential applications. For example, it can be used in gas sensing [2], and in the field of solar energy it is being investigated for use both in photovoltaic cells [3, 4, 5] (given that its band gap is about twice that of silicon and thus tandem cells can create higher efficiencies) and as a photocatalyst [6] (for example, in water splitting [7]). But arguably the greatest attraction of Cu_2O is its excitons which are not only an area of great interest in the field of Bose-Einstein condensates [8, 9], but demonstrate desirable properties described by Rydberg physics; a branch traditionally associated with atomic physics. Atomic Rydberg systems have shown promise in quantum information processing, cavity quantum electrodynamics (QED), many-body experiments [10, 11], and various photonics and optoelectronics devices such as quantum gates and optical switches [12, 13]. If Rydberg excitons can be used in the same way as Rydberg atoms, these functionalities could be integrated into advancing semiconductor photonics technologies [14, 15].

One property of Rydberg atoms that has made them so useful in the aforementioned technologies is the huge radius of the electrons when in high-n Rydberg states which can be on the scale of microns [16]. This makes Rydberg atoms in such states highly polarizable due to large induced dipole moments making them capable of long-range interactions and very sensitive to electromagnetic fields [15] making them useful as probes for detecting weak electric fields [17, 18, 19]. Furthermore, dipole-dipole interaction between atoms results in very strong optical nonlinearities since excited Rydberg atoms shift the energy of nearby atomic Rydberg states such that the linewidth of an excitation source is not broad enough to resonantly excite Rydberg states of other atoms in the vicinity. This is a phenomenon called the Rydberg blockade and results in local transparency of the medium at the excitation wavelength called

electromagnetically induced transparency (EIT) [20]. This optical nonlinearity is so strong that it is evident even at the single-photon level, opening the door to single-photon switches and transistors [12] and allows for the mediation of photon-photon interactions essential for quantum information processing [11].

Excitons are quasiparticles found in semiconductors; in fact, they were first discovered in Cu_2O [21, 22, 23]. The nature of semiconductors is such that, at room temperature, there is sufficient probability of electrons being promoted due to thermal energy in the system from a filled valence band to an empty conduction band to significantly increase the material conductivity above the level of an insulator. The probability of thermal excitation is scales as $\exp(-E_g/2k_BT)$ where E_g is the energy across the band gap, k_B is the Boltzmann constant, and T is the temperature. At room temperature, this gives $E_T = 26\,\text{meV}$ which is well below the band gap and is therefore why the material does not behave as a conductor. This creates charge carriers in the conduction band - the promoted electrons - but also in the valence band in the form of unfilled electron states, the holes, which are positively charged. An electron and a hole interact by the Coulomb interaction and a hydrogen-like (a bound electron-hole pair) state called an exciton exists. Like hydrogen atoms, excitons exhibit Rydberg energy series. Excitons were first discovered in Cu_2O where they are more easily visible than in other materials due to its band structure which dipole-forbids optical transitions across the fundamental band gap (thus reducing the radiative line broadening of the exciton), a relatively high electron-hole binding energy (90 meV - for the Rydberg series of excitons - due to low relative permittivity and high effective masses of electrons and holes compared to other semiconductors). In Cu_2O, excitons with principal quantum numbers far surpassing anything seen in other semiconductors (n=30 as opposed to up to about 3 for e.g. GaAs [24]) have been observed [25] so it is no surprise that it is this material where exciton-based research is focused.

Excitons in Cu_2O with high principal quantum numbers also demonstrate radii of their wavefunctions on the micron scale [15, 26] and so, just as with Rydberg atoms, this results in large dipole moments, high sensitivity to electromagnetic fields, and strong optical nonlinearities at the few/single-photon level. Rydberg excitons therefore promise a union between the functionalities of Rydberg atoms and practical, solid-state semiconductor technologies, both bulk and low-dimensional [14, 15] which is scalable, compact, and with exciton properties that are tunable [27]. An essential step in achieving this is the local confinement of excitons [28] for which a number of approaches are being considered including reduced dimensionality (quantum wells [26] or dots [29]) and tailored structures (such as micropillars [27], microcrystals [30], and nanocrystals [28]). An additional possibility is to create a localised strain field within a bulk crystal to modify the band gap [31] and adequately confine the exciton. The purpose of this project was to create such strain fields using ultrashort laser pulses which have been shown to create very localised damage in other semiconductors sufficient to cause the desired strain [32, 33, 34, 35, 36, 37].

More specifically, this project aims to investigate how the properties of Cu_2O, and in particular the optical properties of its excitons, can be altered

and controlled using infrared, two-photon, picosecond laser machining. This machining has the benefit of being confined to the focal volume of the laser which allows for machining at freely chosen positions within the bulk Cu_2O which can be used for the creation of nanometre-scale optical structures [32, 38, 39]. Furthermore, the use of an infrared laser means that the sample is transparent at the laser's wavelength so that machining can be performed anywhere within the sample. For absorption to occur, a nonlinear, two-photon absorption must take place which requires high light intensities. This results in some sort of damage to the sample such as the formation of another material or a void exerting strain on the surrounding sample which is expected to result in alterations to the optical properties of the crystal and of its excitons.

In this project, both synthetic and natural samples of Cu_2O were laser machined using a 1064 nm laser with 30 ps pulses. Machining parameters such as laser pulse energy, laser polarization, sample thickness, focal point of the laser within the sample, defect concentration, and proximity to other machinings were varied and the changes in optical properties observed. Analysis techniques used include transmission microspectroscopy, transmission imaging, quantitative differential interference contrast (qDIC), Raman spectroscopy, and focused ion beam scanning electron microscopy (FIB-SEM).

Chapter 2 provides background going into detail regarding the optical properties of Cu_2O and its excitons. The process of laser machining will be described as well as further phenomena expected such as filamentation of the laser. Information on the samples and methods used is provided in Chapter 3. Chapter 4 describes the optical setup used for laser machining as well as for transmission microspectroscopy as these used the same optical arrangement. Specific details on the nature of the laser machining for each individual sample are also detailed here. Chapters 5 and 6 show the results of the analysis for non-excitonic and excitonic effects, respectively. The research and findings will then be summarised in Chapter 7.

Chapter 2

Background

2.1 Cuprous oxide

Cuprous Oxide (Cu_2O) is a compound semiconductor which occurs naturally as cuprite in the form of a red gemstone. It can also be grown synthetically [40, 41] as was the case for some of the samples used in this project, although synthetic samples tend to contain higher concentrations of defects than their best natural counterparts. Details of the specific growth method for these samples are included in Sec. 3.1.1. Cu_2O exhibits a cubic crystal structure with copper atoms arranged in a face-centred cubic lattice, and the oxygen atoms in a body-centred cubic lattice such that the copper atoms are coordinated with two adjacent oxygen atoms (see Fig. 2.1a).

The relevant part of the band structure of Cu_2O around the Brillouin zone centre, or Γ-point, is shown in Fig. 2.1b. It consists of two valence bands (VBs) and two conduction bands (CBs). Both valence bands originate from Cu d-orbital electrons and, given that this symmetry is not disturbed due to Cu_2O having a centrosymmetric, cubic crystal structure, are therefore even-parity states. They are separated by an energy of 0.134 eV due to spin-orbit coupling where the upper energy band shows Γ_7^+ symmetry whilst the lower band shows Γ_8^+ symmetry. The lowest conduction band originates from Cu s-orbitals and has symmetry of Γ_6^+ while the following conduction band originates from p-orbitals and shows Γ_8^- symmetry; they are separated by 0.45 eV. The bandgap, E_g, is therefore related to transitions between the Γ_7^+ and Γ_6^+ states with an energy of 2.17 eV. In order of increasing energy, the other gaps are at 2.304, 2.624, and 2.755 eV for $\Gamma_8^+ \rightarrow \Gamma_6^+$, $\Gamma_7^+ \rightarrow \Gamma_8^-$, and $\Gamma_8^+ \rightarrow \Gamma_8^-$, respectively, all of which are direct transitions (i.e. the VB maxima and CB minima lie at the same point in the Brillouin zone - the Γ-point). These energies correspond to yellow, green, blue, and violet coloured light and so the transitions are referred to as such. Only the violet transition involves a change in parity between the states and so is dipole-allowed whilst the other three are dipole-forbidden when only considering the electron Bloch function. However, excitons with p-type envelope functions have negative parity and so transitions to these exciton states become dipole allowed [15].

Excitons are formed due to the excitation of an electron from the valence

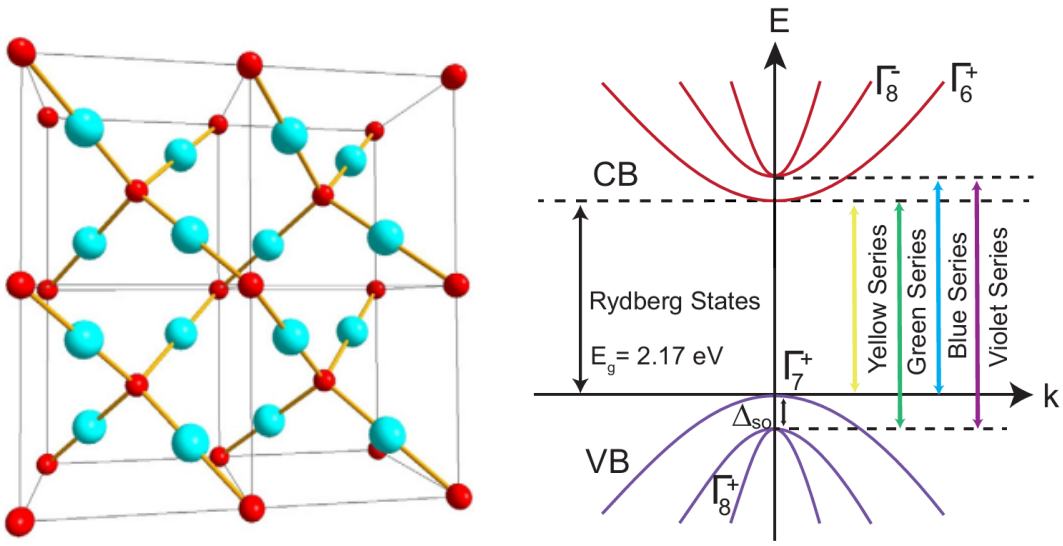

Figure 2.1: (a) Four unit cells of Cu_2O. The light blue spheres represent copper and the red are oxygen. [42] (b) The band structure at the Γ-point of Cu_2O. [43]

band to the conduction band which leaves behind a missing electron in the valence band which can be modelled as a positively charged particle - the so-called hole. The Coulomb attraction between the electron and the hole can bind them creating the exciton. The states of such a system involving a positive and negative charge bound by the Coulomb attraction is described by Rydberg physics (much like a hydrogen atom with a few changes from the hydrogen model due to differing effective masses) in which the energy of the state scales with the quantum number n according to:

$$E_n \; \alpha \; \frac{1}{n^2} \tag{2.1}$$

Although Rydberg physics is best understood within the context of atomic physics, it is applicable in any system with a Coulomb-bound electron [44], thus excitons in semiconductors also have a Rydberg series of energy levels. The energies of the states in a Rydberg series are given by:

$$E_n = \frac{E_{\text{Ryd}}}{(n - \delta_q)^2} \tag{2.2}$$

where E_n is the energy of the n^{th} state, E_{Ryd} is the Rydberg energy unique to the material, and δ_q is a so-called quantum defect - a correction term taking into account deviations from the model such as the frequency and wavelength dependence of the permittivity determining the screening of the Coulomb interaction inside the crystal, and a non-parabolic electron and hole band dispersion [44, 45]. This forms a series of excited states with energies below the band gap. Note that the excitons themselves exhibit a dispersion in their centre of mass motion (the states shown in Fig. 2.1b apply only to the Γ-point); this

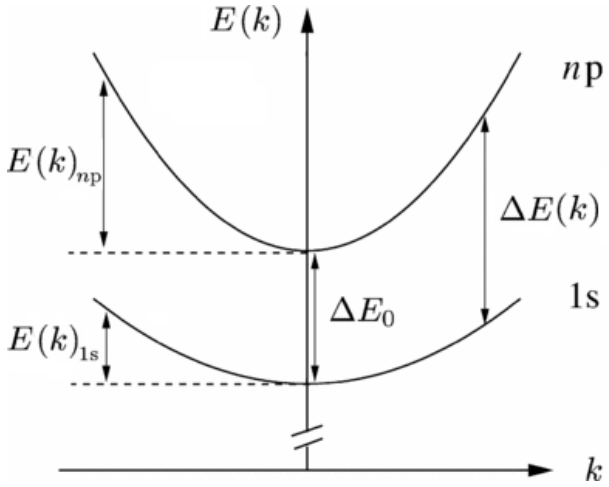

Figure 2.2: The k-dispersion of excitons. The dispersion of each state is inversely proportional to the effective mass. (Figure adapated from [46])

dispersion is shown in Fig. 2.2 and is described by:

$$E(k) = \frac{\hbar^2 k^2}{2m^*} \tag{2.3}$$

where $E(k)$ is the energy, k is the wavevector, and m^* is the effective mass of the exciton [46]. Excitons form for all VB→ CB band edges so that there are actually 4 series of transitions when also taking into account all of the possible exciton states. These series are referred to by the same colours as the transitions. Analysis in this project will focus on the yellow exciton series related to the band-gap transition.

Cu_2O was the first material in which excitons were observed [21, 22, 23], this was possible due to the high exciton stability (owing to high binding energy), the availability of high quality natural crystals, and the appearance of the exciton series in the visible light regime so that effects could be seen at visible wavelengths. Whereas exciton quantum numbers up to roughly $n = 3$ are typically detected for other semiconductors (e.g. GaAs [24]), excitons have been found in Cu_2O with quantum numbers up to $n = 30$ [25]. This is due, in part, to the high Rydberg energy of Cu_2O, but also to its band structure which forbids optical transitions to the lowest exciton energy (described in more detail shortly). The Rydberg energy (E_{Ryd}) is given by:

$$E_{\mathrm{Ryd}} = \frac{\mu e^4}{32(\epsilon_0 \epsilon_r \pi \hbar)^2} \tag{2.4}$$

where μ is the reduced mass and ϵ_r is the dielectric constant (or the relative permittivity). In the case of the Rydberg series in Cu_2O, this value is roughly 90 meV which is very high compared to a semiconductor like GaAs which has a Rydberg energy of just 4.2 meV [44]. This is due partly to having a high exciton reduced mass (μ), a quantity allowing a two-body system to be treated as a single mass according to $1/\mu = 1/m_e + 1/m_h$ where $m^*_{e,} = 0.99\, m_e$ and $m^*_h = 0.58\, m_e$ are electron and hole masses respectively (for Cu_2O, $\mu_{ex} =$

$0.366\,m_e$). Another contributor to the high E_{Ryd} of Cu_2O is its relatively low ϵ_r. For instance, the static dielectric constant, $\epsilon(0)$, of Cu_2O is 7.5 as opposed to that of GaAs which is 12.9 (their optical dielectric constants, $\epsilon(\infty)$, are 6.46 and 10.92, respectively) [15, 42, 47, 48, 49, 50]. These values of ϵ_r and μ alone are not sufficient to explain the high principal quantum numbers seen in Cu_2O excitons, however, since greater binding energies are seen in excitons in other materials without the same effect. For example, the 1s-exciton in CuCl has a reported binding energy of 131 meV [51] without showing the same effect. The unique band structure of Cu_2O must also be considered. In many semiconductors, the exciton states result in a bright, spectrally-broad emission due to exciton-polariton formation with high dispersion which can make other states difficult to detect. In Cu_2O, transitions to this state are parity-forbidden making the other higher-energy states much easier to detect due to narrower linewidths and the required breaking of the parity by the envelope function, suppressing the 1s-exciton compared to higher states [44]. Thermal ionization provides an upper limit ($n_{\max}$) to the principal quantum numbers that can be observed due to broadening of the exciton energies such that states above a certain number, $n_{\max}$ cannot be distinguished. This is given by [44]:

$$n_{max} \approx \sqrt{\frac{E_{\mathrm{Ryd}}}{k_B T}}\,. \tag{2.5}$$

Note that this does not take into account the quantum defect, δ_q. For a temperature of 6.5 K (the original temperature of the samples during laser machining in this project), this is equivalent to states up to $n = 12$ and for later sessions when the samples were cooled to 5 K, this increases to $n = 14$. In practice the highest quantum number seen is expected to be lower than this due to imperfections in the crystal structure.

An absorption spectrum of synthetic Cu_2O is shown in Fig. 2.3. Absorption is clearly low for photon energies below the band gap and increases at the exciton resonances. The laser machining described in the following section relies on the use of a laser with a wavelength of 1064 nm which corresponds to photon energies of 1.17 eV - far into the transparent regime for Cu_2O. Transmission spectra for the yellow exciton series are shown in Fig. 2.4 for both synthetic and natural samples. The intervals between the peaks show the characteristic energies of a Rydberg series as described by Eq. 2.2. States with principal quantum numbers up to $n = 14$ are observed in the natural sample compared to only $n = 10$ in the synthetic showing that the natural sample is of much higher quality in this case. The dominant peaks are those associated with p-excitons as transitions to these states are dipole-allowed, although both d- and f-states can also be observed, particularly the f-states which are also dipole allowed. An additional absorption peak occurs for transitions to the 1s orthoexciton state at 2.033 eV (at 4 K). As mentioned previously, transitions from the VB to the 1s exciton state are dipole forbidden, however this state is split into an orthoexciton and paraexciton (where the paraexciton is 12 meV lower in energy) and orthoexcitons are quadrupole active and are therefore weakly visible for sufficiently thick samples [52, 53].

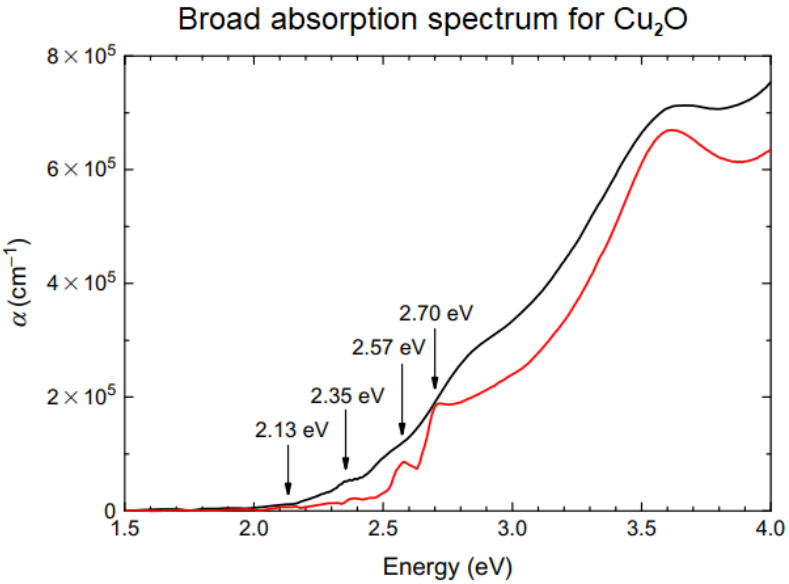

Figure 2.3: A typical absorption spectrum of Cu_2O at room temperature. The black line shows data from an as-grown film, and the red shows data from a film annealed at 930 °C [42].

The vibrational properties of Cu_2O are also relevant to this project due to the use of Raman spectroscopy. Phonon modes are vibrational resonances of atoms relative to the crystal lattice that they lie in. Different crystals have unique sets of resonances and thus investigating what these resonances are can reveal the type of material, or what impurities or defects it may contain. Raman spectroscopy is a method of measuring phonon modes (see Sec. 3.4 for details). A unit cell of Cu_2O contains 6 atoms which yield 18 phonon modes (3 degrees of freedom for each atom) three of which are acoustic modes, and the remaining fifteen are optical with symmetries given by the irreducible representations:

$$A_{2u} + E_u + T_{2u} + T_{2g} + 3T_{1u} \tag{2.6}$$

at the Brillouin zone centre (according to group theoretical analysis) where the E and T modes exhibit two- and three-fold degeneracy [42, 54, 55]. One of the T_{1u} modes represents acoustic phonons and is therefore optically inactive. The degeneracies of the two optical T_{1u} modes are partially lifted by LO/TO splitting (transverse-/longitudinal-optic) where the two-fold degenerate transverse-optical phonon modes are slightly lower in energy that the longitudinal optical one. These are infrared active, but not Raman active. The only Raman active mode is T_{2g} and the rest are silent (i.e. neither IR nor Raman active, see Table 2.1). The dispersions of the optical phonon modes of Cu_2O are shown in Fig. 2.5.

In a perfect crystal one would expect to see only a single peak during Raman spectroscopy since there is only one Raman-active mode, however, this is not the case. As can be seen in Fig. 2.6, the Raman spectrum of Cu_2O shows many peaks - more than can be explained with only the T_{2g} mode and its overtones (for the dispersion of this mode, see the lines at 515 cm^{-1} at the Γ-

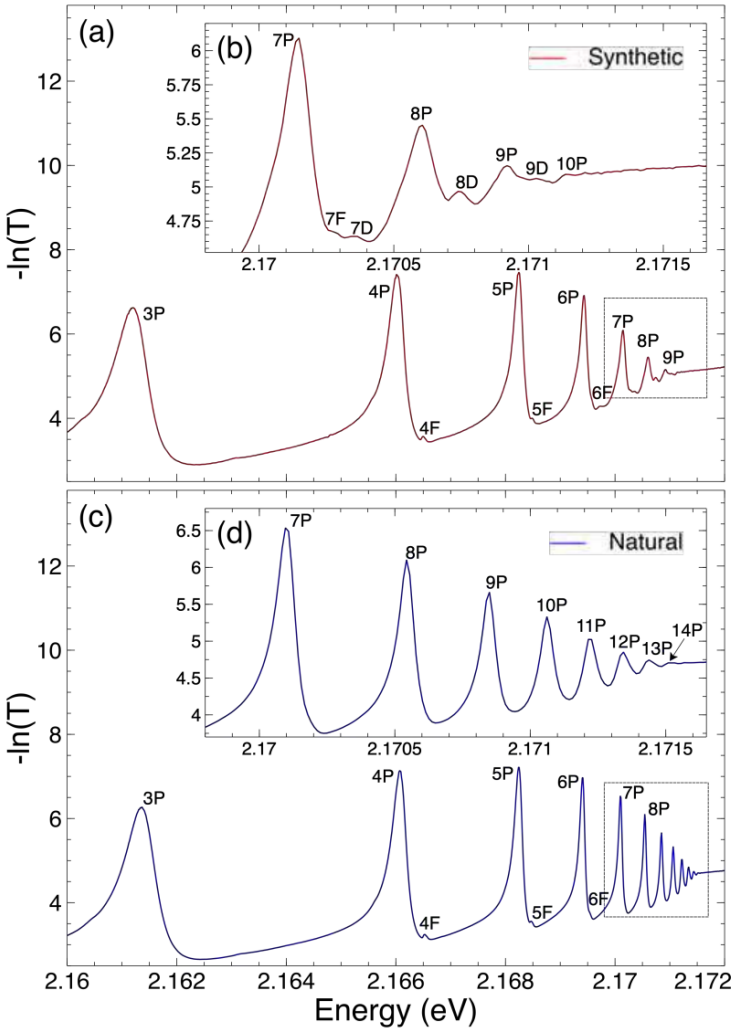

Figure 2.4: Transmission spectra over the yellow exciton series of Cu_2O for both synthetic - (a) and (b) - and natural - (c) and (d) - samples. Both samples were 80 µm thick and measured at a temperature of 5 K. High-n regions are shown in (b) and (d) [41].

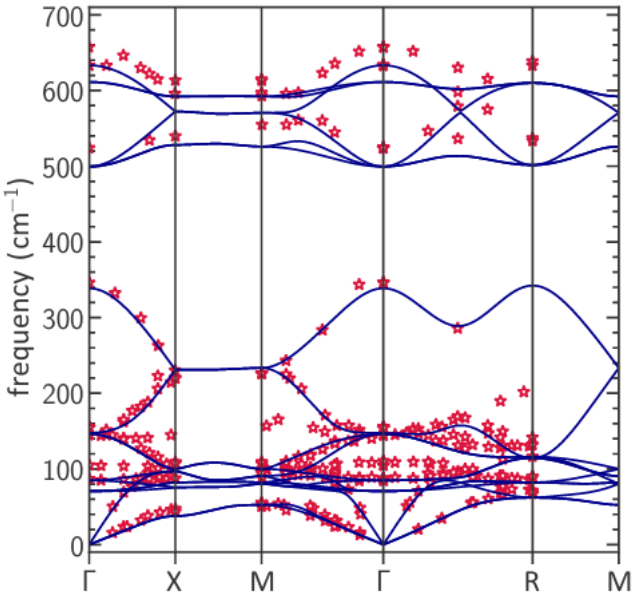

Figure 2.5: The phonon dispersion of Cu_2O [56]. The lines show the dispersion as predicted by calculations from first principles and the plotted points show measurements from neutron scattering experiments [57].

point in Fig. 2.5). This is due to non-stoichiometry in the crystal. Point defects in the lattice (e.g. vacancies) result in a local change in the symmetry of the crystal, usually a reduction. This can cause some Raman forbidden modes to become Raman allowed and thus Raman selection rules for a perfect crystal cease to hold strictly [54, 55]. Which modes become Raman allowed depend on the nature of these local symmetries which can be different depending on the point defect. This can therefore be used to determine which point defects are present in the crystal based on a Raman spectrum.

The most dominant feature of the Raman spectrum of Cu_2O is the large peak at 218 cm^{-1} which is attributed to the first harmonic of the E_u mode. Peaks at 143, 482, and ~ 630 cm^{-1} are attributed to the lower-energy T_{1u}, T_{2g}, and higher-energy T_{1u} modes respectively, though it should be noted that the Raman active T_{2g} peak does not quite match up to the expected values given in Table 2.1 as is the case in some sources [54, 55, 58] but not others [55, 59]. The peak at 408 cm^{-1} is not attributed to a single mode, but to multi-phonon scattering. Small Raman shifts can be difficult to detect since such strong filtering is required to remove wavelengths near that of the laser (see Sec. 3.4) which is why the first peak at around 108 cm^{-1} is a peculiar shape — it is likely the edge of a peak which cannot be seen due to filtering of these shorter wavelengths. Nevertheless, this could be the edge of a peak representing the T_{2u} or E_u modes. Finally, there is a small amount of activity at around 300 cm^{-1} which is often attributed to A_{2u} even though many sources put this much higher at 350 cm^{-1} [42, 55, 60]. It is possible that Raman activity at this shift is, in fact, indicative of the presence of CuO impurities. The Raman spectrum of CuO is also included in Fig. 2.6 which is dominated by a large peak at 298 cm^{-1}. This line of inquiry is not relevant to this project, but is elaborated

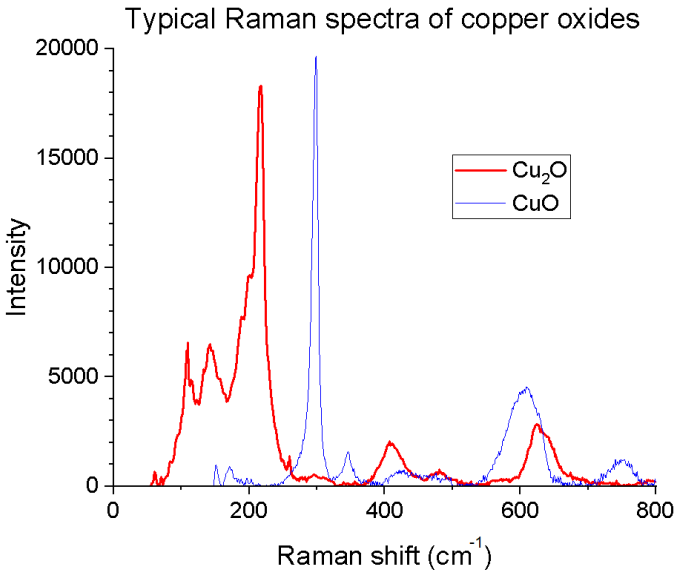

Figure 2.6: Typical Raman spectra for both cuprite (naturally occurring Cu_2O) and tenorite (naturally occurring CuO) [58].

on in Appendix C.

2.2 Laser machining

The purpose of laser machining in this project was to create microstructural defects within a crystal. For this, the laser used needed to have both ultrashort pulses, and be at a wavelength where the crystal is transparent such that a pulse of known energy can be delivered to a point inside the crystal (rather than just to its surface). This requires a multi-photon process using a laser at a transparent wavelength. Prior to this project, this type of laser machining had not yet been carried out on Cu_2O, but other semiconductors have undergone this type of laser machining. It should be stated, however, that much of the current focus in literature prefers the use of femtosecond laser pulses [33, 62, 63] whilst this project saw the use of picosecond pulses due to the availability of equipment. Corbari et al. [62] define three distinct regimes where the pulse duration, τ, is much greater than, much less than, or on the same time scale as the electron-phonon scattering time τ_{e-p}. For the first case, a thermodynamic equilibrium is reached between the electrons and the lattice. For the second, the pulse is delivered on a time scale where phonon scattering can be ignored such as with femtosecond laser machining. The third case is where picosecond machining falls and is more complicated since heating of the lattice and conduction band electrons occurs without reaching thermal equilibrium [64] which can result in melting and boiling of the sample [34, 37] and a greater amount of collateral damage compared to femtosecond machining which is therefore preferred for high-precision machining. It has also been shown that femtosecond laser pulses result in a much smaller statistical variation in the

Mulliken Symbol	Symmetry	Wavenumber (cm^{-1})	Nominal Activity
T_{2u}	Γ_{25}^{-}	85–100	silent
E_u	Γ_{12}^{-}	105–110	silent
T_{1u}(TO)	$\Gamma_{15}^{-(1)}$	140–152	IR
T_{1u}(LO)	$\Gamma_{15}^{-(1)}$	150–160	IR
A_{2u}	Γ_{2}^{-}	307–350	silent
T_{2g}	Γ_{25}^{+}	515	Raman
T_{1u}(TO)	$\Gamma_{15}^{-(2)}$	608–640	IR
T_{1u}(LO)	$\Gamma_{15}^{-(2)}$	640–662	IR

Table 2.1: Raman modes of Cu_2O. Ranges are given since reported values differ [42, 54, 55, 59, 60, 61]. Different sources may also use Mulliken symbols or the symmetry of the modes to differentiate between the phonon modes, both are given here. The acoustic modes, which are not seen in Raman spectra but in Brillouin scattering, are excluded.

threshold fluence for laser damage (defined as 'the fluence at which there is a 50% probability a laser pulse with this fluence will cause breakdown' [65] albeit compared to nanosecond pulses) which shows that, for shorter pulses, the statistical uncertainty with which damage is produced is reduced [37]. It would nevertheless be wrong to argue that femtosecond machining is necessarily preferred to picosecond machining for all purposes. For example, Zhang et al show that picosecond pulses are preferred over femtosecond pulses for creating ultrashort-laser written waveguides with the lowest loss in fused silica glasses [2] whilst Juodzakis and Misawa have shown the efficacy of picosecond pulses in crack-free, three-dimensional recording in borosilicate glass [66]. As for this project, it will be shown that picosecond machining was achieved, even though it wasn't the ideal pulse length, and was adequate for our purposes.

The absorption of the laser by the crystal can be understood using nonlinear optics. Classically, the polarization in a dielectric by an electromagnetic wave is related to the electric field by the equation:

$$\mathbf{P} = \epsilon_0 \chi \mathbf{E} \tag{2.7}$$

where $\mathbf{P}$ is the polarization, $\mathbf{E}$ is the electric field, ϵ_0 the permittivity of free space, and χ is the electric susceptibility. χ is a second-rank tensor, but in isotropic materials it is a scalar (neglecting spatial dispersion) having equal values for all three field directions. Theory based on this relation between $\mathbf{P}$ and $\mathbf{E}$ is called linear optics since the relationship between them is linear. However, this is only true for low optical intensity, as high powers, such as those of a laser, affect the optical properties of the dielectric. To account for this, Eq. 2.7 is altered to the form of a Taylor series:

$$\mathbf{P} = \epsilon_0(\chi^{(1)}\mathbf{E} + \chi^{(2)}\mathbf{E}^2 + \chi^{(3)}\mathbf{E}^3 + \ldots) \tag{2.8}$$

Here, the tensor rank of $\chi^{(n)}$ increases with each element of the series such that

its rank is $n + 1$. Eq. 2.7 represents the first element of this series. Further elements describe higher order and thus nonlinear optical phenomena.

One such higher order phenomenon is the absorption process undergone by the laser and the Cu_2O sample in this project. Since the sample is transparent at the laser wavelength, linear optics dictates that it would not be absorbed due to the incident photons having insufficient energy to bridge the band gap. Instead, two-photon absorption must occur where the laser power (i.e. photon density) is great enough that the probability of two photons being absorbed simultaneously by an electron becomes significant. When combined, the photons have sufficient energy to bridge the band gap. Given that Cu_2O has a band gap $E_g = 2.17\,\text{eV}$, we can deduce that a laser of sufficient power requires a wavelength between 571 and 1143 nm (wavelengths corresponding to photon energies of E_g and $E_g/2$ respectively) to achieve this type of absorption.

For picosecond machining, most of the energy transferred to the crystal by the pulse is nevertheless done by a first order (linear) mechanism. This is because linear absorption can occur involving the electrons liberated in the nonlinear mechanism which can, in turn, transfer energy to other electrons which themselves may be ionised and undergo linear absorption and so on. This is aptly known as avalanche ionisation [33, 67, 68] which becomes the dominant absorption mechanism once the two-photon absorption has occurred. However, avalanche ionisation cannot occur without some electrons having already been ionised, thus the onset of the nonlinear absorption is the threshold at which laser machining will occur.

An additional nonlinear effect that comes into play for this kind of machining is the optical Kerr effect which causes beam self-focusing resulting in filamentation of the laser beam [36]. At high laser powers, the refractive index of an optical medium is altered according to the equation:

$$n = n_0 + n_2 I \tag{2.9}$$

where n is the refractive index, n_0 is the linear refractive index, n_2 is the nonlinear Kerr index, and I is the intensity of the light. This is actually a third-order optical effect and is related to the third-order susceptibility in Eq. 2.8 by $\chi^{(3)} = 4\epsilon_0 c n_2 n_0^2/3$ [67]. Note that this is the same order phenomenon as the two-photon absorption which is described by the imaginary part of $\chi^{(3)}$, and $\chi^{(2)}$ need not be considered as it is zero in centrosymmetric crystals like Cu_2O. Assuming a Gaussian spatial intensity profile, and since n_2 is usually positive, this results in an increase in the intensity-dependent refractive index at the centre of the beam compared to the outside causing the beam to focus by refraction thereby increasing the beams intensity and decreasing its radius. Multi-photon absorption, such as the two-photon absorption described above, eventually occurs at a high enough intensity and the subsequent electron plasma generated in this ionisation results in a decrease in the effective refractive index to counteract the increase brought about by the optical Kerr effect [67]. This can result in localised refocusing cycles, although it should be noted that these cycles are temporal and not spatial (i.e. at a given point in the sample the beam width may change cyclically with time) and so every

point in the sample along the axis of a laser would still experience a filamented laser in this scenario.

Self-focusing is expected to occur when the intensity of light becomes high enough that the change in refractive index counteracts the diffraction of light which is independent of intensity. By relating the Rayleigh length to the self-focusing length, it can be shown that it is a beam's power that determines whether diffraction effects can be overcome according to the equation [67]:

$$P_{cr} = \frac{3.77\lambda^2}{8\pi n_0 n_2} \tag{2.10}$$

where P_{cr} is the critical power above which self-focusing dominates over diffraction (this is assuming a Gaussian beam). As will be expanded upon in Ch. 3, the machining laser in this project had a wavelength of 1064 nm. Given that $n_0 = 2.7$ for a laser wavelength of $\lambda = 1064\,\text{nm}$ [69], and assuming a value of $n_2 = 0.917 \times 10^{-17}\,\text{m}^2/\text{W}$ [70], this suggests a value of $P_{cr} = 6.86\,\text{kW}$. For a 30 ps laser pulse, this is equivalent to a pulse energy of 20.6 nJ.

Chapter 3

Materials and methods

3.1 Samples

Samples of Cu_2O of both natural and synthetic origin were investigated during the course of this project. Due to how the samples needed to be mounted for laser machining, and the thicknesses required for sufficient light transmission, they were prepared such that they consisted of thin slices (less than 0.5 mm thick). These were cut from rods or gemstones (for synthetic and natural samples respectively) and polished to create multiple samples. To achieve this, the rod was first encased in ViaFix^{TM} cold setting resin, then relatively thick slices (around 5 mm) were cut using a Struers Secotom-50 saw fitted with an M1D20 diamond cut-off wheel. This slice was then roughly ground using an MD-Piano 50 disk, then finely ground on a Struers MD-Largo disk with a 9 µm diamond suspension, and finally polished using a DP-DAC satin woven acetate cloth disk with a 3 µm diamond suspension. Sample thicknesses were measured using an Olympus BX-50 transmission microscope by adjusting the stage to where each surface was in focus, taking a reading for these depths and finding the difference between them; this value was then multiplied by the refractive index of Cu_2O for red light, $n = 2.9$ [69]. This could be done

Name	Thickness (µm)	Origin	Laser-machined
AF00	140	synthetic	✓
AF01	150	synthetic	
AF13	130	synthetic	✓
AF14	180	synthetic	
AG15	230	synthetic	✓
AL01	100	natural	✓
AM01	100	natural	✓
AH	n/a	natural	

Table 3.1: Showing all samples used in conjunction with this project.

Figure 3.1: Rods of Cu_2O grown using the optical floating-zone method. Thin discs were cut from the rods to prepare the samples that were used.

for samples whilst they were in the cryostat to be machined by moving the piezoelectric stage on which they were mounted (see Ch. 4.1) to bring each surface in focus; in this way, the thickness of the sample could be measured in more localised areas since this setup used a greater magnification than the Olympus microscope. In this case, the wavelength of the transmitted light was centred around either 571 or 609 nm depending on whether the HRSI (high-resolution spectral imaging) setup was set to scan the yellow Rydberg series or the 1s-orthoexciton. Refractive index values for these wavelengths were taken as 3.08 at 571 nm and 2.99 at 609 nm [69]. Thicknesses given in Table 3.1 were based on the readings taken at the corresponding machining sites.

3.1.1 Synthetic Samples

The synthetic samples detailed in this chapter were all fabricated by Dr Ravi Singh at the Indian Institute of Science Education and Research (IISER) in Bhopal, India. To achieve this, a 5 mm diameter copper rod of 99.999% purity was oxidised for roughly 40 hours in air at 1100°C and atmospheric pressure. This was then fused to a seed rod by melting and Cu_2O was subsequently grown using the optical floating-zone method [41]. The resulting rod is shown in Fig. 3.1.

The samples detailed in the next three subsections are addressed in the order in which they were laser machined. The final two samples, and the sample AH in the next section, were not laser machined but were used or examined in other ways as part of this research.

3.1.1.1 AF00 - Thin sample

The first sample to be machined, AF00 (see in Fig. 3.2), was a synthetic sample which was around 140 µm in thickness. Since it was used in the first attempt at machining, a lot of the work done on this sample was to confirm that machining was, in fact, possible, and to determine the settings necessary to achieve said machining. Once a working procedure was developed, machinings were done.

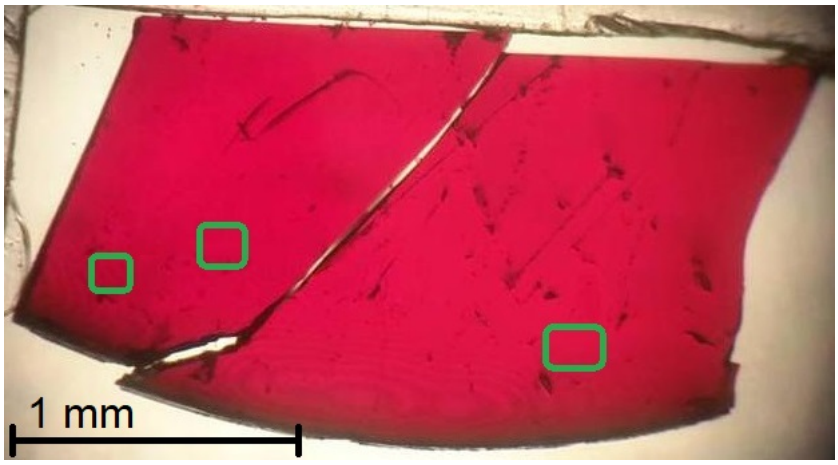

Figure 3.2: A photograph of the sample AF00 taken through a microscope. The sample is cracked into two pieces both of which were used in machining. Three of the machining locations are shown in green; these will be addressed further in Ch. 4.

This included machining the middle of the sample, although this was found to be difficult to do without affecting either surface of the sample. Further details of machining are given in Ch. 4.

3.1.1.2 AG15 - Thick sample

With the difficulties encountered in machining without affecting the surfaces in sample AF00, a thicker sample was chosen so that when focusing the beam in the middle of the sample for machining, the power density at the surfaces would be reduced. This was achieved with sample AG15 (see Fig. 3.3) which has a thickness of about 230 µm. However, the decrease in transmission close to the bandgap was such that there was not enough signal to perform the usual HRSI analysis on the exciton Rydberg series (more on this in Sec. 3.2). Therefore, the spectral range of this analysis was shifted to the 1s-orthoexciton wavelength - 608.5 nm where there is no background absorption (see Fig. 2.3).

3.1.1.3 AF13 - Medium sample

A sample with a thickness between that of the previous two was selected next to enable both mid-sample machining, and greater transmission. This was AF13 and had a thickness of 130 µm (shown in Fig. 3.3). As with AG15, transmission signal at the yellow Rydberg exciton frequency was too poor to carry out transmission microspectroscopy and only at the orthoexciton frequency was there enough transmission for further analysis. This is odd given that the sample thickness is comparable to AF00 so may suggest some alignment problem with the setup rather than low transmission through the sample. Machining within the sample without affecting the surfaces was feasible.

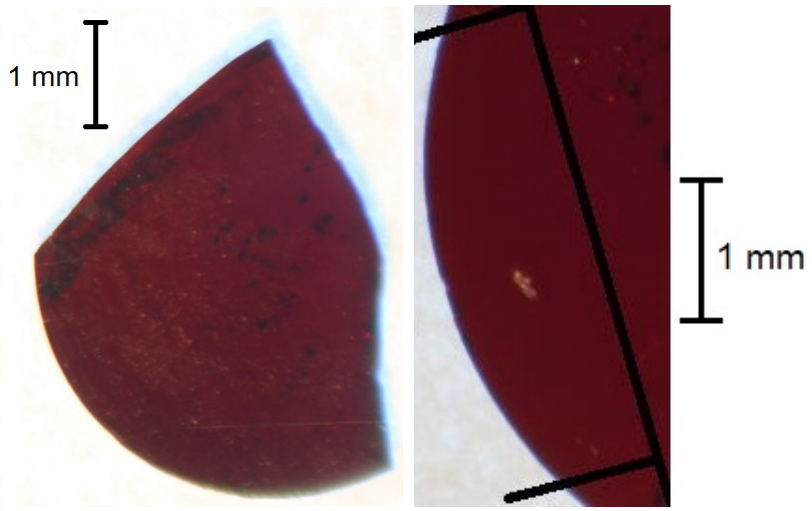

Figure 3.3: A photograph of the samples AG15 (left) ad AF13 (right) taken through a microscope. The clear curve in the bottom left of AG15 was once the edge of the rod described at the start of this chapter. The AF13 image comes from before it was cut from the disk, black lines are drawn to enclose the region that later became the individual sample.

3.1.1.4 AF01 - Etch test

This sample was not used in laser machining, but was used to test a chemical etching process that was as a possible way of removing impurities from the surfaces of samples (see Appendix A for further information on this). Ultimately, the goal was to etch the natural sample AL01 prior to laser machining, but tests were performed to ensure that this sample would not be destroyed by the process. The effect of the etching is shown in Fig. 3.4 where the surface of the sample has clearly become more rough and transmission has been reduced. This was in contrast to the effects seen for AL01 where the the surface was aligned to the (111) crystal plane which has been shown to reduce the effects of this type of etch [7].

3.1.1.5 AF14 - FIB-SEM test

AF14 is another synthetic sample of thickness roughly 170 µm. It was not laser machined, but was instead a test sample used in FIB-SEM (see Ch. 3.5) before looking at machined samples to avoid the risk of damaging any machinings unnecessarily with the FIB. An image of the sample is shown in Fig. 3.5 and an example of some of the FIB milling done on this sample is shown in Fig. 3.6.

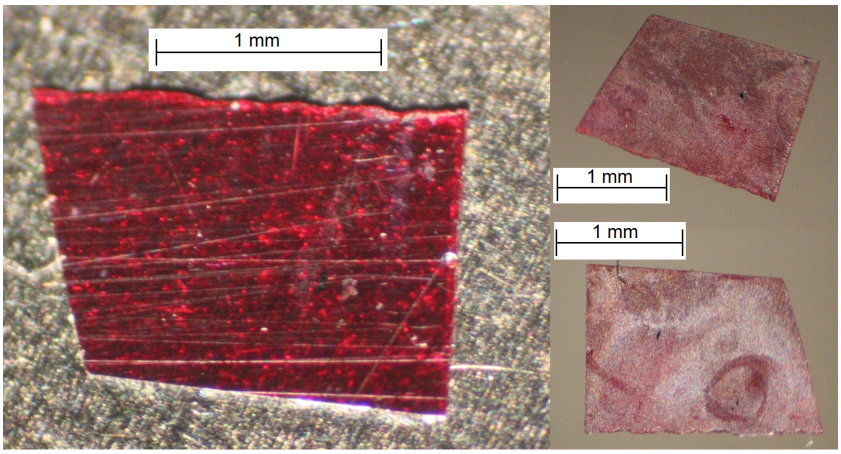

Figure 3.4: The image on the left shows the sample AF01 before etching. The two images on the right show each side of the sample after etching was carried out.

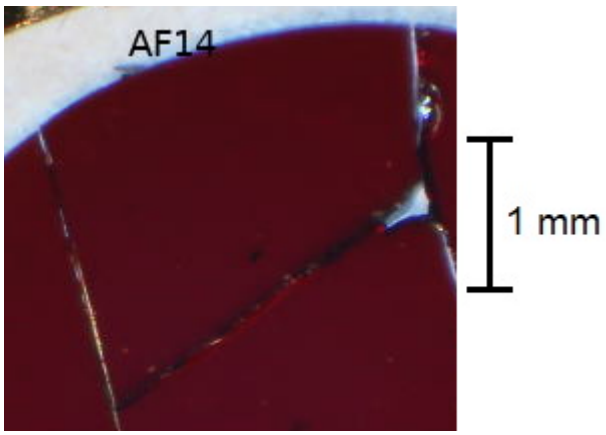

Figure 3.5: An image of the synthetic sample AF14 (other samples cut from the same disk of material can also be seen).

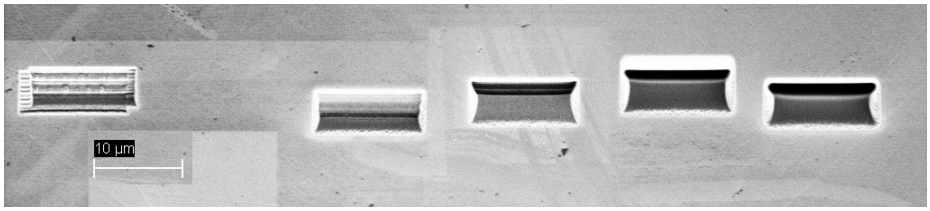

Figure 3.6: A FIB image of some of the FIB millings at various currents on sample AF14.

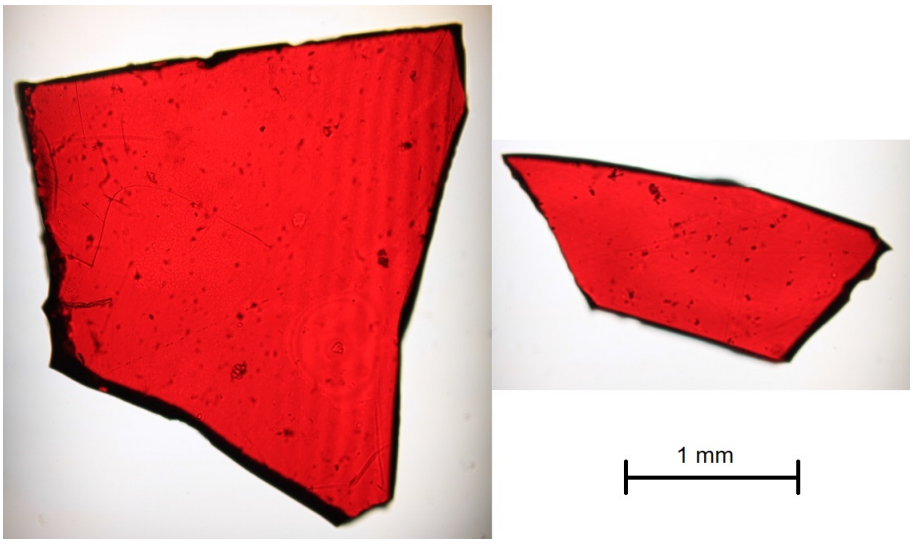

Figure 3.7: A photograph of the machined fragments of the sample AL01 taken through a microscope. The two fragments shown were broken apart after machining and both contain machinings.

3.1.2 Natural samples

3.1.2.1 AL01 - Thin sample

AL01 (Fig. 3.7) was the first natural sample to be machined. There were two main benefits to testing a natural sample; firstly, it could be compared to the synthetic samples to see if there are any differences in the machining process. It is documented that even the best synthetic crystals have a different concentration of defects than good-quality natural crystals, specifically a greater concentration of copper vacancies [40] (V_{Cu}) believed to result from a macroscopic crystal strain [41] which could have consequences in machining. Secondly, due to this lower defect concentration, and resulting lower absorption in the bandgap, natural samples can be used in second harmonic generation (SHG) provided they have 111 crystal orientation; with the surfaces of the crystal perpendicular to the [111] direction and therefore parallel to the (111) plane. Propagation of the excitation light in this direction allows transitions which would be dipole-forbidden [71]. Ultimately, the signal of the second harmonic was unexpectedly weak and thus no distinction could be made between normal and machined regions of the sample, but the machining was still carried out and the other analysis techniques employed. The sample thickness was 100 µm although readings of the sample thickness for the final two machinings sites were as low as 68 and 46 µm showing significant variation in the sample thickness. The machinings were done in sets where each set had a different purpose: investigating the effect of pulse energy, distance between pulses, creating structures of machinings around a single point, and a set that would be easy to look at using FIB-SEM.

After machining was carried out on the previous samples, the setup was altered to allow for the recording of the sample by a video camera during

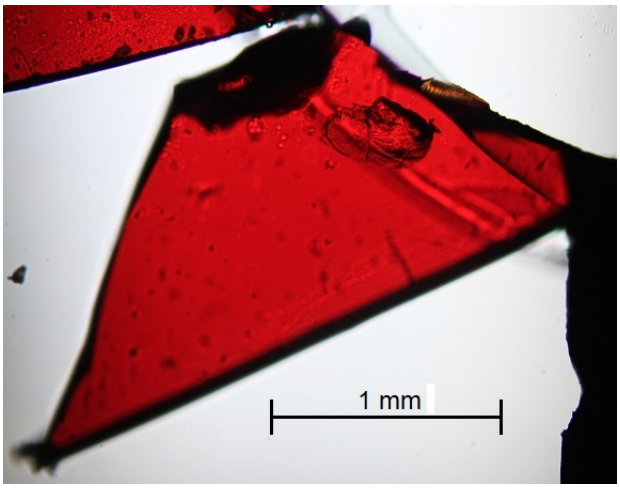

Figure 3.8: A photograph of the machined fragment of the sample AM01 taken through a microscope. This sample was split into 3 fragments during re-mounting, but only data from machinings in the fragment shown here are included in this thesis. Other fragments can be seen on the edges of this image.

machining (see Fig. 4.1). This is explained further in Ch. 3.2. In addition, this sample was chemically etched before any machining was carried out (see Appendix A). The etching procedure was tested beforehand on samples AH and AF01 (see Subsects. 3.1.2.3 and 3.1.1.4), but unlike those samples, there was no clear effect on AL01 due to its orientation.

3.1.2.2 AM01 - Thin sample

To help to achieve mid-sample machining, sample AM01 was prepared which is another natural sample (see Fig. 3.8). This was also oriented in the 111-direction but was slightly thicker (100 µm). Mid-sample laser machining was achieved in this sample, but only in 7 cases, all of which were preliminary test machinings (more detail in Ch. 4.4.5).

3.1.2.3 AH - Etch test

AH is a natural gemstone bought from Quebul Fine Minerals and originated from Poteryaevskoe Mine in western Siberia. It measures approximately $20 \times 20 \times 15$ mm and two other samples have been taken from it - AH01 and AH02 - which are unrelated to this project. The remaining stone was used in the preliminary test of the procedure for the wet etching technique mentioned in Sec. 3.1.2.1 before it was carried out on any of the thin, polished samples. The effect of the etching is shown alongside an image of the original sample in Fig. 3.9 where the surface of the sample seems to have become rougher and greyed compared to the original red sample.

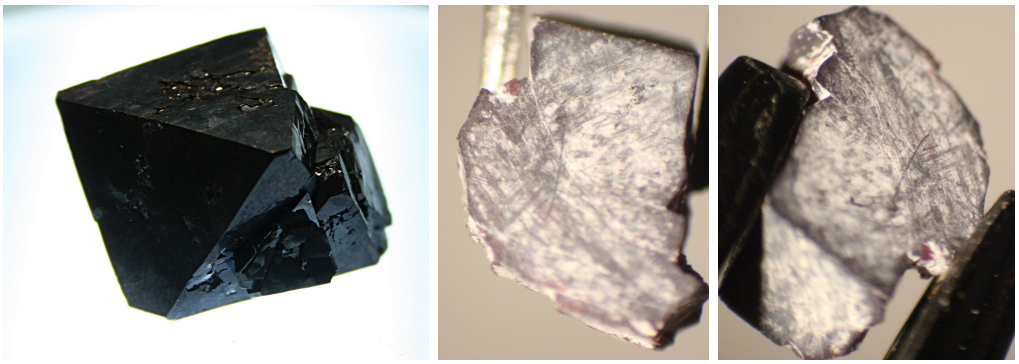

Figure 3.9: The image on the left shows the sample AH before etching. The two images on the right show the sample after etching (and after samples AH01 and AH02 were removed from it).

3.2 Absorption microspectroscopy

The setup for the high resolution spectral imaging (HRSI) is shown in Fig. 4.1 alongside the laser machining setup. The sample was Köhler illuminated using an LED light and adjustable apertures controlling the illumination size on the sample and in directional space. The light was filtered through a band-pass filter centred at 572 nm with a spectral width of 10 nm to remove light with wavelengths outside the range measured to reduce optical excitation and heating of the sample, then passed through the sample. The transmitted light was directed into the Iris 2000 Mark II spectrometer and Pixis:100BR CCD detector which had 100 pixels in the vertical direction along the spectrometer input slit at which a spectrum was taken over a wavelength range of roughly 10-12 nm over 1340 spectral pixels. The CCD camera was later replaced with the Pixis:400BR model with a 400 vertical pixels range prior to the machining of AL01 and AM01. In practice, the vertical range became limited instead by the height of the image formed but this still allowed for an increase in range in the y-direction of a factor of roughly 2 (to roughly 200 pixels). A vertical stack (of 100 or 400) of spectra constituted a single data acquisition at a given x-coordinate. In order to map the sample over a two-dimensional spatial region, the piezoelectric stage on which the sample was mounted was moved horizontally whilst the CCD performed a number data acquisitions (usually 100, but this depended on the width of the scanned region and the required spatial resolution). This resulted in a grid of 100×100 spectra having been acquired.

The spectrometer was set to the 2^{nd} order diffraction for all scans to increase the spectral resolution (at the expense of the signal strength due to greater dispersion at higher order of diffraction). For excitons at the yellow Rydberg series for which a nominal centre wavelength of 571 nm (2.171 eV) was used, the resulting spectral range was 4.2 nm, or 16 meV. To address the s-orthoexciton, the centre wavelength was 608.5 nm, or 2.0370 eV. Note the relation between

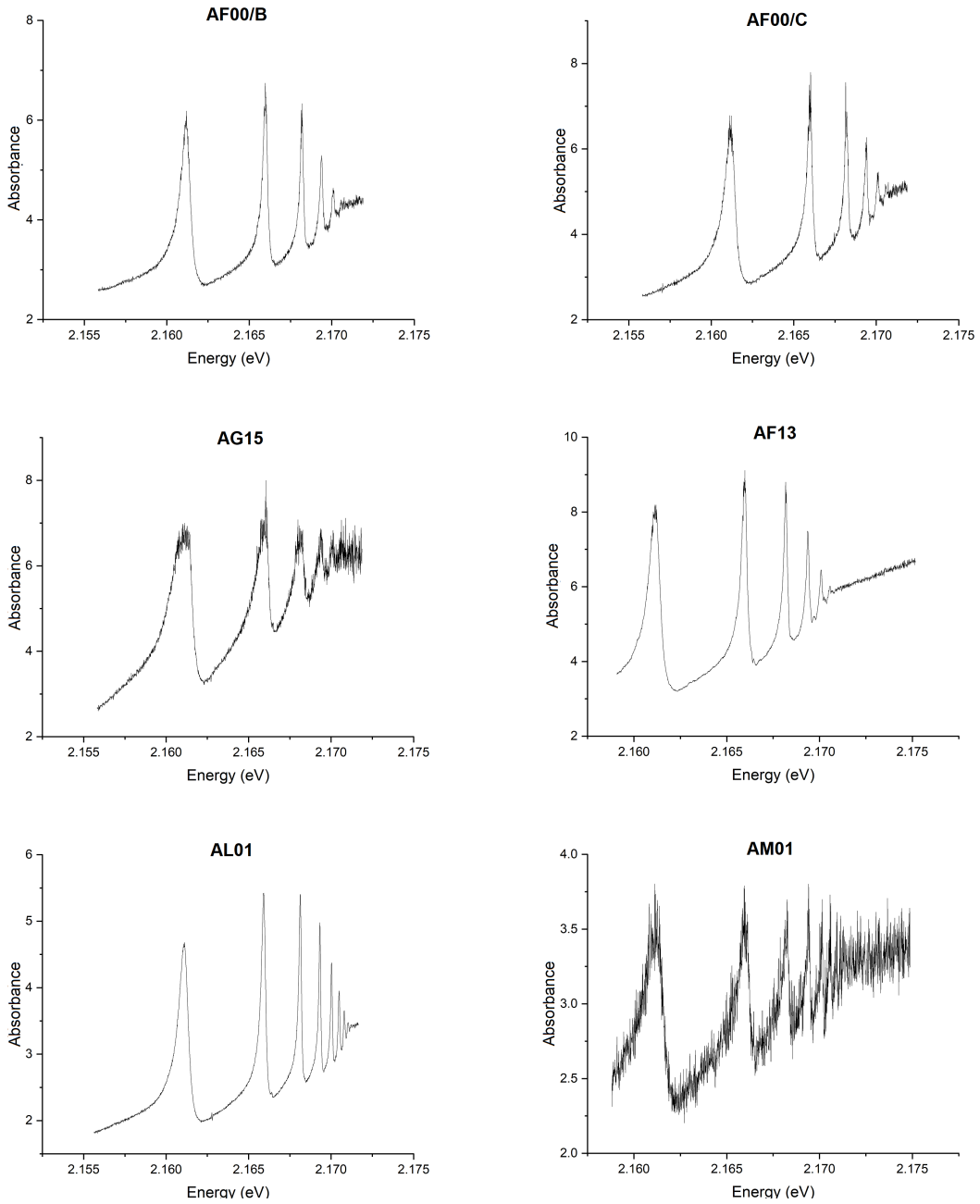

Figure 3.10: Examples of absorption spectra for the various samples used in this project from $n = 3$ upwards.

energy and wavelength according to the following equation:

$$E = \frac{hc}{\lambda} \tag{3.1}$$

where E is the photon energy, h is Planck's constant, c is the speed of light in a vacuum, and λ is the light wavelength.

To calibrate the resulting data, a helium neon discharge lamp was placed in the beam path after the hot mirror (see Fig. 4.1) directed towards the detector and a spectrum taken. The known emission peaks from neon were then used to calibrate the spectra accurately. For wavelength, the scaling was linear and a dispersion of -3.1725 pm per pixel was found for the second order diffraction. This was multiplied by the pixel number and added to a constant - the highest wavelength (λ_{M}) in the spectrum. For all subsequent scaling, the same dispersion was used, and the position of the emission lines of the helium neon lamp were used to determine λ_{M}.

In order to obtain an absorption spectrum two further sets of data were collected. One provided a background scan of 5 acquisitions with the LED light blocked. The acquisitions from this scan were averaged and then subtracted from the data taken with the LED unblocked in order to have data proportional to the detected intensity. Then, a reference scan of 20 acquisitions was taken in a region of the sample mount away from the sample itself to get a measurement of the source intensity without the sample. These were then averaged and an absorption spectrum, $A(\omega)$ obtained by combining this with the scan of the sample according to the equation:

$$A = \ln\left(\frac{I_0 - b}{I - b}\right) \tag{3.2}$$

where A is absorbance, I is the intensity, b is the background intensity, and I_0 is the intensity of the reference scan. Acquisition times varied depending on the sample but would typically be around 5-6 s. The resulting spectrum (examples shown in Fig. 3.10) contain absorption peaks according to the energies of the photons absorbed (hc/λ) by the excitons. Note that calibration was performed in air whereas this formula assumes vacuum wavelength so is only approximate. CCDPlot software was used to fit a differential Lorentzian curve to these peaks one at a time including a vertical offset, O, the equation for which is given by:

$$y = O + B\frac{1 + \delta_L(\nu - \nu_0)/\Gamma}{1 + ((2(\nu - \nu_0))/\Gamma)^2} \tag{3.3}$$

where ν_0 is the peak centre, Γ is the full width of half maximum (FWHM), B is the peak amplitude, and δ_L the differential amplitude - a measure of the peak asymmetry. Such an asymmetry is seen in Fig. 3.11 which shows an example of an absorption peak with its associated fitted peak. The asymmetry of the peaks is described as a Fano resonance which arises due to the interference of discrete spectrum of transitions with a continuous one; in the case of Cu_2O, this is occurs for direct exciton absorption transitions and indirect phonon-assisted transitions, respectively [72, 73, 74]. This fit was repeated for each

spatial point and the value of each of these five variables was then plotted in a 2D map. The results of this are shown in Ch. 4.

As mentioned previously, the use of thicker samples resulted in a decrease in transmission hindering the use of the above technique in the Rydberg series wavelength range. This change can be calculated using:

$$\frac{I}{I_0} = \exp(-\alpha(\lambda)L) \tag{3.4}$$

where I is the transmitted intensity, I_0 is the input intensity of the light, $\alpha(\lambda)$ is the wavelength-dependent absorption coefficient for Cu_2O, and L is the distance the light travels through the sample. α varies over the wavelength range scanned during HRSI acquisition (570-575 nm). Taking L to be the additional distance through the thicker sample rather than the thinner one that the light must travel ($\sim 100\,\mu m$) and $\alpha = 20\,mm^{-1}$ [69], then we should expect the transmitted intensity through the thicker sample, AG15, to be 13.5% of that through the thin sample, AF00, according to Eq. 3.4 (although errors in the values of α and L put this value in the range of 0.8-20%). In practice, the signal was found to decrease to 12% of the previous sample.

Although the light transmitted through AG15 was enough to show the absorption of the Rydberg series, the signal to noise ratio was low, in some cases the SNR was only 2 - this was due to the low transmission. When performing the analysis of these peaks, the resulting maps therefore lacked the fine structure of previous maps which is why the 1s-orthoexciton peak was looked at instead which lies in a much more transparent region of the spectrum (see Fig. 2.3). To fit this peak a normal, symmetric Lorentzian fit was used (i.e. without the differential amplitude parameter) since the peak was much more symmetrical. The fit was also made more difficult by the splitting of the 1s-orthoexciton states. Theoretically, orthoexcitons exhibit threefold degeneracy [44, 75], but in practice splitting was evident in the samples even without any laser machining present due to the linewidths of the absorption peak for the 1s-orthoexciton being narrower than the energy shift by internal strain. Two examples of this are shown in Fig. 3.12. The peaks would fluctuate between being combined and distinct and thus fitting them as either separate peaks or as a single degenerate peak often resulted in a poor quality of fit producing parameter maps with features that did not correspond to physical effects.

3.3 Absorption cross section

With the additional lens in place for laser machining of the final two samples, AL01 and AM01, videos could be recorded using the video camera in Fig. 4.1 whilst the laser pulse was delivered to the sample using the same illumination source of the absorption microspectroscopy. This reduced the depth offset required for laser machining from 115 µm to 17 µm. Although there would ideally have been no depth offset, by this point laser machining was understood to have an effect that went over a range of depths in excess of this value

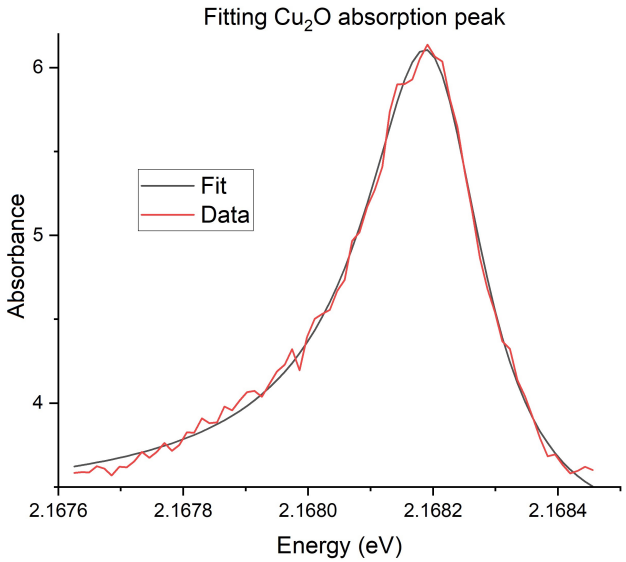

Figure 3.11: An $n = 5$ absorption peak from AF00 and the differential Lorentzian peak used to fit it.

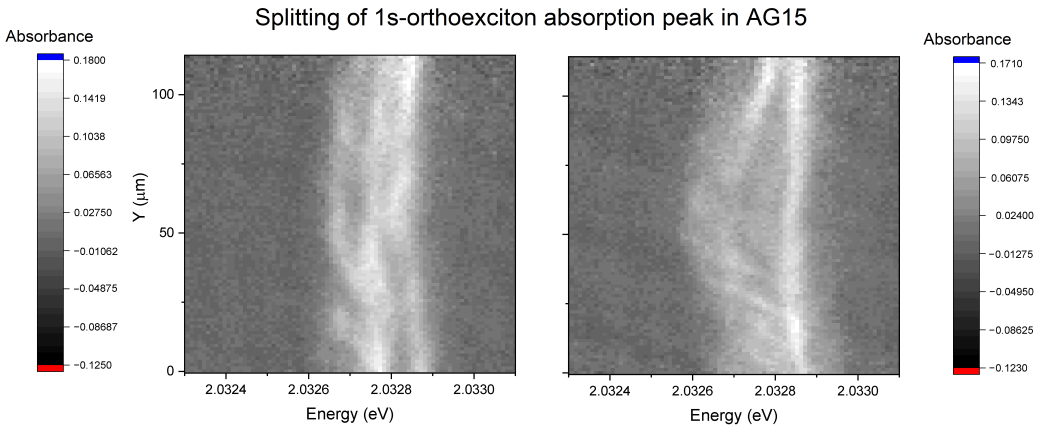

Figure 3.12: Two vertical stacks of absorption spectra at 6.5 K over the range of the 1s-orthoexciton absorption peak at different x-coordinates in the sample AG15 about 60 µm apart. The absorbance is represented by the brightness. The 1s-orthoexciton is a triply degenerate state, but splitting is evident throughout the sample.

and, furthermore, most of the effects seen in transmission photography were on the surfaces anyway. To increase the depth of field of this acquisition, the illumination NA was reduced to minimise the aperture without a sharp reduction in the transmission (compared to the that used for HRSI for which the NA was maximised) so that out-of-plane effects - such as machining on one of the surfaces - could be seen much more easily.

The resulting videos were converted to bitmap format and the frames before and after the pulse were averaged to create a before- and after-image of the machining. Then, by dividing the after-image by the before-image and integrating over the area affected by laser machining, the absorption cross section (σ_{A}) could be calculated for each machining according to:

$$\sigma_A = B\left(b - \frac{I}{I_0}\right), \tag{3.5}$$

where σ_A is the absorption cross section, B is the area over which I/I_0 is averaged in $(\mu\mathrm{m})^2$, I and I_0 are the transmitted intensities after and before machining respectively, and b is the value of the non-machined background of the I/I_0 image. B was chosen to be the smallest area enclosing the laser-affected region, and b was calculated by averaging I/I_0 in the area surrounding this region.

A similar procedure was used to calculate a value for the transmission change cross section (σ_{TC}) to account also for increases in transmission for certain pixels. Using the above method, the overall change was a decrease in transmission due to laser machining, but the method used assumed that a decrease was the dominant effect. To confirm this, Equation 3.5 was altered to:

$$\sigma_{TC} = \sum_{x,y} |b - \frac{I}{I_0}| \tag{3.6}$$

where x, y denotes the x and y values of the pixels in the region affected by the laser machining. The two important changes here are finding $b - I/I_0$ for each pixel, and finding the magnitude so that increases in transmission for individual pixels could be found. The result was compared to values of σ_A for each machining.

3.4 Raman spectroscopy

Raman spectroscopy is an analysis technique that allows us to measure vibrational modes within a sample. A monochromatic light source is used to illuminate a sample with narrow-band light, typically a laser. Generally speaking, light incident on matter will be absorbed, transmitted, or experience Rayleigh or Raman scattering. In Raman scattering, some internal excitation is involved in the scattering which causes the scattered photon to experience a frequency shift equal to the energy of the internal excitation according to $E = hf$. Typically, these excitations are vibrational and are represented by phonons which can be absorbed (Anti-Stokes scattering given by Eq. 3.7) or emitted (Stokes

scattering given by Eq. 3.8). The relations between incident photons, scattered photons, and phonons are given by:

$$\begin{aligned} E_{\text{in}} + E_{\text{ph}} &= E_{\text{sc}} \\ \frac{1}{\lambda_{\text{in}}} + \frac{1}{\lambda_{\text{ph}}} &= \frac{1}{\lambda_{\text{sc}}} \end{aligned} \tag{3.7}$$

$$\begin{aligned} E_{\text{in}} &= E_{\text{sc}} + E_{\text{ph}} \\ \frac{1}{\lambda_{\text{in}}} &= \frac{1}{\lambda_{\text{sc}}} + \frac{1}{\lambda_{\text{ph}}} \end{aligned} \tag{3.8}$$

where the subscripts in, sc, and ph refer to the incident photon, the scattered photon, and the phonon respectively. The scattered light is picked up by a microscope which is coupled to the spectrometer consisting of a grating and CCD detector which provides a spectrum in which the peaks appear that are shifted from the wavelength of the incident laser. The energies of the phonon modes can be calculated from this using Eq. 3.8. Though, the convention is rather to show Raman shift in cm^{-1} instead of wavelength where Raman shift is the shift in wavenumber of the scattered photon. This value is constant no matter what the wavelength of the excitation laser is whereas the the wavelength shift is not.

This setup was also used to measure the photoluminescence (PL) in the sample. Here, the laser which is intended to provide a monochromatic light source for Raman scattering also acts as a source of electronic excitation. Electrons in the sample may be excited if the incident photons have enough energy to achieve this. The amount of energy that the excited electrons have is much greater than phonon energies and so, as these electrons relax, they emit light with photon energy equal to the energy lost during relaxation - photoluminscence - which is picked up by the microscope and spectrometer in exactly the same way as the Raman scattered light is. Resulting spectra may therefore involve both of these features.

The equipment used was a Horiba Scientific LabRAM HR Evolution Raman Spectrometer [76] with 3 excitation lasers of wavelength 473, 532, and 660 nm and operated through LabSpec 6 Software [77]. An integrated BX41 microscope was used to collect the light from the sample. This was also used to position the sample correctly and provided images of the sample's surface by reflection contrast. The microscope was coupled to a spectrometer which consisted of a diffraction grating which acts as the monochromator and a multichannel, air-cooled CCD Detector (at -60 °C). Diffraction gratings of 1800, 600, and 300 l/mm were available, with the spectral range scaling approximately inverse to the groove density. It was found that the 300 l/mm grating had sufficient resolution to show any relevant peaks and provided such a spectral range (660-765 nm using the 660 nm laser) that a PL peak was also covered by the CCD at a single spectrometer position; this was therefore used in the majority of this analysis. During scans the sample was mounted on a motorised XYZ stage driven by the LabSpec6 software.

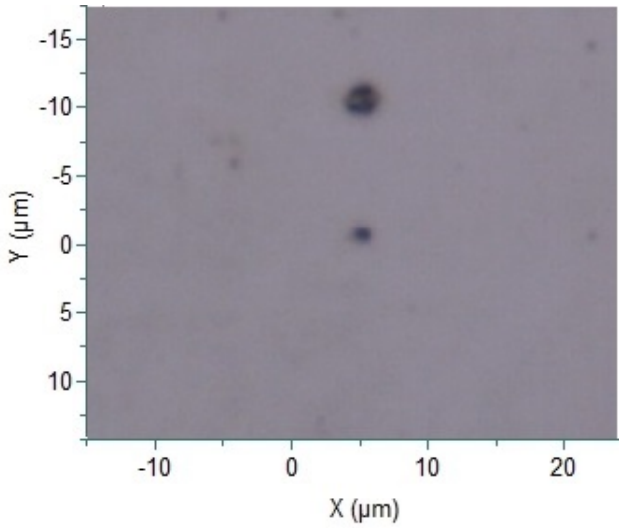

Figure 3.13: A reflection image using white light showing the effect of using a 473 nm laser to perform Raman analysis on Cu_2O. The large spot at the top was the result of 6 s of laser exposure. The spot below was created with a 3 s exposure with the laser attenuated to 50% of its full power. Laser exposure at 25% power and lower were performed below this with no visible effect.

The 660 nm laser was predominantly used since it was the only laser with photon energy lower than the band gap energy of Cu_2O; $E_g = 2.0\,\text{eV}$ at room temperature [78]. This is equivalent to light of wavelength $\sim 620\,\text{nm}$ which is consistent with the energy of the first PL peak measured when using the 473 nm laser in initial scans. The higher photon energy lasers still yield Raman spectra, but the high absorption of the sample at that wavelength prevents penetration into the sample so only the surfaces could be analysed. Higher energy excitation lasers were also found to damage the sample even when attenuated, whilst the 660 nm laser did not. Fig. 3.13 shows the effect that the 473 nm laser had on the surface of a sample. Extinction coefficients (κ) for Cu_2O at the three given laser wavelengths are 0.67, 0.03, and 0 for 473, 532, and 660 nm respectively [69] (the value of zero here means that the value is $< 10^{-5}$, the values provided here are also for thin films so may differ slightly for bulk Cu_2O). Given that the penetration depth, δ_p (the depth into a material after which the intensity of light falls to $1/e$ of its original value), is given by the expression $\delta_p = \lambda/4\pi\kappa = 1/\alpha$, and assuming the maximum extinction coefficient at 660 nm given the above value ($\kappa = 10^{-5}$), this is equivalent to a penetration depth of at least 1 mm - far more than the thickness of any of the samples. The use of the 660 nm laser therefore meant that 2D x-y scans could be taken at multiple z-depths to create a 3D array of data points (see Fig. 3.14). Further parameters for Raman acquisition can be found in Appendix C.

The resulting data were then analysed with the hyperspectral analysis software HIA (hyperspectral image analysis), 'a method to factorize the hyperspectral data into the product of component concentrations and spectra' [79]. This involved first the denoising of a hyperspectral data set using singular value de-

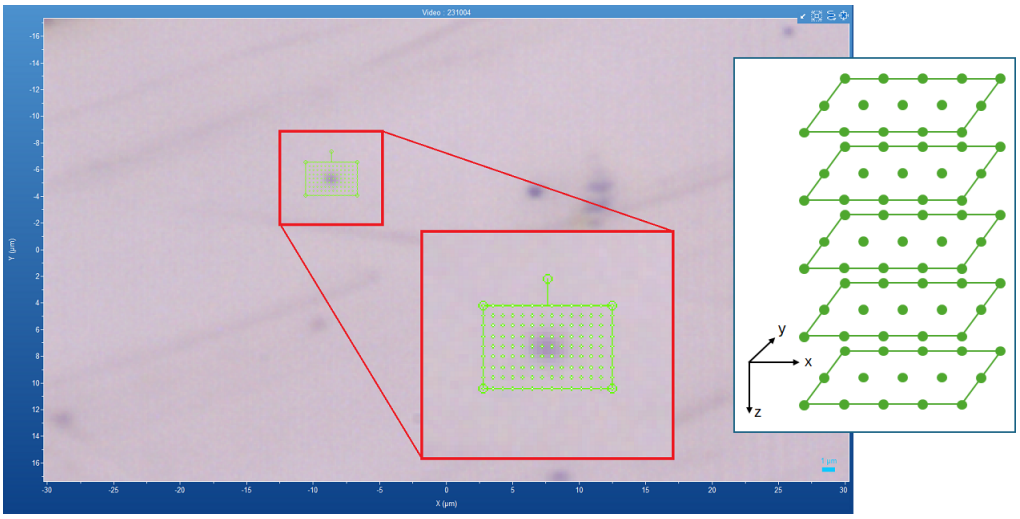

Figure 3.14: A screenshot taken during a Raman spectroscopy session using the 20× microscope objective. It shows a white light reflection image acquired by the colour camera within the LabRAM system of the front surface of a machined sample, the machinings themselves can be seen. In green is the grid of points at which a Raman spectrum was acquired. This was repeated at multiple depths to achieve a 3D array of points (shown on the right).

composition (SVD) followed by a factorisation into spectra and concentrations of chemical components (FSC^3). To achieve SVD, the data, represented by a matrix $\mathbf{A}$ of size $m \times n$ was decomposed into 3 separate matrices given by:

$$\mathbf{A} = \mathbf{U}\mathbf{\Sigma}\mathbf{V}^{\mathbf{T}} \tag{3.9}$$

where $\mathbf{U}$ is an $m \times m$ orthonormal matrix, $\mathbf{V}^{\mathbf{T}}$ is an $n \times n$ orthonormal matrix, and $\mathbf{\Sigma}$ is an $m \times n$ diagonal matrix where the terms A_{ii} are called the singular values which are positive and sorted in descending order. The smallest singular values, which represent noise-like spatial and spectral distributions in $\mathbf{U}$ and $\mathbf{V}$, are set to zero thereby removing them from the reconstruction of $\mathbf{A}$. Therefore, noise can be removed from the data whilst preserving the signal by considering only the first singular values up to a certain threshold. This threshold was determined separately for each set of data to ensure that the removed singular values did not contain any discernible signal. Typically, this would be in the range of 6-14 (i.e. the first 6 singular values would be used to reconstruct $\mathbf{A}$ for a threshold of 6).

The resulting data, represented by a matrix $\mathbf{D}$ then underwent further factorisation into matrices $\mathbf{C}$, $\mathbf{S}^{\mathbf{T}}$, and $\mathbf{E}$ where $\mathbf{C}$ represented a (spatial) concentration of a number of chemical components, $\mathbf{S}^{\mathbf{T}}$ represented the spectra associated with these components, and $\mathbf{E}$ was an error matrix to be minimised. The relationship between these matrices is given by $\mathbf{D} = \mathbf{C} \otimes \mathbf{S}^{\mathbf{T}} + \mathbf{E}$. The additional physical constraint that $\mathbf{C}$ and $\mathbf{S}^{\mathbf{T}}$ must be non-negative was also introduced, this factorisation is called non-negative matrix factorisation. This provided Raman spectra of each chemical component with an associated spatial distribution of the concentration of that component. This technique is

called factorisation into spectra and concentrations of chemical components (FSC^3) [79, 80]. The number of components was chosen in advance of the FSC^3 analysis and was varied to ensure that this number was equal to the number of materials with different Raman spectra in **D**. Without laser machining, only one component should theoretically be sufficient to describe the single crystal, but a change in chemical composition due to laser machining could be detected by increasing the number of components.

3.5 FIB-SEM

Focused ion beam (FIB) - scanning electron microscopy (SEM) was used to reveal the profile of the machinings both on and beneath the surface using a Carl Zeiss 1540XB CrossBeam workstation operated using SmartSEM V5.06 software. SEM is an imaging technique capable of generating extremely high-resolution images. This is achieved by scanning the surface of a sample with a electromagnetically focused electron beam causing secondary electrons to be emitted from the sample's surface due to inelastic collisions with the electrons from the beam up to a depth of only a few nm [81] [82]. The value of each pixel in the image is the sum of an offset (the brightness) and contrast where the latter is linearly scaled with the current of the detected electrons. Both brightness and contrast were controlled by knobs on a control board and were adjusted to achieve a useful imaging of the regions of interest, but the control of these values was not recorded.

The ions used in the FIB are gallium and, just as with the SEM, these can generate secondary electrons upon collision with the sample which can be detected in the same manner. The beam itself is formed from a liquid metal ion source (LMIS) in which melted gallium is deposited onto a tungsten needle with a large voltage applied which causes the gallium atoms to ionize and be emitted from the needle and directed towards the sample by electrostatic lenses. Unlike SEM, this can be quite destructive to the sample due to the high mass of the ions and therefore can be used not only to image, but also to mill away parts of a sample with high precision. The FIB's axis was chosen to be perpendicular to the surface of the sample while the beam used in SEM was at a 54° angle to the FIB (see Fig. 3.15).

To uncover any features beneath the surface, the FIB was used to mill a trench in front of it with a high current (2 nA for around 30 minutes), and then the end of the trench closest to the machining was gradually polished away with a much lower current (20-50 pA for 1-2 minutes) to result in a finer polish. Fig. 3.16 shows the milled trench in front of a machining (from the perspective of the SEM) before polishing. Since the SEM gun was at an angle to the polished wall, it could image the wall between each polish to reveal any inhomogeneities due to laser machining. When such effects were found, higher quality SEM images were acquired by changing the SEM acquisition method, scan speed, and/or resolution. The standard acquisition method was to perform a pixel average in which a single frame was scanned at a rate of $100 \times 2^{S-1}$ ns per pixel where S is the scan speed setting - an integer from

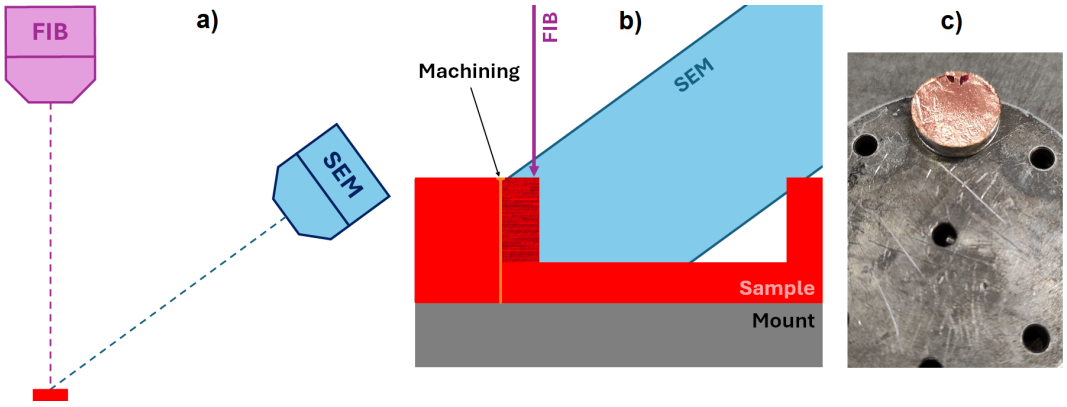

Figure 3.15: a) The sample sits at the coincidence region of the ion and electron beams. The FIB is perpendicular to the sample surface and the SEM is 54° from it. b) A representation of FIB-milling and SEM-imaging (these do not occur at the same time). The FIB removes layers from the back wall of a trench until the laser machining is reached which can be imaged by the SEM. c) The sample itself is attached to an adhesive copper pin which is then mounted.

1 to 15, resulting in pixel dwell times of 100 ns to 1.6 ms. Pixel average was faster than other methods so was useful in providing a real-time display of the sample. For higher quality images, the line integration method was used. Here, each line (horizontal row of pixels) was scanned multiple times and the average was stored and displayed. For scans over a large area, the slowest scan speeds could take hours to complete. In later sessions as the procedure was improved to reduce the time taken for scans the area scanned was reduced to include only the region of interest allowing for the use of very slow scan speeds without having to wait more than 10-20 minutes. Finally, the resolution of the images was also increased when looking at very small effects from 1024×768 pixels to 2048×1536. This had the effect of increasing the total acquisition time of the image so was mostly useful when even the slowest scan speed using the lower resolution didn't produce an image of good enough quality.

In many cases, especially early in the development of the above procedure, no inhomogeneities were seen beneath the machinings which were visible as small craters on the surface. Now it may well be possible that there simply was not any discernible effect below the surface, but it is also possible that the machinings may have been completely destroyed in the polishing step or lay deeper in the sample was seen. The smallest polishing thickness was about 200 nm due to limitations in the magnification of the system used, whilst some of the subsurface effects were $<$100 nm across in the direction of polishing (as will be shown later). It would therefore not only be possible, but likely for the back wall of the FIB-milled trench to be so close to the machining that even the smallest polish would destroy it in one go. This may beg the question as to why so many effects *were* then seen using this technique for which there are three answers. Firstly, not all of the sub-surface effects were so small - larger ones were easier to find. Secondly, a very small tilt in the sample would have been

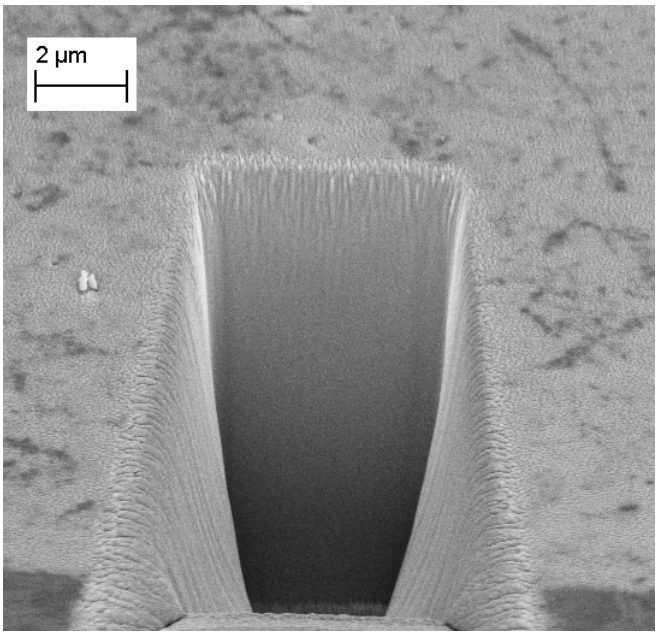

Figure 3.16: An SEM image at 8,000× magnification at scan speed $S = 7$ showing a trench milled using FIB in front of a machining which has affected the surface of the sample. The trench is 17 µm long and we see to a depth of 12.4 µm (since there is a 54° angle between the FIB and SEM).

enough to allow a polish to reveal part of the machining without destroying it as long as the FIB-milled trench was deep enough. For example, over the height of a 30 µm deep trench, a 100 nm diameter machining would double its range in the polishing direction with a tilt in that direction of only 0.2°. Given the numerous demounting and remounting, and even sample cracking, between when the laser machining was carried out on sample an when FIB-SEM was performed, it could reasonably be expected for the sample to have become tilted by around 1°. This is seen in some of the results in Ch. 5. Finally, in later sessions the procedure was optimised to allow for a finer polish (as little as 60 nm) by intentionally creating a spatial offset between both FIB and SEM so that a greater magnification and therefore precision could be used on the FIB whilst also being able to image deeper in the sample with the SEM.

3.6 qDIC

Differential interference contrast (DIC) is an imaging technique performed using a microscope setup capable of producing high contrast images of structures that exhibit phase contrast created, for example, by birefringence. Cu_2O is not a birefringent material, birefringence can be introduced in a sample due to, for example, strain induced from a local defect. In our case this defect is, of course, due to laser machining.

DIC microscopy was carried out by passing polarized light from a Köhler illumination source through a Wollaston prism which separated the light into

two orthogonally polarized beams which were directionally separated from each other by a small amount. These two beams were then focused onto a sample by the condenser lens, converting the directional split into a spatial split called the shear distance. As these beams passed through the sample, they acquired a phase difference, δ_ϕ due to a spatial- and polarization-dependent refractive index. Then, an objective lens collimated the transmitted light into a Nomarski prism which recombined the beams at the far-field of the objective lens. This prism was also translated perpendicularly to the beam path to create a phase offset, ψ, between the two beams by changing the relative thicknesses experienced by the beams of the birefringent wedges that formed the prism. The light was then passed through a polarizer oriented orthogonally to the original polarization so that the resulting intensity upon reaching the camera could be given by:

$$I_{out} = \frac{I_{in}}{2}(1 - cos(\psi - \delta_\phi)) \tag{3.10}$$

This was repeated for a phase offset of $-\psi$ and the images were combined to create the contrast image with pixel values I_C according to:

$$I_C = \frac{I_{out}(+\psi) - I_{out}(-\psi)}{I_{out}(+\psi) + I_{out}(-\psi)} \tag{3.11}$$

Values of ψ were used such that the criterion $\delta_\phi << \psi < \pi$ was met which allows Eq. 3.10 to be linearized to the approximation:

$$I_C = \frac{\delta_\phi sin(\psi)}{1 - cos(\psi)} \tag{3.12}$$

This means that the resulting pixel values are directly proportional to the phase difference of the two beams [83] [84] and converting the pixel values to represent δ_ϕ for a known ψ is trivial. This setup is shown in Fig. 3.17 [85].

The equipment used were an Olympus BX-50 microscope with a 20× objective and Canon EOS500D Camera. This analysis was performed at multiple depths throughout a laser-machined sample and also at multiple sample orientations as it was found that this had an effect on the result. Rotating the sample by 180° around the optical axis has no effect on the birefringence but does alter the phase gradient. Images were then paired with their 180° rotated counterpart to separate the phase gradient effects from the birefringent effects by aligning the images with each other, then either subtracting them or averaging them respectively using the software ImageJ. An example of how these images are created is shown in Fig. 3.18. The two left images are phase difference images which are added to or subtracted from one another to create the images shown on the right representing birefringence and phase gradient respectively.

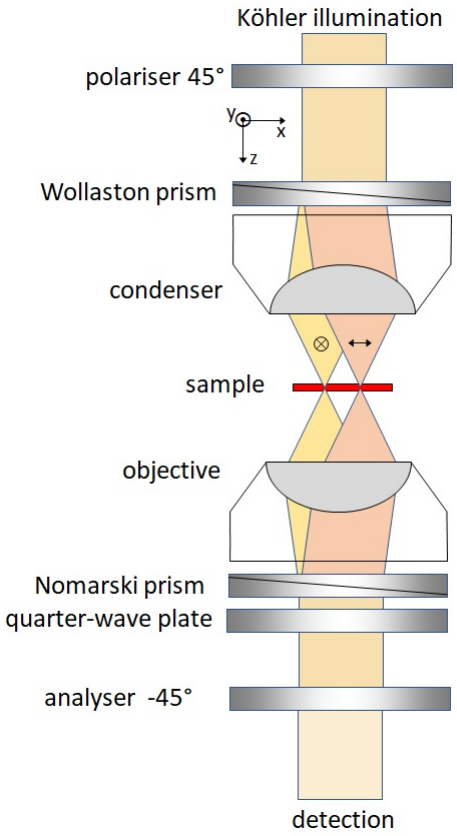

Figure 3.17: A diagram showing the differential interference contrast microscopy setup. [86]

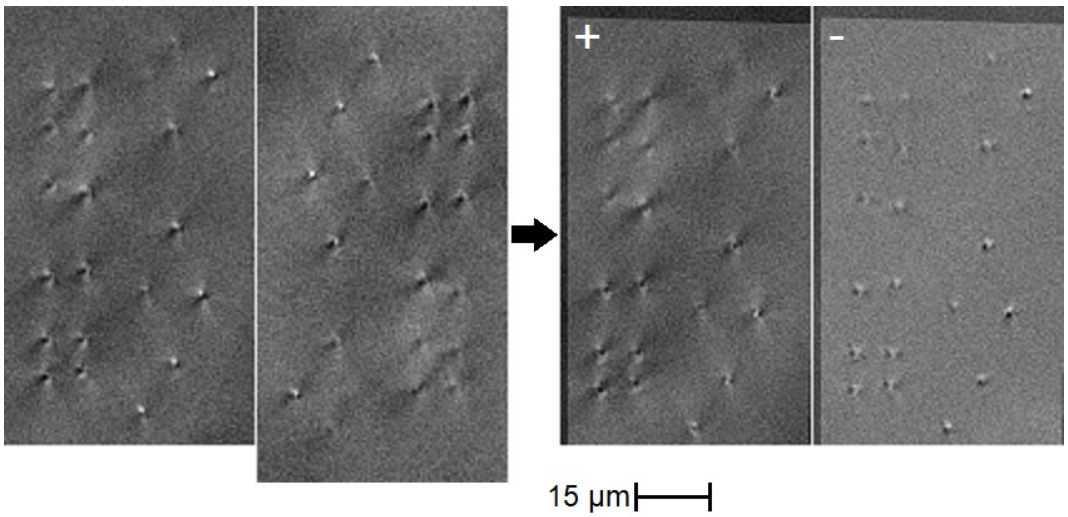

Figure 3.18: This figure shows the result of qDIC analysis for two rotations of the sample 180° apart from each other (left). One of these images is then rotated and translated to match the other and the result subtracted or averaged from its counterpart to create the following two images respectively (right). The greyscale is linear between -0.162 and 0.3072 for the first image, and -0.1461 and 0.2352 for the second and represents the phase difference in radians.

Chapter 4

Laser machining setup

4.1 Design

Fig. 4.1 is a diagram of the optical setup used during both laser machining, and absorption microspectroscopy analysis. The laser used was a 1064 nm EKSPLA PP-2250 Nd:YAG laser capable of firing 30 ps pulses either individually or at a rate of 20 Hz with pulse energies (E_p) on the millijoule scale. This was located in a separate lab so the laser was delivered via a relay using four mirrors to the optical table. The beam was then passed through a spatial filter (represented by two telescopes and a pinhole in the diagram) to remove any distortions or imperfections and to create a well-defined optical mode. Both the input iris and the pinhole were chosen to be smaller than the beam arriving at that point to allow a small amount of beam walk and spatial walk off. This reduces the beam intensity, but the pulse energy of the laser was around 100 times larger than was required for laser machining so this was not a problem. The telescopes consisted of a convex lens with focal length $f = 150\,\text{mm}$ and and concave lens of $f = -100\,\text{mm}$ and the distance between them was adjustable to create a variable focal length. The second telescope in the spatial filter was reversed to become a beam expander. Originally, the output beam from this filter was collimated until it reached the aspheric lens L4 at the window of the cryostat, but this was altered prior to the machinings detailed in this report to be slightly diverging. This was due to the difficulties encountered in machining within the sample without affecting the surfaces. For this reason, the beam was made to intentionally become diverging to overfill the lens at the front of the cryostat to provide a more homogeneous laser power spread at the sample surface.

The laser next passed through a Thorlabs WPH10ME half-wave plate (designed for use at 1064 nm) on a rotation mount located between silver-coated mirrors M1 and M2 so that its polarization could be altered from its default - vertical - but for earlier machining prior to site AF00/C this was not present. After this, optical density filters of value 0.25, 0.5, and 1.0 OD were used as required in the beam's path and rotated about a vertical axis in order to fine-tune the laser power by increasing the optical path length in the filter. This could be used to alter the pulse energy measured with the photodiode whilst

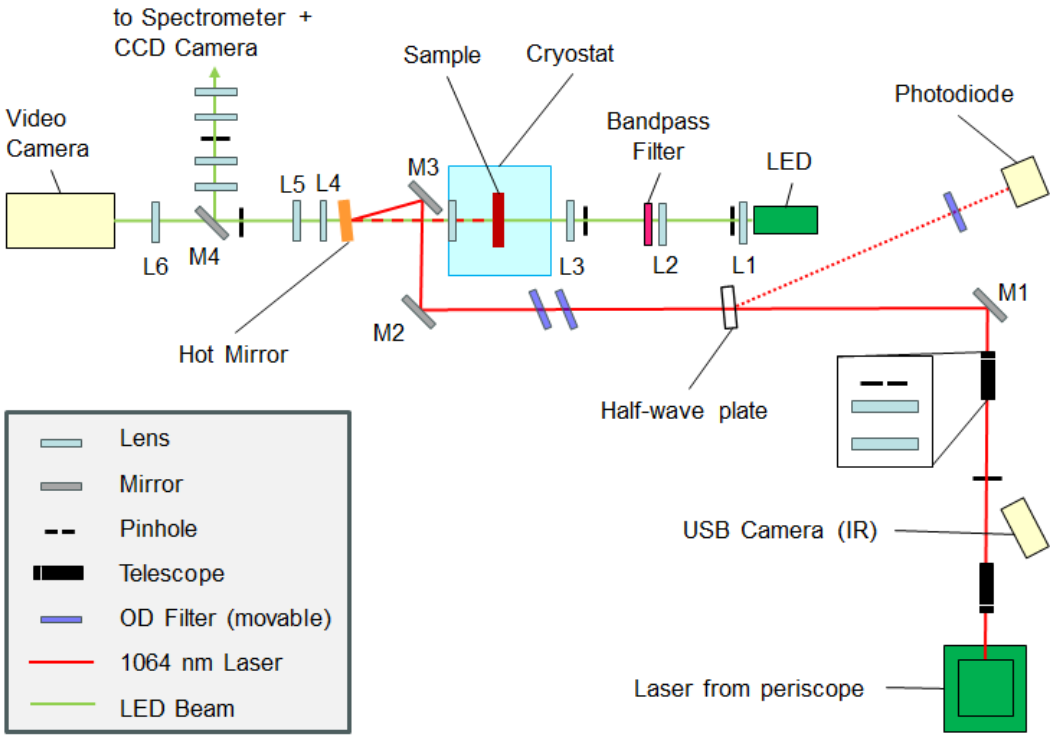

Figure 4.1: A diagram of the setup of the optical table on which laser machining was carried out. Both the laser path and LED path for absorption microspectroscopy are shown. The four mirrors are separately labelled. The distances and sizes in this diagram are not to scale.

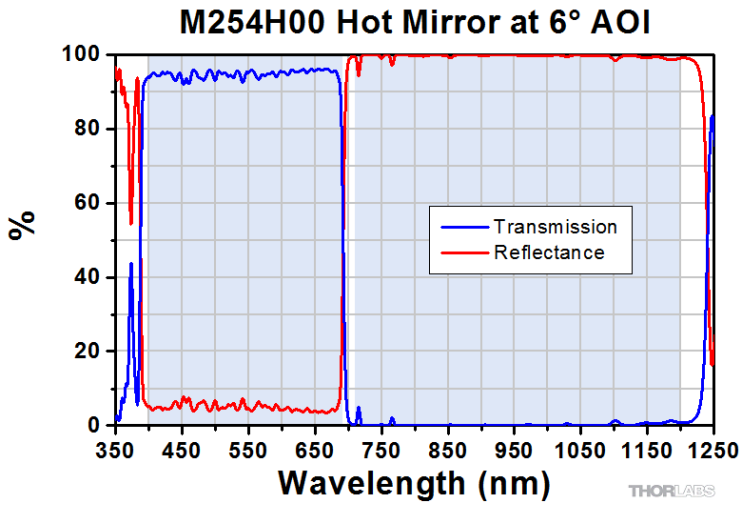

Figure 4.2: Reflectance and transmission curves for the hot mirror which was used to direct the machining laser onto the sample without obstructing the view of the sample from the video camera.

the laser was operating at a pulse rate of 20 Hz according to the procedure detailed in the Sec. 4.3. The OD filters were designed for the visible range and were individually characterised before use by taking 10 readings of pulse energy without an OD filter, and then 10 readings with the an OD filter using a COHERENT FieldMaxII-Top power meter. These values were then averaged and compared to work out the effective optical density of each of the filters. To ensure there was no significant drift in pulse energy over time, readings of pulse energy without an OD filter were taken regularly. The effective optical density at 1064 nm was found to be about 1.57 times larger than the given values which is expected for the material (Soviet NS8 glass). Finally, a Thorlabs M254H00 hot mirror was used to reflect the laser (see Fig. 4.2 for reflectance and transmission curves) through the lens L4 and into the sample which could be simultaneously imaged by the video camera as the hot mirror allowed the visible light through (94% transmission at 571 nm). The aspheric lens L4 was a Lightpath 345105 with a numerical aperture of 0.56 and a focal length of 5.5 mm. The sample was mounted on an Attocube ANC350 piezoeletric stage which was itself housed in a Montana C_2 Cryostation cooled to 6.5 K for most samples, and later to 5 K when the efficiency of the cryostat was improved after helium refilling; this was for the sample AM01 only.

A further change to the setup, as mentioned in Ch. 3, was the addition of lens L5 to the setup between L4 and M4 in Fig. 4.1. The purpose of this was to allow the video camera to acquire transmission images in the same plane as the machining laser focal point so that a video could be recorded of the sample at the same time as the laser machining occurred. The focal length of L4 was significantly different ($\sim 115\,\mu$m) for the LED illumination (of wavelength roughly 580 nm) as compared to the laser (of wavelength 1064 nm) due to the different wavelengths experiencing a different refractive index. An $f = 75$ mm lens (L5) was used here (shown immediately before the pinhole near M4 in

Fig. 4.1). Light from the sample in a plane further from L4 than the previous focal plane would be converging after L4 rather than be collimated. This resulted in an even greater convergence due to the lens after the hot mirror which resulted in a re-imaging before the $f = 75\,\text{mm}$ lens which was then used to create an image at the pinhole as normal. The videos captured using this updated setup were used to generate images that could be used to calculate absorption cross sections for the machinings.

In the last two sessions of laser machining, the profile of the laser had become affected by faults in the laser unit itself that could not be rectified on a workable timescale. As will be seen later, this resulted in the machining of line-like features rather than spots or circles. This could not be entirely solved with the spatial filter set up, but could be improved by it. Machining was carried out multiple times whilst varying the aperture of the pinhole and the input and output irises of the two telescopes forming the spatial filter to improve the quality of the laser beam profile without too much reduction in the laser power.

4.2 HRSI setup

Two cameras were mainly used in the characterisation of the machinings. One was a Sony TRV-620 camcorder which was used both to position the sample, and in later sessions to record the sample as the laser pulse was fired. These pulse videos were then used in later analysis. The other was a Pixis:100BR CCD camera used in conjunction with the Iris 2000 Mark II spectrometer built by Wolfgang Langbein and Stefan Schneider. Together these provide high resolution spectra ($\sim 10\,\mu\text{eV}$) over a narrow range ($\sim 0.016\,\text{eV}$). As mentioned in Ch. 3, the CCD camera was replaced for later sessions - this was because the old camera was registering too many dark counts due to not being able to maintain a vacuum and therefore sufficiently low temperature. The replacement camera was a Pixis: 400BR and improved the vertical range, quantum efficiency, and reduced the number of dark counts due to operation at a lower temperature.

The illumination was provided by a LXML-PX02 lime LED which was focused through a pinhole by lens L1, then was refocused by L2 through an Omega 575BP10 bandpass filter centred at the same wavelength as the spectrometer was set to collect - 572 nm - with a width of 10 nm (fine tuning of the centre wavelength was achieved by rotating the filter about the vertical axis). The beam was then focused through the far-field aperture which could be adjusted to alter the depth of focus of the image. Finally, the beam was collimated by L3 before it entered the cryostat to uniformly illuminate the sample. For imaging of the sample, L4 (the same used to focus the laser in machining) is the objective lens which collimates the beam, which then passes through the hot mirror and is focused onto the aperture next to mirror M4 by an Edmunds Optics achromat lens (L5) with focal length $f = 300\,\text{mm}$. The next lens, L6, was described above. Without M4 in place (see Fig. 4.1), the transmitted light could be picked up by the video camera after being colli-

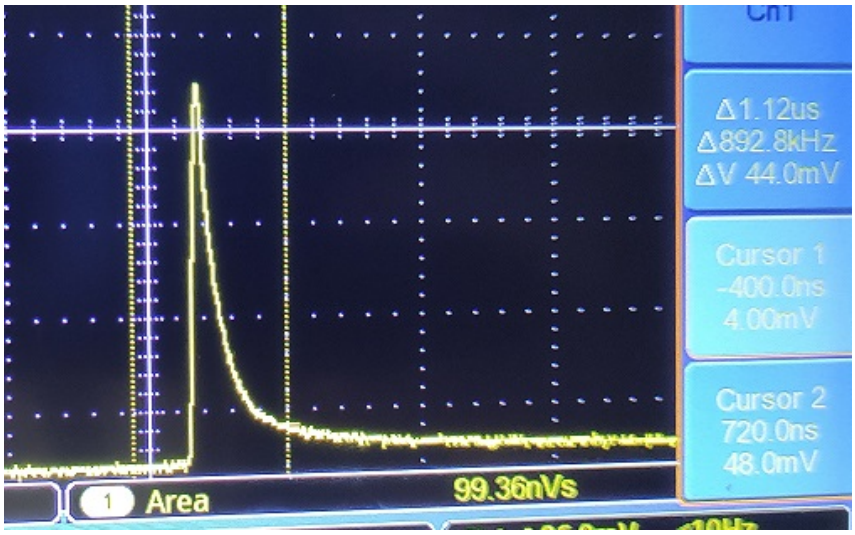

Figure 4.3: A trace shown on the oscilloscope connected to the photodiode. Vertical dotted lines show the range over which the peak was integrated in order to measure the energy of each pulse, E_p.

mated by another Edmunds Optics lens (L7) with $f = 200\,\text{mm}$. This was used both in positioning the sample and, for samples AL01 and AM01, recording the pulses. With mirror M4 in place, the light was directed towards the spectrometer through a series of lenses which imaged the sample onto the entrance slit of the spectrometer which helped to avoid vignetting [87].

4.3 Measuring pulse energy

At two points in this setup a small portion of the laser was either transmitted (at the hot mirror) or reflected (at the half-wave plate) where most of the beam was not. This made it possible to measure the energy of each pulse by the addition of a ThorLabs PDA100A-EC photodiode to the setup to pick up this signal. Originally, the transmitted laser light through the hot mirror was used but once the additional lens had been put in to allow the video camera to record the pulses, the transmitted laser was obstructed and the reflection from the half-wave plate was used instead.

The photodiode was connected to a Tektronix TBS1052B oscilloscope to record voltage against time. An example of the signal from the photodiode is shown in Fig. 4.3. The peak displayed on the oscilloscope would be integrated in the range -400→700 ns (where 0 ns is defined as the point at which the pulse was first detected). After a value was taken of the pulse, a further value was taken of the background, as this was non-zero, which was subtracted from the integrated peak of the laser pulse. This value was expected to be proportional to the pulse energy so just needed to be calibrated which was done as follows; before machining, the power meter (see Sec. 4.1) was put immediately in front of the cryostat and readings were taken from both the power meter and the photodiode over a range of pulse energies from the minimum that could be

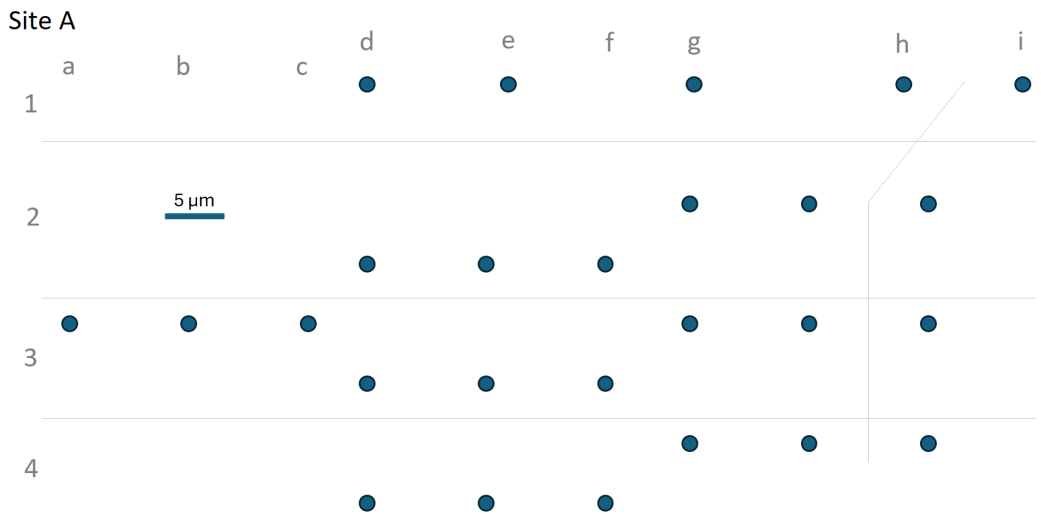

Figure 4.4: The pattern of the first set of laser machinings on the AF00 sample at site A. All pulses used were vertically polarized. Letters and numbers in grey are used to identify each individual machining; thin grey lines are also included to make it clear which labels apply to which machinings.

detected by the photodiode up to energies far exceeding those that would be used in machining. This was also done for both 0° and 45° rotation of the half-wave plate as this also resulted in a small decrease in signal at the photodiode. Readings from both the photodiode and the power meter were plotted against each other to confirm that their relationship was linear, and the conversion factor between the two variables was found. In this way, the photodiode could be used to measure the energy of each laser pulse.

4.4 Laser machining

Laser machining varied depending on the properties of the samples, these include: thickness, natural/synthetic sample, and defect concentration. These will be elaborated upon in the following subsections. It is also believed that surface composition of the samples has an effect during machining, but this would be confined to specific regions of samples, not to a sample as a whole. Below is an account of the laser machining done on each of the samples with a focus on those for which further analysis is included in Ch. 5 and 6.

4.4.1 AF00

Different machined sites on a sample are denoted in the following using capital letters. The first set (at site A) included here is the first set in which machining in the middle of the sample without affecting the surfaces was first achieved. The location of this set is represented in Fig. 3.2 by the middle green mark where the thickness was measured to be around 120 µm. This machining set consisted of a row with varying laser focal depths and pulse energies which

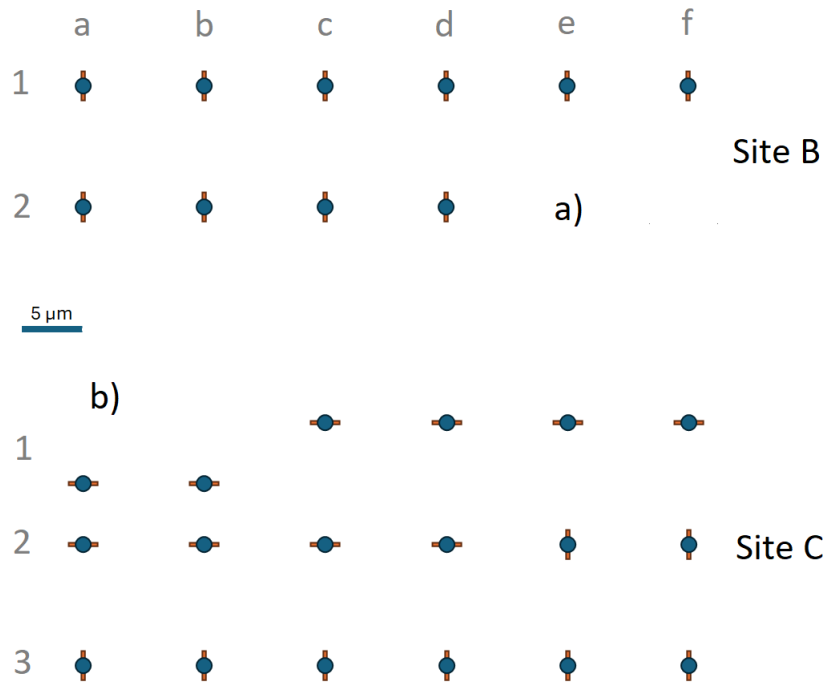

Figure 4.5: A diagram showing the pattern in which the two sets of laser machinings at sites B and C were done on the AF00 sample. Lines show the orientation of the laser polarization for each machining. a) machinings at site B consisting of two rows. b) site C machinings, a set of 3 rows, the first two of the top row were machined too close to the middle row so this was adjusted for the machinings 1c to 1f. The scale included applies to both sites.

were altered depending on whether the previous pulse had a visible effect or affected one of the surfaces. For example, if the pulse affected the front surface only, the focal point of the laser was shifted to be closer to the back surface by 2-5 µm (or to a depth between two depths known to have affected either surface). If a pulse affected both surfaces, the subsequent pulse would be decreased in energy by about 20% (and increased by the same amount for pulses with energy too low to cause any effect at all). Once mid-sample-only machining was achieved, groups of 3 machinings at the same depth and pulse energy were machined roughly 10 µm vertically below this initial row to test the repeatability. Further mid-sample-only machinings were achieved multiple times and it was found that the range of depths at which this was possible was <1 µm. A diagram showing the relative positions of these machinings is shown in Fig. 4.4 . Only HRSI data and transmission images were acquired of this set as this region was damaged by the laser after machining during laser alignment.

The next set was on a different part of the sample (site B, shown in green on the right hand side of Fig. 3.2) and had the same aim as set A. The thickness of the sample varied across this region from 120–137 µm. It consisted of two rows, one of 6 and one of 4 machinings, and small adjustments were made to

the focal depth and pulse energy after each machining in the manner described above. The first row (of 6) was performed with laser pulse energies from 1.94 - 2.18 µJ whilst the row of four beneath it used pulse energies from 0.81 - 0.92 µJ. Mid-sample-only machining was not achieved and the effect of changing the focal depth was inconsistent - the laser for the penultimate machining was focused closer to the front surface than for the final machining, but affected the back surface and the final one affected the front. This lack of consistency was attributed to local sample effects such as inhomogeneous defect concentrations or surface compositions. The middle of the sample was nevertheless affected, albeit along with the surfaces, so analysis was still performed. These machinings also feature later in FIB-SEM.

Prior to the final set of machinings a half-wave plate was installed to allow for the investigation of the effects of the orientation of the linear polarization of the machining laser (see Sec. 4.2). Asymmetric effects had been picked up by the HRSI scans (more on this later) which may have been evidence of an effect of the orientation of the linear polarization of the machining laser pulse. The location of this set is shown in the leftmost green mark in Fig. 3.2 where the thickness was measured to be 135 µm (site C). Here, three rows were machined (the first two of the top row were a little too close to the middle row, see Fig. 4.5b). The bottom row was machined with vertical polarization along with the final two of the middle row. The rest (top row and the first four of the middle) used horizontally polarized laser pulses. With the exception of the first machining on the middle row which was created by a 2.0 µJ pulse, these were all machined by laser pulses of 3.2 ± 0.4 µJ.

One additional set from this sample is included in Sec. 6.2. These machinings were part of a row and were performed early in this project to find the correct value of the offset that was required between the focal distances of the laser versus visible light, not for the purposes of mid-sample machining (referred to as site X). For this reason, the exact pulse energies used in machining are not known, but are estimated to be around 8-9 µJ. The reason they are included here is that they were later found to show interesting results in orthoexciton scans, they are otherwise not explored further in other types of analysis.

4.4.2 AG15

Exclusive, mid–sample machining was routinely achieved with this sample due to the increased thickness. Fitting of the Rydberg series was still preferential, however, and so other samples were preferred as candidates for laser machining. Nevertheless, one set of machinings is still included here. The thickness measured at this region was 225 µm. The machining consisted of two 'cross' structures in which four machinings were performed around a central point at a distance of 10 µm from that point (above, below, left, and right). This was meant to create a combined strain effect on the region that the machinings enclosed. The pattern was machined twice; one with a radial laser polarization, and one azimuthal polarization (see Fig. 4.6). All used pulse energies of

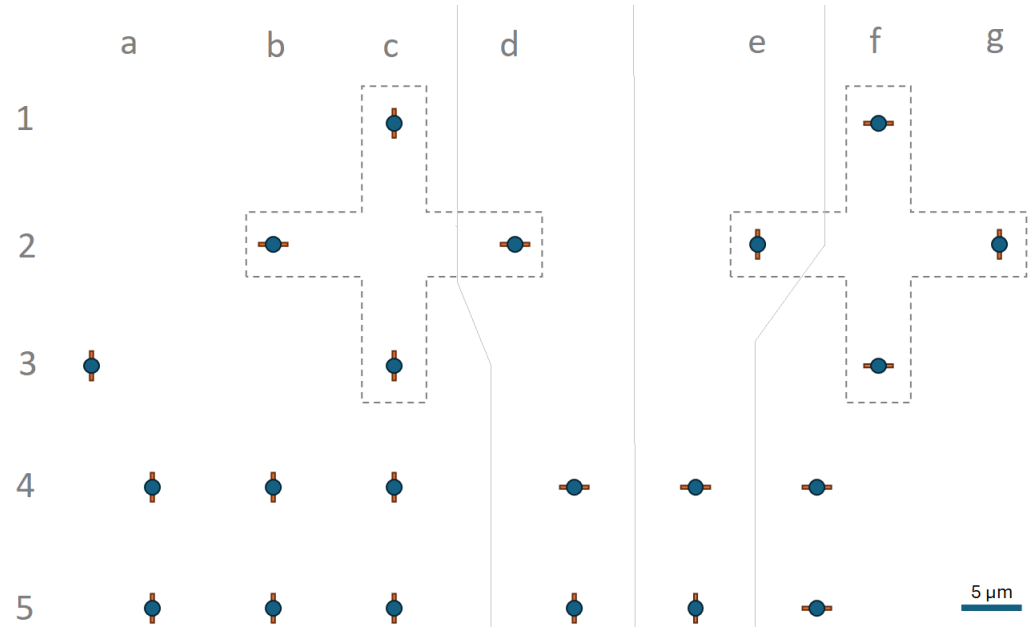

Figure 4.6: A diagram of the arrangement of machinings on the AG15 sample including laser polarization direction. The cross structures are on the top with two rows of six machinings beneath them

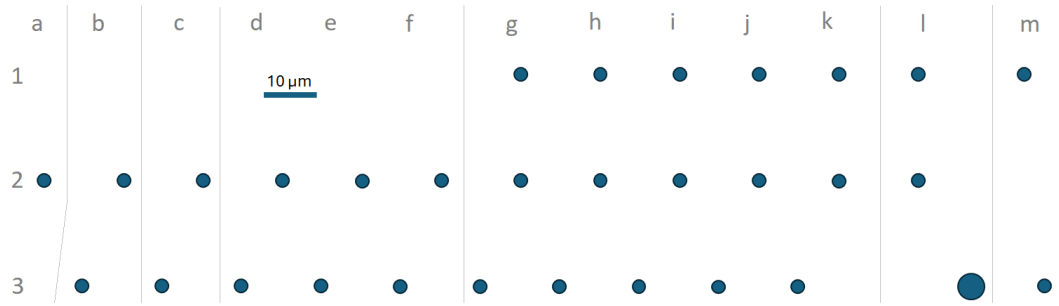

Figure 4.7: A diagram of the arrangement of machinings from the AF13 sample. All used horizontally polarized laser pulses.

$4.9 \pm 0.4\,\mu J$. Below this were two rows machined using a higher pulse energy of $11 \pm 1\,\mu J$ (see Fig. 4.6). The final three of the first row and the final one of the second row were machined with horizontally polarized laser pulses, the rest were vertically polarized.

4.4.3 AF13

One set in this sample was successful in achieving many machinings within the sample even whilst varying the depth of focus of the laser. This provided some useful findings using qDIC analysis and so is also included here. This set was made up of 3 horizontal rows of 10, 12, and 12 machinings from top to bottom in a region of the sample with thickness measured to be 125 µm (see Fig. 4.7). The purpose of the first row was to find the machining threshold energy by keeping other settings such as the laser focus depth constant and decreasing

the pulse energy until machining ceased to occur according to:

$$E_n = E_0 \exp(-0.1n) \tag{4.1}$$

where E_n is the pulse energy used in the n-th sequential machining, and E_0=1.39 µJ. This resulted in machinings that affected the middle of the sample, but also the front since the laser's focus depth was not correct. This also meant that the threshold found would not necessarily be correct when the laser was focused at the correct depth. Therefore, for the second row, pulse energies of 1.2 ± 0.2 µJ were used and the depth of laser focal point varied until surface machining occurred (after about 20 µm). The purpose of the final row was another attempt to find the threshold pulse energy for machining using Eq. 4.1 and a starting value of $E_0 = 1.23$ µJ. While this did result in mid-sample machining, every pulse also affected the front surface meaning the chosen depth was not correct. As with the first row, the threshold energy found in this case would be lower than the intended value. Despite this, much mid-sample machining was achieved and the resulting findings using qDIC are shown later in Ch. 5.

It is difficult to say why it was so difficult to find the correct laser focus depth. It could be that measuring where the surfaces were (and by extension the sample's middle) was not particularly accurate (±2 µm). This measurement was done using the LED transmission light and video camera; with the LED on, the far-field iris was opened fully to minimise the depth of focus. The stage was then positioned so that a surface of the sample was in focus on the video camera and the coordinate on the piezoelectric stage corresponding to this depth was recorded. Additionally, fluctuations in the sample's thickness or tilt in the sample would introduce an inaccuracy here. Another possibility was mentioned earlier and that is the surface composition. There have been many instances where the depth of the machining has suddenly jumped to one surface or other with little-to-no change in the laser focus depth and little change in location on the sample. This would suggest that the composition on the surface had become significantly different and that these changes are specific to very localised areas. It was thought that this could be addressed with chemical etching which was attempted with mixed results (see Appendix A).

4.4.4 AL01

Site A in this sample explored the effects of pulse energy by milling rows of machinings such that the n-th machining was done with a pulse energy:

$$E_n = E_0 \exp(0.1(n-1)) \,, \tag{4.2}$$

where $E_0 = 0.4$ µJ which was determined beforehand to be in excess of the energy required to reliably machine with every pulse and was done for values of $n = 0 \rightarrow 11$ increasing the pulse energy exponentially. The separation between machinings was 15 µm to ensure each was spatially isolated from other sufficiently to suppress any effect of existing machinings on the machining's

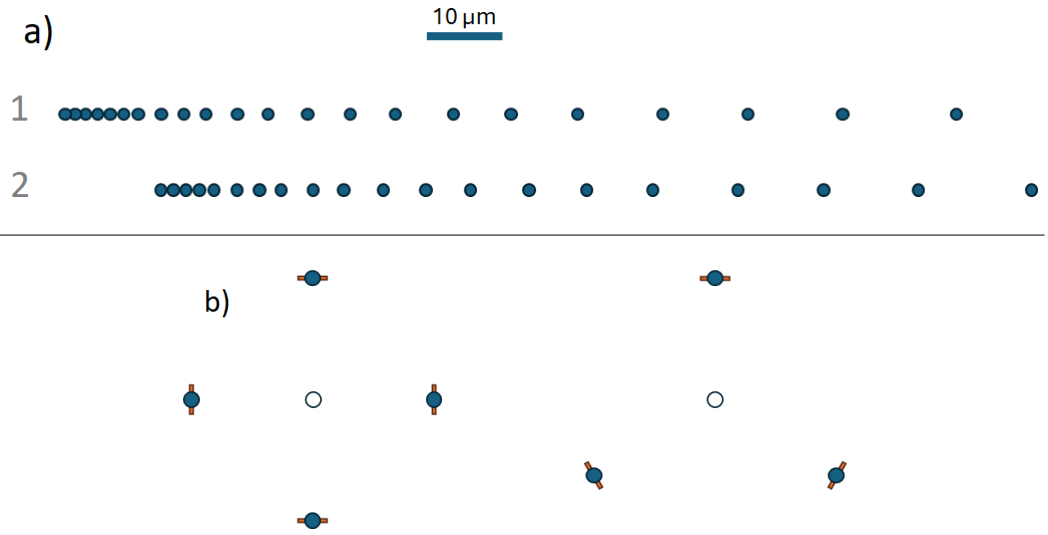

Figure 4.8: A diagram showing two sets of machinings in the AL01 sample. a) is the first set where the spacing was varied. The top row used vertically polarized pulses and the bottom used horizontal polarization. b) shows examples of the structures machined around a central point with radii 8 and 4 µm. Each structure was separated by a distance of 15 µm and laser polarizations perpendicular to those shown in the image were also used.

outcome. This was both to investigate the effects of changing the pulse energy, and also to determine the threshold pulse energy for machining. Machining in this manner was carried out for both vertical and horizontal laser polarizations at a region of the sample roughly 100 µm thick.

Similarly, in the site B, the distance between the machinings was decreased according to:

$$D_n = D_0 \exp\left(\frac{1-n}{8}\right) , \tag{4.3}$$

where D_n was the distance from the n-th machining to the $(n+1)$-th machining and $D_0 = 15\,\mu\text{m}$ which had been determined to be large enough that machinings could be considered to be independent of each other. This was to investigate the cumulative effect that the machinings may have on the surrounding crystal due to induced strain. Again, this was performed separately for vertical and horizontal laser polarizations. The sample thickness at this site was 110 µm. The vertically polarized pulses had energies of $0.5 \pm 0.05\,\mu\text{J}$ and consisted of $n = 22$ machinings whilst the horizontally polarized pulses were of energy $0.85 \pm 0.1\,\mu\text{J}$ and consisted of $n = 20$ machinings. Fewer machinings were performed in the second instance since it was clear in the first row that previous machinings on the row were interfering with machining. The pulses energies used in each row were intended to be the same but were different due to a calculation error.

The reason machining on site C was performed was for later examination

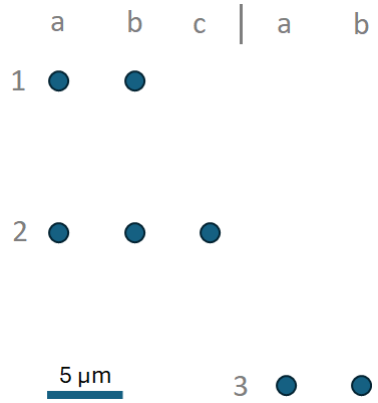

Figure 4.9: A diagram showing the pattern of selected machinings in the AM01 sample.

with FIB-SEM. These were machined at a 100 µm thick part of the sample and consisted of four rows each machined with pulse energies of about 0.4, 0.5, 0.7, and 0.9 µJ. The FIB-SEM analysis was not performed on these due to time constraints, and transmission videos of them appear to show only surface machining.

Finally, structures comprised of multiple machinings were created. These were done both in triangular and square shapes where the polarizations of the laser pulses for each were either all in the same plane as the centre of the structure, or orthogonal to this plane (see Fig. 3.7). These structures were created in two sizes with the distance from the central point to each machining (r) being either 2 µm or 4 µm. Similar to the distance-varying set, this geometry was chosen to create regions of high strain using three or four machinings rather than just two. The triangular shaped structures used pulse energies of 1.15 ± 0.1 µJ whilst the rectangular ones used 0.6 ± 0.1 µJ (these were intended to be the same energy, but the compensation for the effect of rotating the half-wave plate on the pulse energy was incorrectly compensated). These structures were machined in regions of the sample of thickness 70 and 45 µm for the triangular and rectangular structures respectively.

4.4.5 AM01

In all 7 cases of mid-sample machining, the machinings were test machinings to check that some quantity (e.g. depth, laser power) was correct before commencing with machinings proper. The relative positions of these are shown in Fig. 4.9. Data relating to the laser machining of this sample is included in Sec. 5.4.

Besides these test pulses, laser machining in this sample consisted of four structures similar to those shown in Fig. 3.7, and rows with varying pulse energy, laser focus depth, and laser polarization. There was also a row of points machined with the laser focused on the surface of the sample and the pulse energy varied to find the threshold energy for machining on the surface which was expected to be considerably less than for machining in the middle.

For the majority of cases, the pulse energies used lay between 0.3 and 0.75 µm with the exceptions being for the surface machinings which used a pulse energy of roughly 0.2 µJ. As with the previous sample, all laser shots were recorded so these machinings were included in this type of analysis.

Chapter 5

Non-excitonic effects of laser machining

5.1 Birefringent effects

In this section the focus will be on the images resulting from the qDIC analysis of samples AG15 and AF13. As the thickest samples, these were the ones for which mid-sample machining was the easiest and thus provided the most amount of machinings appropriate for this kind of analysis given that it aims to measure birefringence induced due to strain within a sample. Images showing the phase shifts created by the machinings in these two samples are given in Fig. 5.1 which gives a direct indication of the birefringence in the sample according to the method outlined in Sec. 3.6. Maximum and minimum values of the phase shift ($\delta_{\phi,max}$ & $\delta_{\phi,min}$) were taken from the two images (excluding the large burn in the bottom right of the AF13 image) in order to calculate the change in refractive index due to laser machining according to the equation:

$$\Delta n = \frac{\Delta\phi\lambda}{2\pi L} \tag{5.1}$$

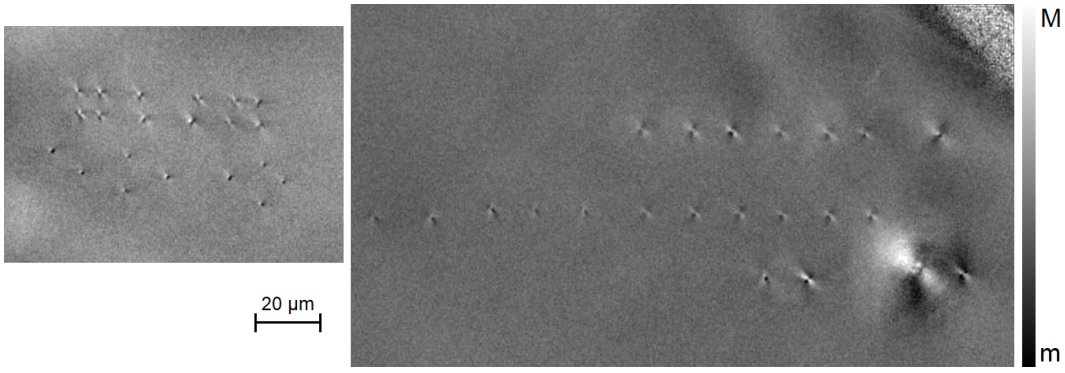

Figure 5.1: qDIC images of machinings in sample AG15 (left) and AF13 (right). The pixel brightness corresponds to phase shift. Minimum (m) and maximum values (M) are $m = -0.1685$, $M = 0.1455$ for AG15, and $m = -0.1754$, $M = 0.2512$ for AF13 (all in radians).

Sample		Max.	Max. >5	Min. >5	Min.
AG15	δ_ϕ/rad	0.136	0.0964	-0.0973	-0.159
	Δn	0.0019	0.0014	-0.0014	-0.0022
AF13	δ_ϕ/rad	0.201	0.138	-0.122	-0.165
	Δn	0.0028	0.0.0019	-0.0017	-0.0023

Table 5.1: Values of phase shift and refractive index change for laser machinings in sample AG15 and AF13.

where λ is the wavelength of the transmitted light, and L is the distance over which the phase shift occurred - though this cannot be measured. The effective length will be approximately the depth of field of the imaging which can be estimated with the expression $\lambda n/\mathrm{NA}^2$. For $\lambda = 650\,\mathrm{nm}$, NA=0.5, and n=2.9, this gives a length of $L = 7.5\,\mu\mathrm{m}$. Additional values of $\delta\phi$ were also obtained since the maximum and minimum values were only present for single pixels that were relatively far removed from other values so could represent atypical results. These additional values were found by binning the values of all pixels in the area occupied by machinings across the range given by $\delta_{\phi,max} - \delta_{\phi,min}$ into 128 bins and using the additional criterion that a bin's count must be at least 5 to be accepted. This value is denoted as $\delta_{\phi,>5}$. These results are shown in Table 5.1. Despite being machined with far lower pulse energies (<2 µJ rather than up to 11 µJ) AF13 showed a larger phase shift due to laser machining. This was the thinner of the two samples and surface machining did occur on some occasions. Out of focus surface effects may have contributed to the value given here.

As detailed in Ch. 3, further images created during the course of qDIC analysis were made by the combination (either the average or difference) of two phase difference images with reversed shear direction (in practice, the samples were rotated in the plane of their surfaces by 180° in order to achieve the same outcome). These are referred to hereafter as birefringence and gradient qDIC images respectively.

These two samples were the thickest two and therefore mid-sample machining was far easier to achieve (particularly without affecting a surface). This is important as there is a specific effect on the birefringence of the sample surrounding a laser machining that was only apparent for mid-sample machining - an anisotropic effect evident in the birefringence images (curiously for specific sample rotations, more on this later). This effect can be seen in Figs. 5.2 and 5.3, where a positive phase difference is observed along one axis passing through the machining, and the opposite effect is seen along the axis perpendicular to this. This is consistent with a uniaxial, tensile strain along one of these axes which causes a compressive strain in the other axis (or vice versa) related to the original strain by Poisson's ratio, ν_p, by: $\epsilon_{xx} = -\nu_p \epsilon_{yy}$. Even if not uniaxial, the strain is, at the very least, asymmetric so the question remains, however, how does a laser pulse result in a uniaxial strain with an orientation consistent across all machinings? One possibility is that the dam-

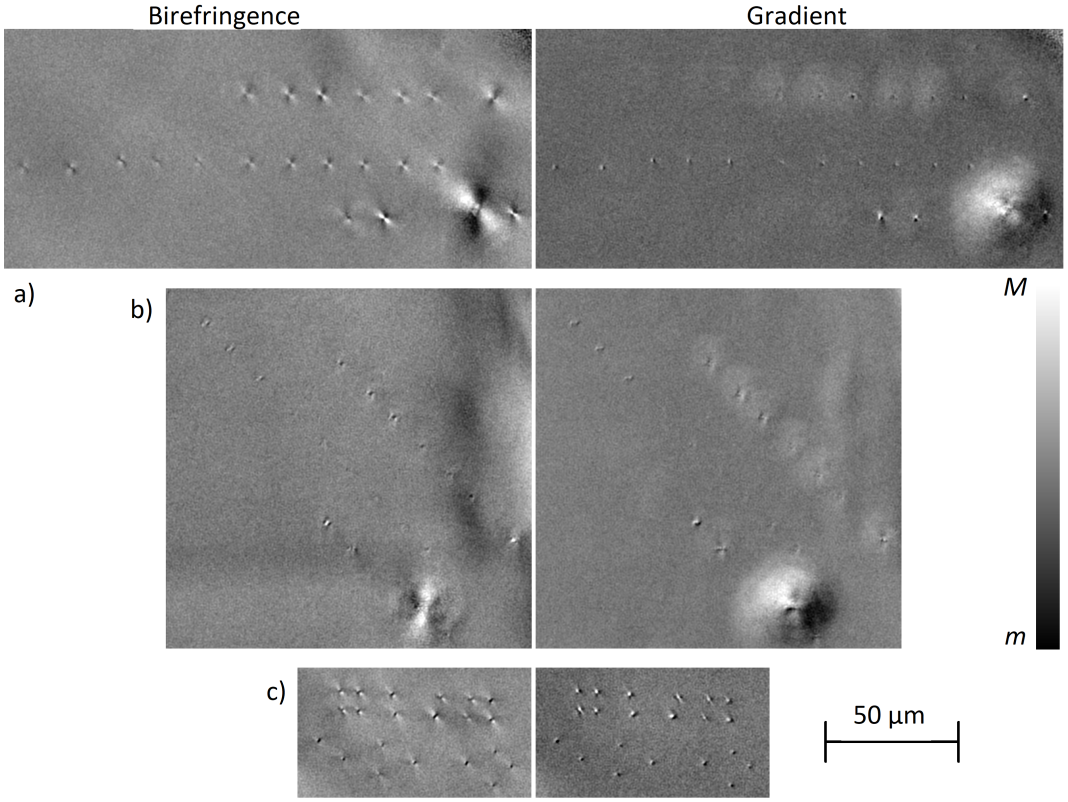

Figure 5.2: Birefringence (left) and phase gradient (right) qDIC images for samples AF13, shown in a) and b) the same site rotated 45°, and AG15, shown in c). The greyscale represents the phase difference ranging from a) $m = -0.15$ to $M = 0.12$ b) $m = -0.16$ to $M = 0.11$ and c) $m = -0.10$ to $M = 0.18$ radians.

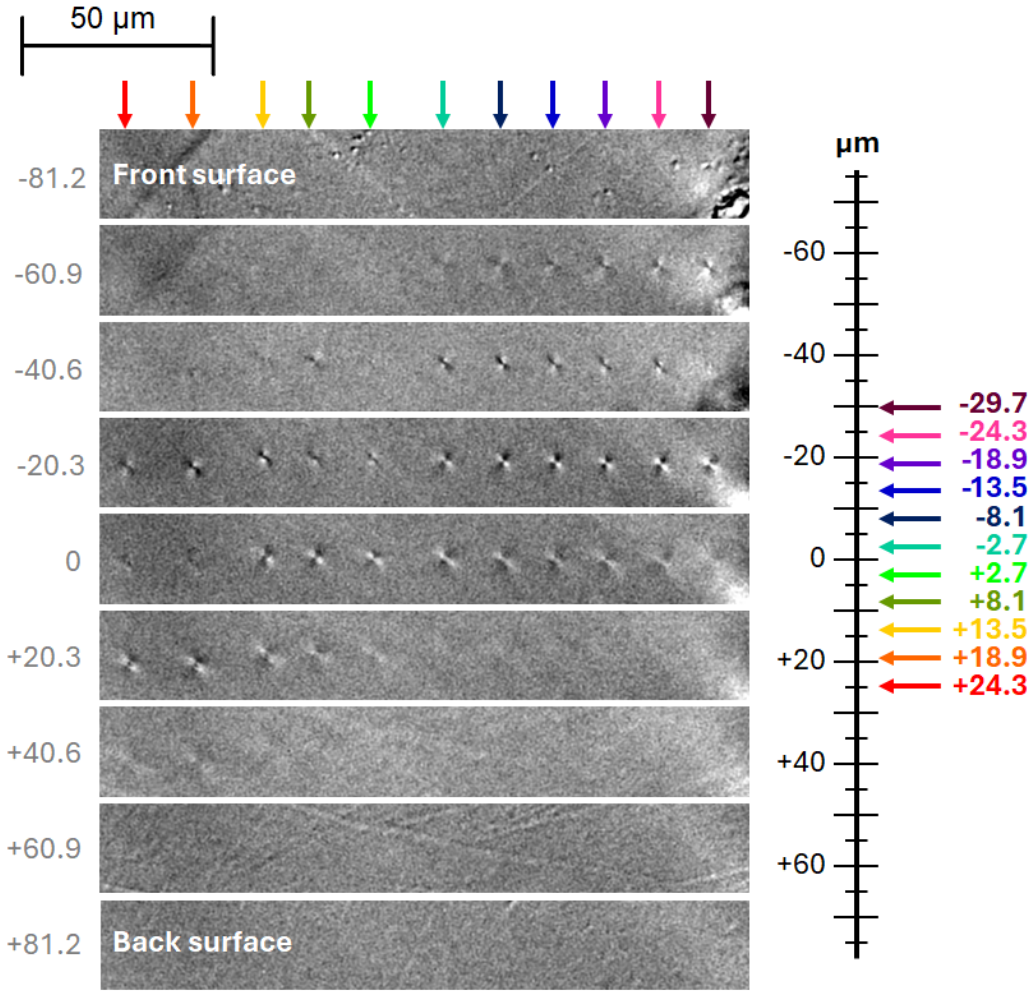

Figure 5.3: A focus stack of birefringence images through AF13 from the front surface to the back in which the phase difference is represented by the greyscale from between ±0.065 rad. The individual images are separated in depth by 20.3 µm (taking into account the refractive index). The depths at which the machining was intended are shown on the scale on the right. Numbers on the left show the coordinates of the planes in which images were captured for qDIC relative to the centre of the sample measured in µm.

age itself is asymmetric and is somehow aligned with some axis of the crystal - though why this might occur in an isotropic crystal is unclear. Fig. 5.2c shows the birefringence and gradient qDIC images for AG15 in which radial and azimuthal laser polarizations were used to create the 'cross' features (see Sec. 4.4.2). This shows that the orientation of this birefringence pattern is not dominated by an effect of laser polarization. It is worth noting that, for AF13, the light and dark axes on this pattern flip depending on the depth in the crystal as shown in Fig. 5.3 which shows cropped images of the middle row of machinings from Fig. 5.2a at various depths compared with the intended depth of each machining. For machinings deeper in the crystal, the 'light' axis is top left to bottom right and the 'dark' axis is perpendicular to this - bottom left to top right, but this is reversed for images taken of the same machinings but closer to the front surface of the sample. This was not seen for other machinings and the reason for it is unknown.

As can be seen in Fig. 5.2b, the orientation of the crystal relative to the shear direction was important for seeing this anisotropic effect insomuch as the shear direction had to be parallel to one or other of the light or dark axes in order for them to be seen. When the sample was rotated in-plane by $\pm\pi/4$ radians relative to a position where the pattern was seen, the pattern was either greatly reduced or disappeared completely as shown in Fig 5.2. The reason for this is that the polarization of the ordinary and extraordinary beams that pass through the sample are along and orthogonal to the shear direction. At a certain orientation of the crystal compared to the shear direction, the beams' linear polarization directions are aligned with the fast and slow axes in the birefringent crystal. At a $\pi/4$ rotation from this position, both beams will become equally misaligned from both fast and slow axes (assuming the axes are orthogonal) and thus will experience the same refractive index resulting in vanishing phase difference.

The difference images show a much smaller affected region than the birefringence images. FIB-SEM images will later show that the damaged part of the sample is small - smaller even than the shear distance in qDIC. Firstly, this shows that the birefringence effect extends beyond the machining which itself is shown in the gradient images. But what this means for this analysis is that, for the central point of each machining, there is a significant difference in the refractive index This is not due to birefringence, but the formation of a void or a different material entirely.

Confirmation of the a connection between the orientation of the strain patterns with the crystal axes is worth pursuing and could be done with Laue imaging of the samples. This being the case, the superposition of the strain fields caused by the four machinings in the cross-like features of AG15 would not cause the same strain shift in the centre as might be expected if the pattern orientation were due to laser polarization, but cancel each other out. Therefore, structures made of just two machinings aligned with the light/dark axes of the strain patterns which are close together (but not so close that machining of the second causes further damage at the first i.e. 2-5 µm) could be a better alternative to creating localized traps (see Fig. 5.4). If strain fields of

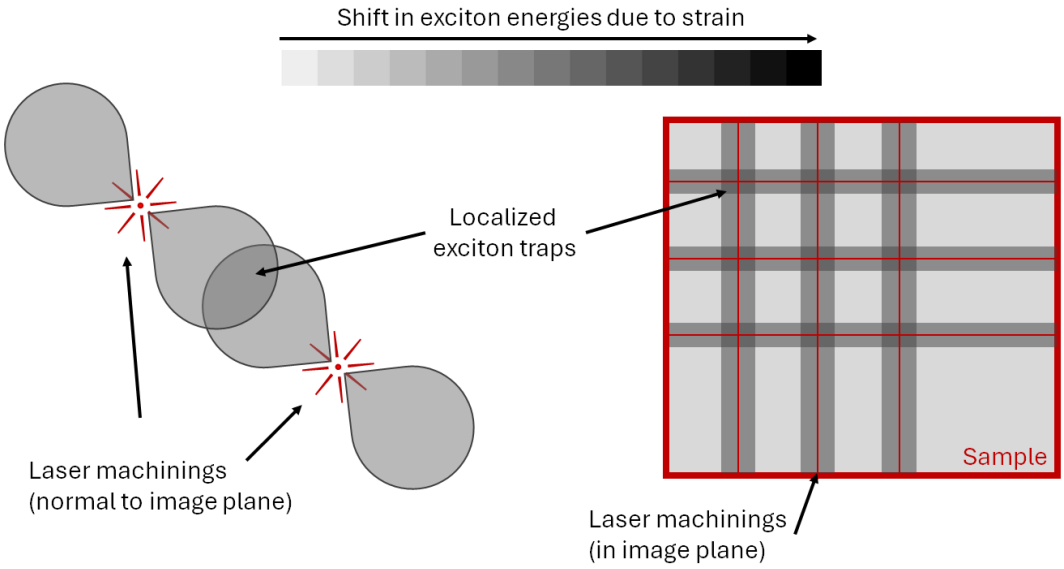

Figure 5.4: Two diagrams showing how the superposition of the strain fields due to laser machining could create localised exciton traps. On the left, machinings normal to the plane of the page cause the exciton energies in the region between them to shift by a greater amount than if there were just one machining. On the right, six machinings performed in the plane of the page (3 vertically and 3 horizontally) create 9 localized regions of high strain at their intersections showing the potential for arrays of exciton traps.

adjacent machinings can be superposed in this way, one could also consider laser pulses delivered to the same point in a bulk crystal from orthogonal angles such that the strain is singularly large at the point of their intersection, and localized enough to trap a single, high-n exciton; a single crystal could even contain 2D or 3D arrays of confined electrons; a simplified version of this is shown in Fig 5.4. Alternatively, laser machining could be employed alongside other methods of confinement (e.g micropillars containing only sections of laser-induced damage could also contain sufficiently localized strain).

5.2 Cu_3O_2 formation

As detailed in Sec. 3.4, the confocal Raman imaging of the machinings provides data on both the change in the Raman modes and photoluminescence of the sample. Fig. 5.5 shows the result of this analysis for AF00/B-4a (sample AF00, site B, machining 4a, see Sec. 4.4.1). Figs. 5.5a,b show spectra for both the machined and unmachined parts of the sample in the PL and Raman regime respectively. Figs. 5.5c,d show a weighted difference between the spectra above them to highlight the change in the spectra due to laser machining. This was obtained by multiplying one spectrum by a constant before subtracting. The constant used was found manually by trying different values and finding the one for which the Raman peaks disappeared. The spectra given were

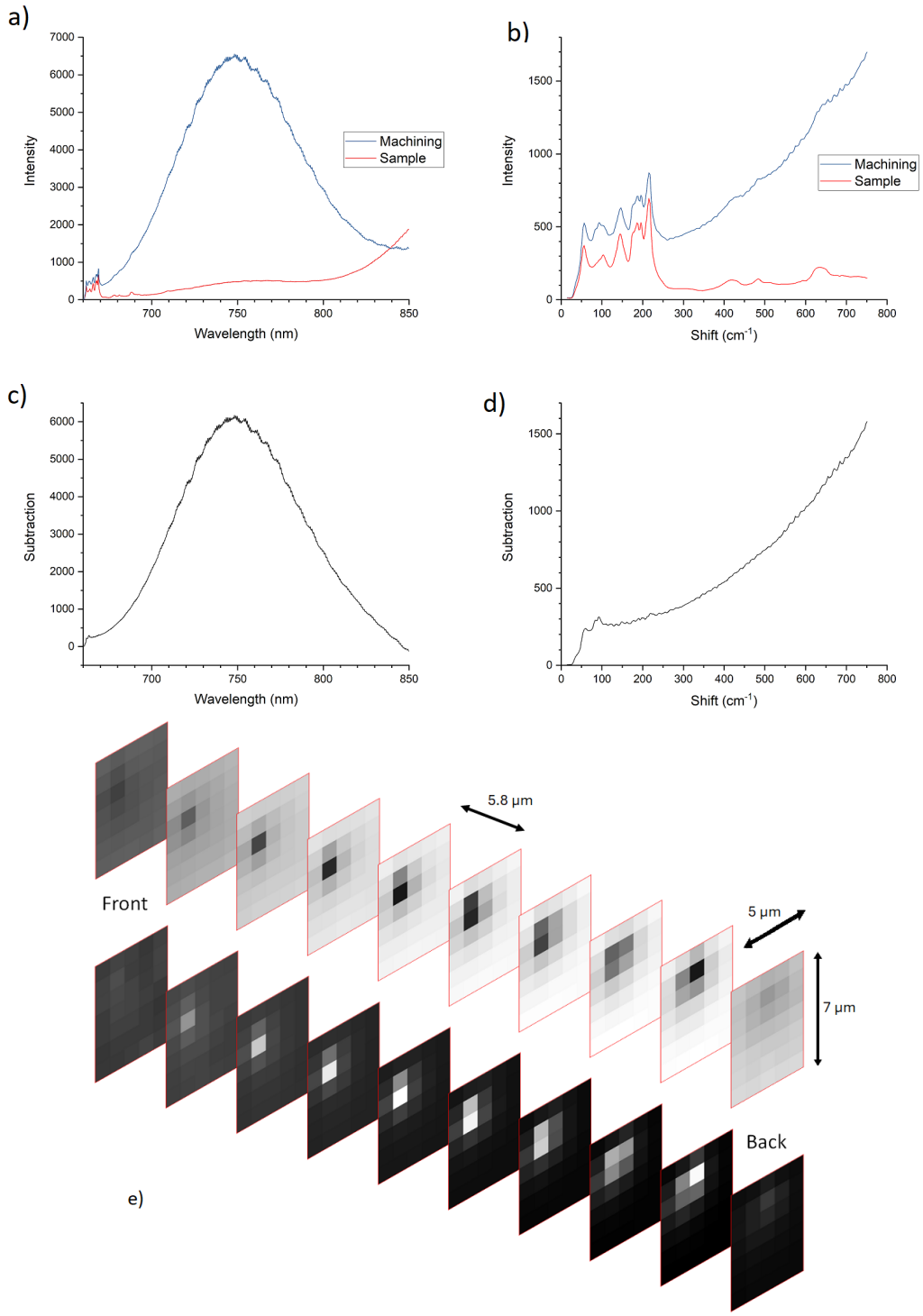

Figure 5.5: a,b) Raman spectra corresponding to the machining AF00/B-4a and the surrounding sample. c,d) a weighted difference between the spectra to show the change due to laser machining. e) concentration distributions of the two components showing which is the unmachined (top) and machined (bottom) material. Each pane measures 5 µm×7 µm (data rotated during analysis) and are separated by depth intervals of 5.8 µm (taking into account refractive index at 660 nm). Greyscale ranges from 0 to 1 for relative concentration.

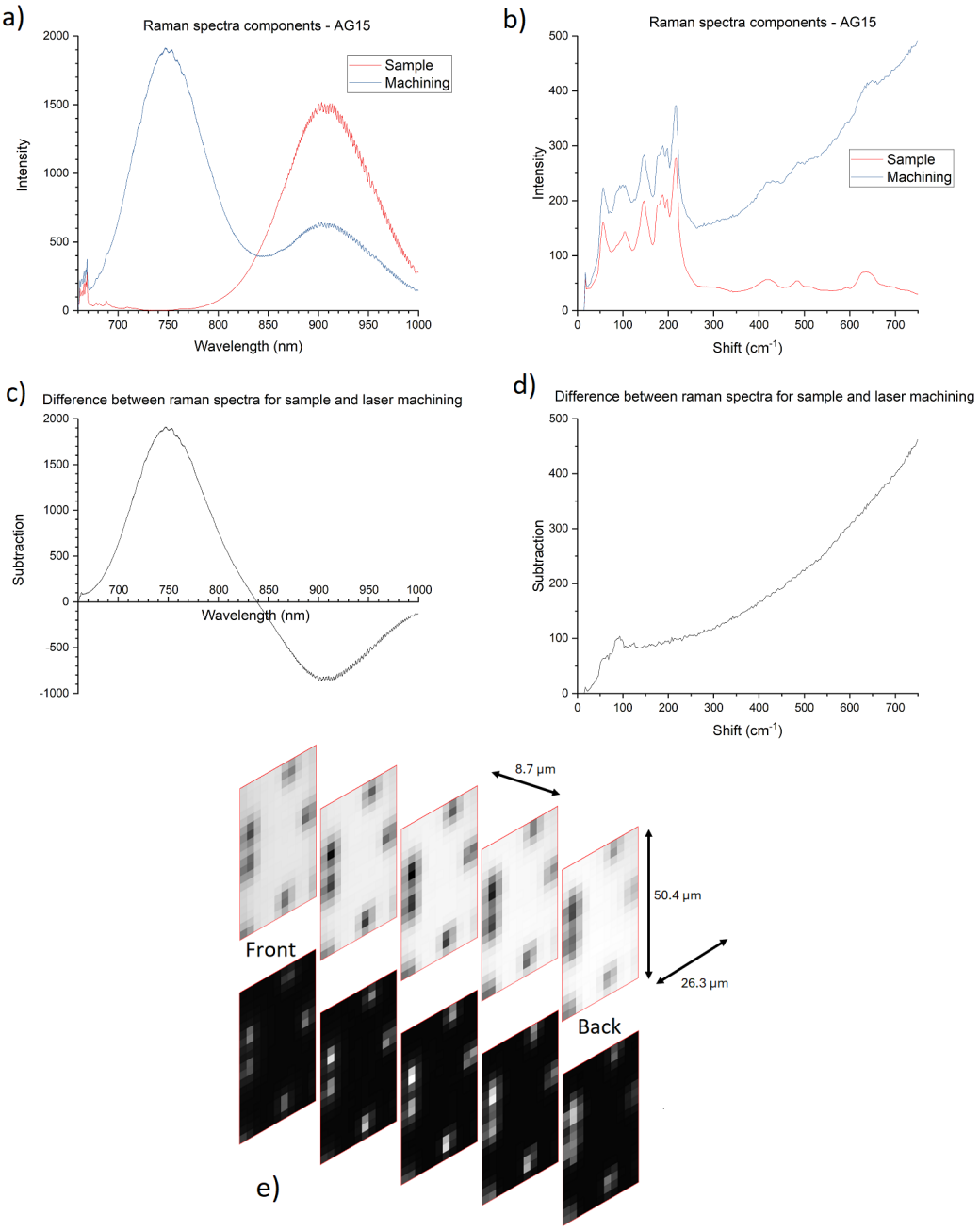

Figure 5.6: As Fig. 5.5 but for machinings AG15-2b, 3a, 3c, and 4a-c. The panels are 26.3 µm× 50.4 µm.

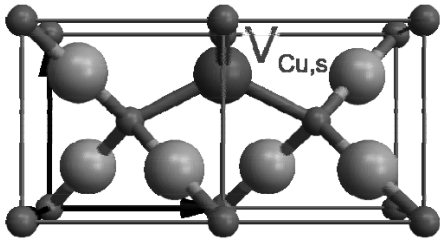

Figure 5.7: Two adjacent cubic unit cells of Cu_2O with a split copper vacancy (V_{Cu}^{split}) where a copper atom is split between two adjacent copper sites in the lattice. Large spheres represent copper atoms while small ones represent oxygen atoms. [55]

attributed to the machined and unmachined material using Fig. 5.5e which shows a stack of images of the relative concentrations of material with a given spectra (blue spectrum for the upper stack, and red for the lower). Since the scans took place over a point-like machining at multiple depths, it is clear that the first component is related to the unmachined material and the second to the machined material. These attributions are the ones used in the spectra.

The first 10 depths at intervals of 5.8 µm (corrected for refractive index $n = 2.9$ for $\lambda = 660$ nm [69]) were scanned over a 7 µm×5 µm region. In the Raman spectral range (up to 750 cm^{-1}), there is a clear peak at 94 cm^{-1} associated with the laser machining. This peak corresponds to the T_{2u} phonon mode which is not Raman active in a defect-free Cu_2O crystal due to symmetry. The presence of defects breaks the crystal symmetry and allows for the observation of such vibrational modes. In the case of the 94 cm^{-1} peak, only one type of defect is able to render the mode Raman active, and that is the V_{Cu}^{split}defect [54, 55] which is a split copper vacancy where a copper atom is shared between copper locations in two adjacent unit cells (see Fig. 5.7). This shows that, at the machinings, this type of defect is increased in its concentration. In some cases, such as for AG15, this peak is also present in unmachined regions but was found to appear or increase at the machinings.

In the photoluminescence, the laser machining resulted in the increase of a broad peak around 750 nm accompanied by a decrease of a PL peak around 900 nm (see Fig. 5.6a) although some samples did not have the 900 nm peak to begin with. According to Lefez et al. [88] Cu_3O_2 has shown PL around 760-780 nm. This is red-shifted to 750 nm but is spectrally closer than other defect-related PL known in Cu_2O - the closest of which are 810 nm and 720 nm for singly and doubly charged oxygen vacancies respectively (V_O^{1+}, V_O^{2+}) [42].

It should be noted that both V_{Cu}^{split} and Cu_3O_2 are actually two conceptions of the same physical effect since Cu_3O_2 can be seen as a 'defect structure of Cu_2O' [89]. The presence of one copper vacancy per double unit cell which has two copper sites and 4 oxygen sites represents a material with composition $Cu_{(4-1)}O_2$. This supports the attribution of the 750 nm PL emission to the V_{Cu}^{split} defect.

The same analysis was also carried out for AG15-2b, 3a, 3c, and 4a-c over a slightly larger area - 26.3 × 50.4 µm, this was 5 depths at 8.7 µm intervals (see

Fig. 5.6). This shows the same trends as for AF00 in Fig 5.5. Additionally, for AG15, a decrease in luminescence at 910 nm, which is a PL associated with copper vacancies (V_{Cu}), was found [42]. This could be the result of pre-existing copper vacancies being converted to the split configuration as a result of laser machining.

Thus far, the FSC^3 analysis has used two components - which were found to represent the unmachined and machined parts of the sample. However, more components can be used. Often, the additional components result in the splitting of certain features between different components artificially representing a non-physical effect. The analysis works by using the same number of components as there are materials with different spectra, this is the result of using more components than necessary. An example of this is shown in Fig. 5.8 where machining spectra 1 and 2 show sharp, non-Lorentzian peaks as part of their PL that are equal and opposite and therefore cancel each other out when combined suggesting that 4 components is more than is required to reveal physical effects in this case.

5.3 Laser machining spatial structure

The spatial structure of the machining was investigated with FIB-SEM (see Sec. 3.5). Surface FIB and SEM images of AF00-B and AF00-C respectively are shown in Fig. 5.10 with the machinings themselves shown in the light blue circles. These correspond to those shown in Fig. 4.5 where the first set has been rotated clockwise by approximately 110° and, in the second set, only the last four machinings of the bottom two rows are seen - these have also rotated by 180° between laser machining and FIB-SEM imaging.

As outlined in Sec. 4.4.1, pulse energies of about 2 and 3 µJ were used to machine the top row of the first set, and the second set respectively whilst the second row of the first set was made with pulse energies of ~ 0.9 µJ. The higher pulse energies resulted in a larger effect on the surface of the sample. Surface modifications created at sufficiently high pulse energy typically consist of a central, round depression of some 0.1-1 µm in diameter surrounded by a smooth, raised area with diameter 1-3 µm - a structure that would appear to be consistent with a localised melting and re-forming at the point of entry of the laser pulse with the central region having been melted and the surrounding area made up of a 'splatter' of this material (note that machining was carried out in a vacuum at 6.5 K). An expression for the mass of material that can be melted by a given amount of energy, E, is:

$$m = \frac{EM_r}{C_m(T_M - T)} \tag{5.2}$$

where m is the mass of the material that can be melted, M_r is the molar mass of the material, C_m is the molar heat capacity, T_M is the melting temperature, and T is the initial sample temperature at the time of machining. Using values of $E = E_p = 2$ µJ, $M_r = 143.09$ g mol^{-1}, $C_m = 70$ JK^{-1}mol^{-1} [90], $T_M = 1505$ K,

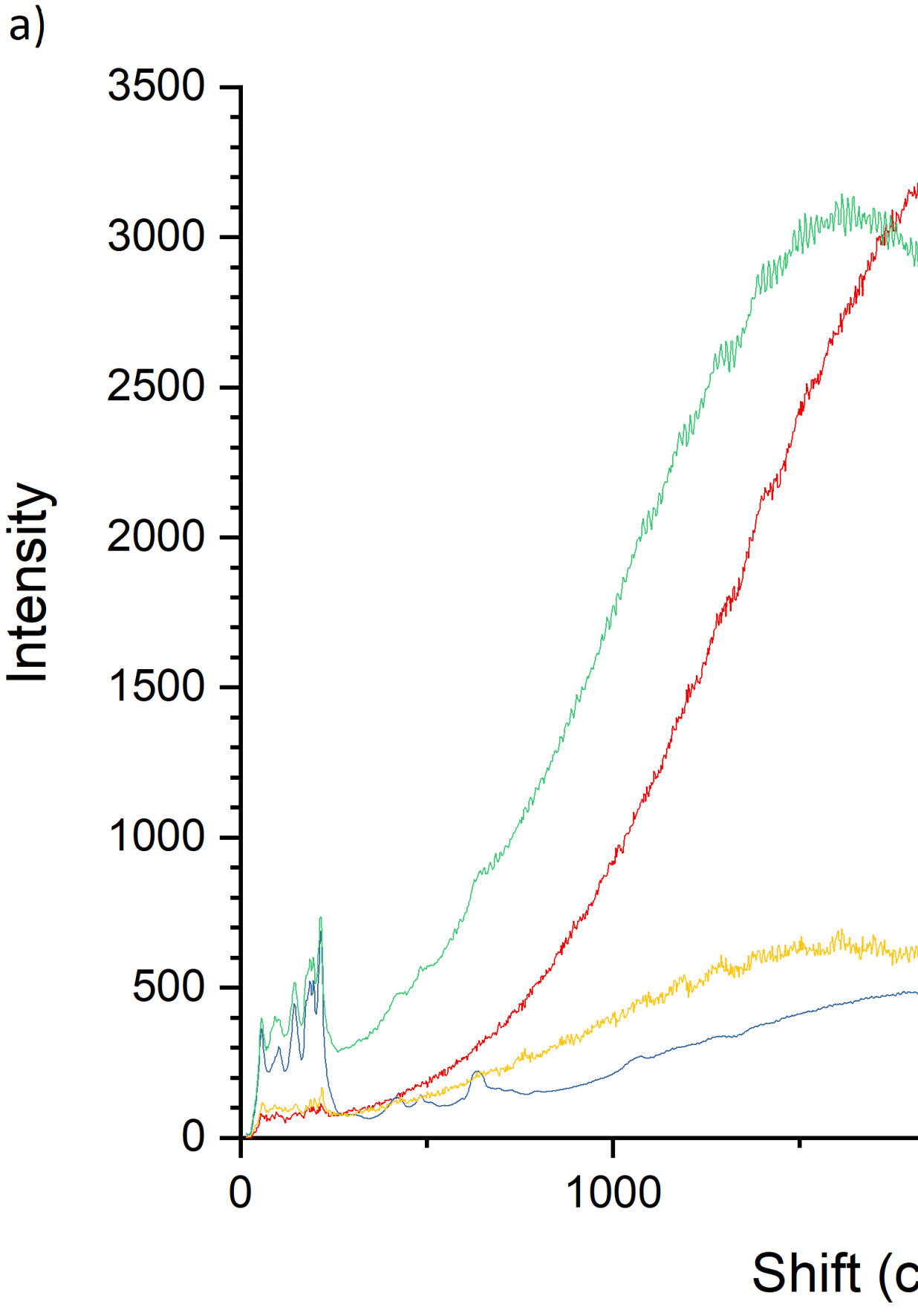

b)

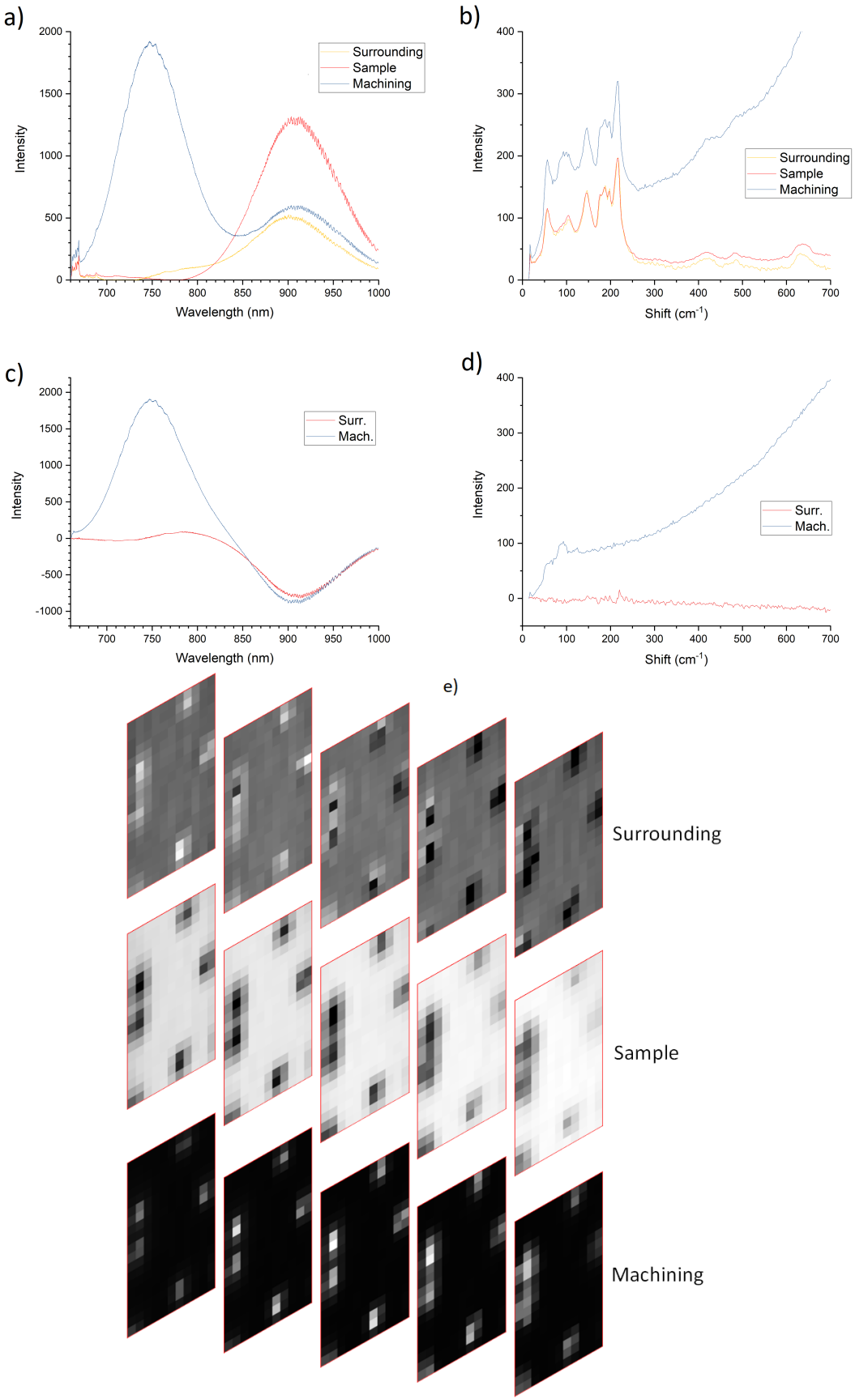

Figure 5.9: Raman spectroscopy data using 3-components in FSC_3 for the same machinings as described in Fig. 5.6.

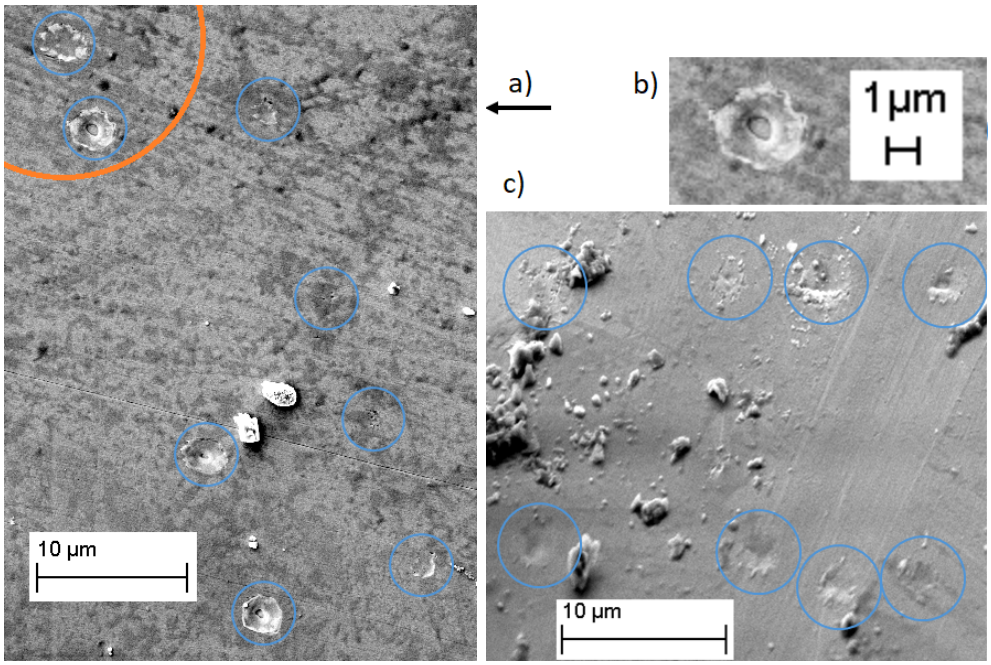

Figure 5.10: a) FIB image of site AF00/B. The size of the beam at the surface calculated with Eq. 5.3 is represented by the orange arc centred on AF00/B-1e. b) magnified image of AF00/B-1d. c) SEM image of AF00/C, only machinings 2c-f and 3c-f are seen (the sample was rotated 180 ° relative to orientation during laser machining). Light blue circles are included to show where the machining has affected the sample surface.

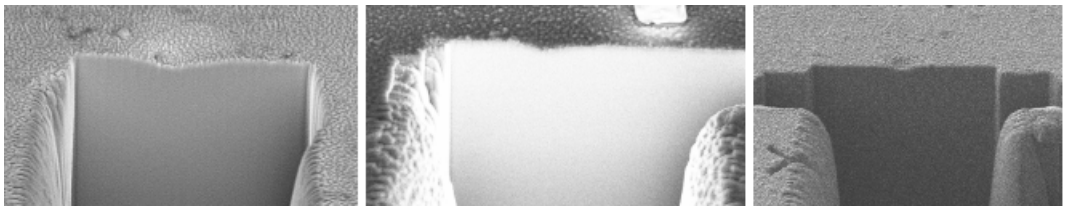

Figure 5.11: SEM images of the surface profiles of 3 machinings part way through FIB polishing. These and other images were used to estimate the amount of material displaced during laser machining. The widths of the back walls seen are 5, 8, and 10 µm for respectively.

and $T = 6.5\,\mathrm{K}$, we find $m = 2.7\,\mathrm{ng}$. While C_m depends on temperature, a constant value of $T = 600\,\mathrm{K}$ is used to provide an estimate. This value is around half of T_M and above the Debye temperature (Θ_D) for Cu_2O ($\Theta_D \sim 500\,\mathrm{K}$ [56]). Note that we also assume complete absorption of the pulse energy to get an upper limit. Given a density of $6.04\,\mathrm{g\,cm^{-3}}$, the volume of melted material would be $450\,\mu\mathrm{m}^3$. As can be seen in Fig. 5.10, the machined areas that may have undergone melting are approximately 2.5 µm across. The depressed region in the middle of these features and the raised region surround them suggest that the melting actually occurred in only the smaller interior area, but even assuming this whole area was melted up to a depth around the same scale (2.5 µm), this melted volume would only be about $12\,\mu\mathrm{m}^3$. This is far below the value calculated above and thus the laser pulses used in machining contain sufficient energy to cause this kind of melting. Note that the whole pulse is not absorbed by this area as much of the pulse is involved in further machining below the surface of the sample, and much of it may also simply pass through the sample entirely.

Fig. 5.11 shows three SEM images of laser machining on the surface of samples when FIB polishing has milled away part of the machining. It is clear in these cases that some material on the surface has been displaced due to laser machining. This cross-sectional view of the machinings, alongside a further 15 images of the same machinings taken between polishes, were used to calculate the amount of displaced material. The images were first rotated so that the top ridge seen was horizontal. Then, the contrast of the images was adjusted so that the ridge was sharply delineated by black and white only. These were then loaded into CCDPlot software where they were fully binned vertically and scaled to create plots of the ridge heights. The background was subtracted from these and the depressed region integrated to find the 2D area that had been displaced. Three of these stages are shown in Fig. 5.12 including the spatial plot. Assuming a conical-like depression in the surface of the sample, this could be used to estimate the total volume displaced. The measured volume would differ for each polish depending on how close to the centre of the depression it got with a maximum value reached at the very centre. For this reason, values of the displaced volume are given as both an average from all images of a given machining (V_{avg}), and also as the maximum value calculated from the set of images of a given machining (V_{max}). For the three

Machining	V_{avg} (µm^3)	V_{max} (µm^3)
AF00/B-1a	0.0655	0.0740
AF00/B-1b	0.0457	0.0620
AF00/B-1c	0.0367	0.0560

Table 5.2: Calculated volumes of displaced material on the surface of AF00 due to laser machining.

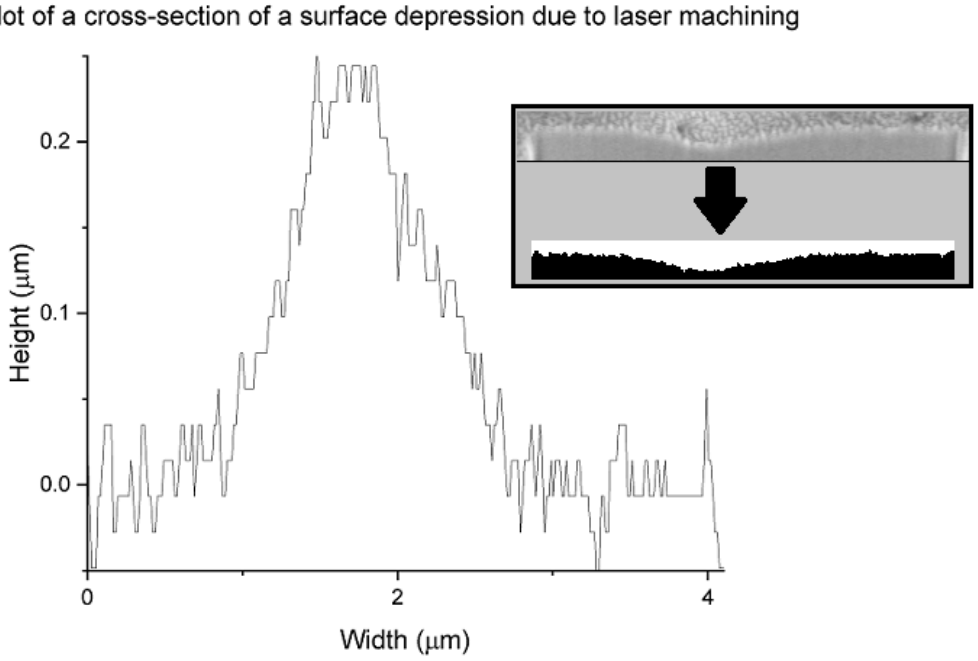

Figure 5.12: A plot of the profile of laser machining on the surface of the sample for AF00/B-1a. This was obtained from the SEM image by using high contrast to sharply delineate the top ridge (images shown in top right) then vertically binned the image to get the plot.

machinings in Fig. 5.11, these values are given in Table 5.2. The upper limit estimate included previously was assumed the size of these volumes to be much larger than they really were. In reality, the region visibly affected was not as large as the region that material was actually displaced from. Additionally, the depth of this displaced volume was about 10 times smaller than was assumed and the shape of the displaced volume was more conical than cylindrical. This confirms that the laser pulses contained more than enough energy to melt this volume.

The question that remains is why the affected area is so small. Given that the NA of the aspheric lens used to focus the beam during laser machining was 0.56, and assuming a circular beam, the radius, r, of the area of the surface that would have been irradiated by the laser beam if the sample was focused on the middle of the sample is given by:

$$r = 0.56\, d/n \tag{5.3}$$

where d is the depth within the sample were the laser was focused (in this case, half its thickness), and n is the refractive index. For AF00, this means that $r = 8.3\,\mu m$ - far larger than the features evident in Fig. 5.10. It is not clear what the reason is for this discrepancy in sizes. It may simply be the case that only the centre of the laser beam is powerful enough to be absorbed by the sample at such a beam radius, although the separation between the surface and in-sample machining in Fig. 5.16 shows that no machining occurred after the surface until the beam further reduced in radius meaning that there must be some additional mechanism that allows the laser to be absorbed at the surface of the sample that is not present below the surface. Another explanation could be that the laser machining proceeds in a somewhat similar manner to that described by Kononenko et al. [33] where laser machining begins at the focus and grows backward towards the laser source, although the nature of this machining is quite different in that it uses multiple femtosecond pulses in diamond. They did consider picosecond pulses but stated the 'diameter of the modified region substantially changes over a single shot' and that the growth rate was only 10 µm per shot. In addition, the nature of the damage caused by this machining was drastically different to that seen in this project; none of this agrees with findings in this project.

The subsurface effects of the laser machining have been investigated using FIB-SEM as described in Sec. 3.5. An example of a subsurface effect is shown in Fig. 5.13 which contains a sequence of SEM images acquired between uses of a FIB to remove 100 nm-thick layers of material in sequential steps. The visible features appear to be indicative of filamentation within the sample. There is one dominant filament, but others seem to form with increasing depth which is expected at high powers [67]. In addition, slightly further from this central filament there are non-parallel effects that don't continue through the sample. Effects of this nature are also shown in Fig. 5.14 where no filamentation was seen alongside it. This may be indicative of the laser beam interacting with defects, voids, or other inclusions already present within the sample resulting in machining at an orientation at least partly dependent on that of the pre-existing inclusions which is why they are not parallel to the filaments when they do appear alongside them.

The 4th panel in Fig. 5.13 is shown again in Fig. 5.15 alongside two plots of the widths of the laser machinings against their depth in the sample. Both are 50-70 nm wide. This type of analysis was performed for many images of machinings and the widths given above are representative, the only exception found in the data is shown in Fig. 5.16 (similar figures are shown for other machinings in Appendix D). Of all the filament-like machinings analysed in this way, this one was far closer to the surface than the others. In addition, the pulse energy used to create this machining ($\sim 0.9\,\mu J$) was lower than for all other instances were sub-surface effects were seen suggesting that greater pulse energies result in thicker sub-surface machinings.

In addition to being thinner, the machining in Fig. 5.16 also has a well-defined start point which is thicker than elsewhere. Roughly 0.5 µm deeper there is another spot-like feature that is about the same thickness. Similar

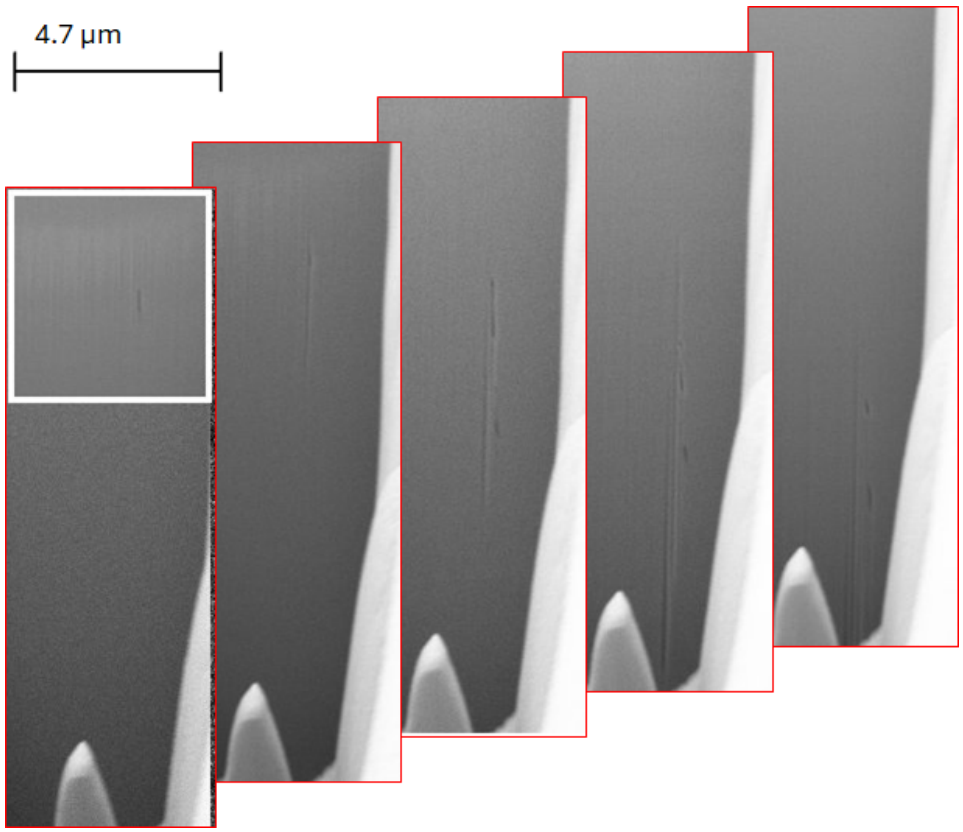

Figure 5.13: A stack of SEM images of machining AF00/C-3e taken between 100 nm FIB polishes showing the effect of laser machining below the surface of the sample. Each image is 4.7 µm wide and the depth of the front image is approximately 31 µm. The white frame in the first panel is an artefact of the software.

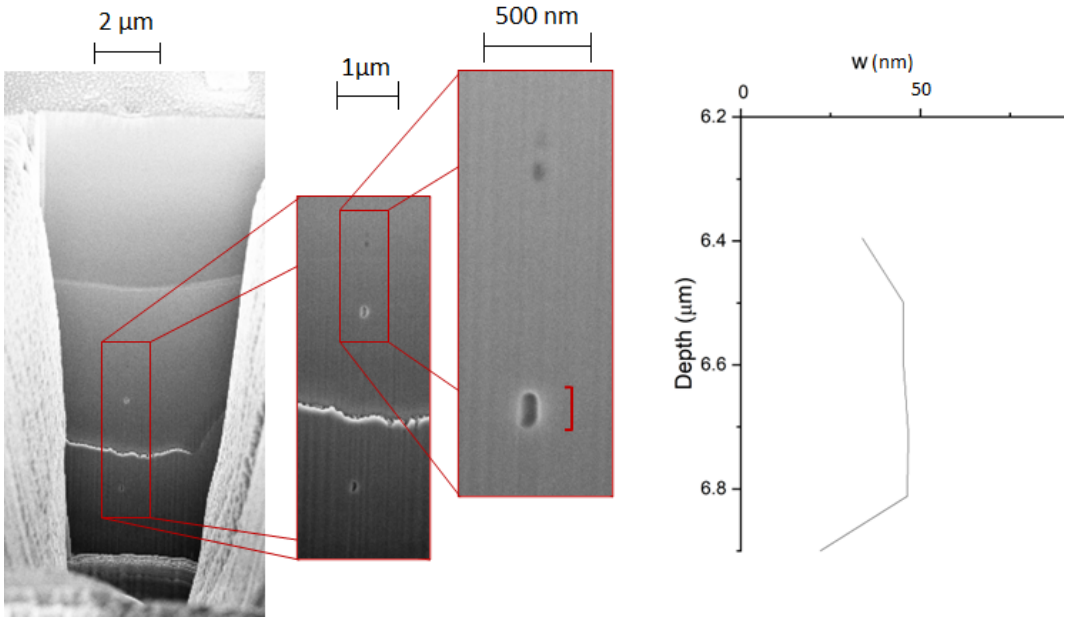

Figure 5.14: An instance in which laser machining resulted in effects without filamentation is shown here for AF00/B-1b. The width of the main feature here (shown by the red bracket) is also plotted against the depth.

spots are seen in Fig. 5.14 without a filament-like machining which could suggest their origin being an interaction between the laser and inclusions already present in the crystal. It is difficult to say whether the same can be said for the beginning of the machining in Fig. 5.16. Whilst it is a similar width, which may suggest that it was an inclusion which then triggered the subsequent damage, laser filamentation does not require such inclusions to trigger it and it is known that the two photon absorption mechanism only begins at a certain threshold. Therefore, a distinct beginning to a laser machining is expected over a gradual one suggesting that this is what is seen in Fig. 5.16. Furthermore, the spots in Fig. 5.14 did not result in filament-like machining.

5.4 Laser pulse energy dependence

Plots showing both the absorption cross section (σ_{A}) and transmission change cross section (σ_{TC}) as described in Sec. 3.3 are shown in Fig. 5.17. As would be expected, the plots show that, generally speaking, higher pulse energies result in a larger change in transmission. σ_{TC} (calculated using Eq. 3.6) was considerably larger than σ_{A} (as shown in Fig. 5.17a). σ_{A} is almost always positive and shows the same trend as for σ_{TC}. The overall effect is a decrease in transmission by absorption and scattering beyond the collection directions of the 0.56 NA optics. But the absolute change transmission was dominated by changes which consisted of both increases and decreases in transmission in the area surrounding the machining due to variations in the refractive index brought about by strain and interference effects. Fig. 5.17a indicates that the

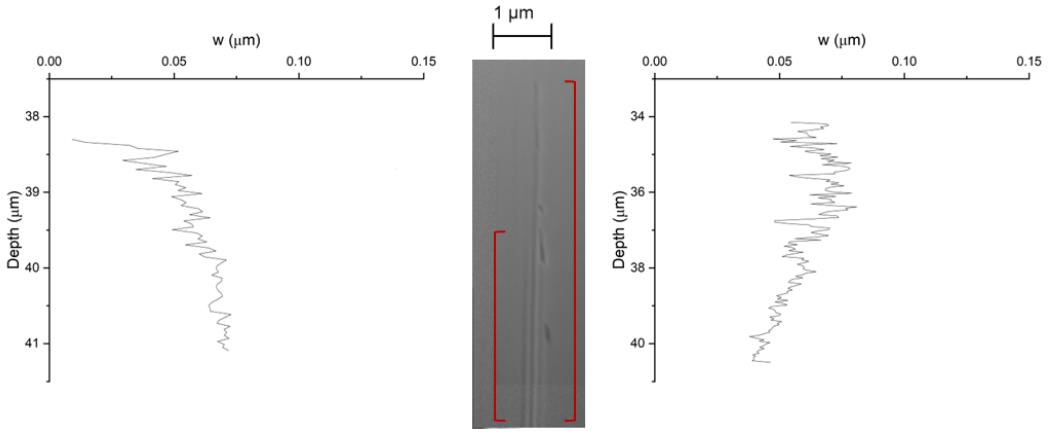

Figure 5.15: An SEM image of laser machining AF00/C-3e with plots of the filament thicknesses shown either side. Red brackets on the SEM image show the depth ranges of each of the plots.

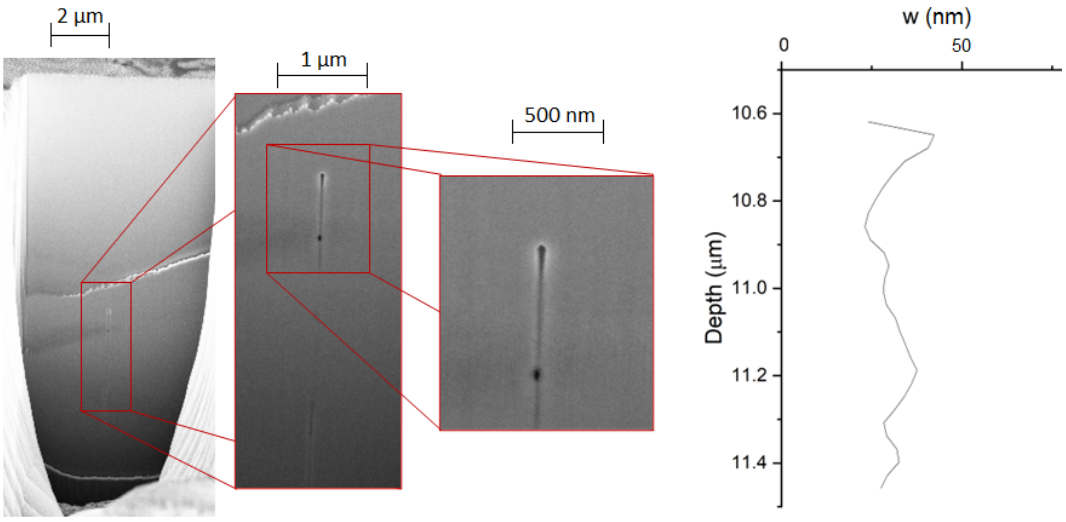

Figure 5.16: An SEM image of laser machining AF00/B-2d which is relatively close to the surface of the sample. There also appears to be a very distinct beginning to the sub-surface effects.

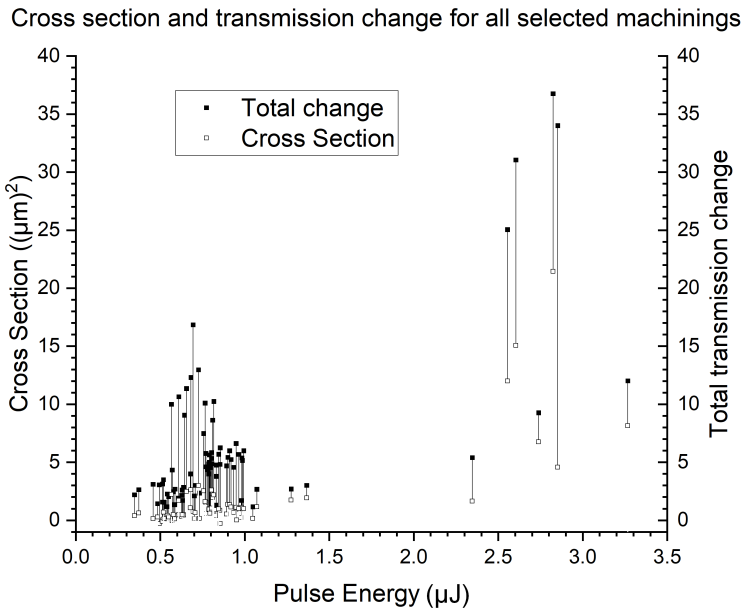

(a)

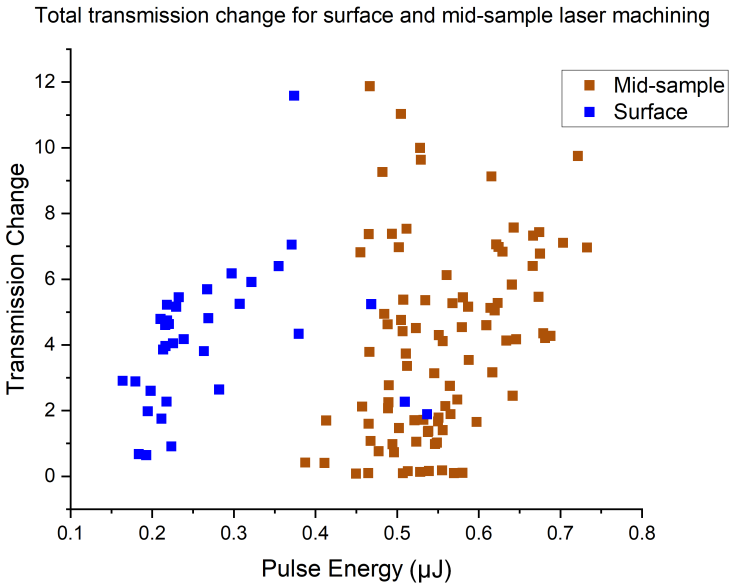

(b)

Figure 5.17: (a) Measured changes in σ_A and σ_{TC} for laser machinings in sample AL01. (b) A plot of calculated transmission change due to the machinings on AM01 as a function of the pulse energy used. All machinings affected at least one of the surfaces, but the laser focus was positioned at the front surface (data points shown in blue) or at the centre of the sample (data points shown in orange).

threshold pulse energy when focused on the middle of the sample AL01 was around 0.4 µJ.

The data for AM01 shows two separate threshold pulse energies. This is because some machinings were performed with the laser focused in the middle of the sample as normal, but for others the laser was focused on the surface. Fig. 5.17b shows data for surface-focused machinings (blue), and mid-sample-focused machinings (orange). For mid-sample machining, a threshold pulse energy around 0.4 µJ is found, similar to AL01. When focused on the surface of the sample, this dropped to around 0.15 µJ. It should be restated here that all machining in both of these samples affected the surface and very few appeared to affect the middle of the sample. It is therefore to be expected that focusing the laser on the sample surface would reduce the pulse energy required for machining since this greatly increases the intensity at the machining location.

Machinings with features rendering the analysis of the cross-sections unreliable (as detailed in Appendix D) have been excluded from Fig. 5.17. Approximately 38% of machinings were plotted for AL01 and 82% for AM01. One factor that altered the outcome was machinings that were performed very close together such as in the distance variant set of the AL01 sample. To show this graphically, a line of best fit was plotted on the σ_A versus pulse energy graph for this set of machinings and the vertical distance of each point to the line was calculated. This distance was then plotted against the distance to the closest neighbour of each machining, shown in Fig. 5.18. We clearly see that the machinings only deviate from this trend when they are closer together than about 2 µm. It is believed that the increased absorption of a machining means that the usual threshold power does not need to be met in order for further machining to occur. This means that for a machining performed close to an existing one, machining may occur as normal, but a weaker part of the beam that overlaps with a previous, presumably absorbing machining gets absorbed and results in further damage at the existing machining location and thus a greater change in transmission is measured than normal. This is supported by the images in Fig. 5.18 which were created using the pulse videos which show the change in transmission. For most machinings the effect is consistent as shown in the first two images, but for the instances where machinings were too close to each other, there is machining that does not fit this pattern. More specifically, there is more machining at the location of the previous machining as well as the new one.

Analysis of the structure of the damage caused by laser machining in Sec. 5.3 showed certain other effects of varying pulse energies. The largest pulse energies had the greatest effects on the surface of the sample - this was for energies of 2 µJ and above. These are thought to be due to the sample melting and reforming and so it is no surprise that a laser pulse containing more energy would increase the amount of melted material. For machining below the surface, there was one instance where the resulting filament-like damage was narrower than for other cases. This was for the only machining below 1 µJ where subsurface effects were seen. As with the surface machining, this suggests that a greater pulse energy causes a thicker machining.

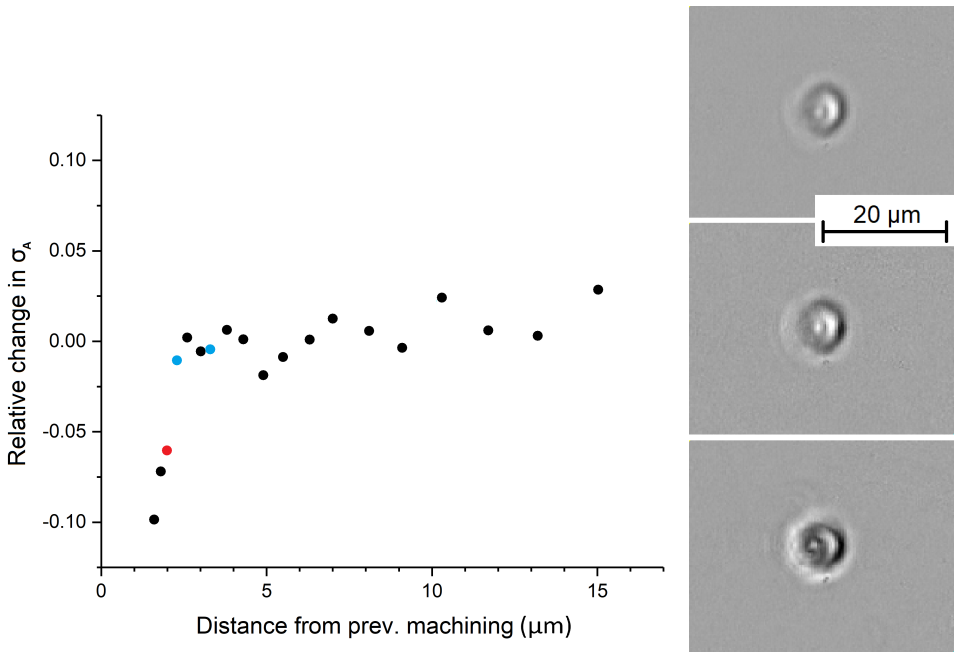

Figure 5.18: The relative change in σ_{A} (by measuring the deviation of points from a line of best fit) due to laser machining in the vicinity of previous machinings (left). The images (right) show the change in transmission intensity from before laser machining to after (scaled from $-4500 \rightarrow 2500$ counts). The first two images show examples of spatially independent machinings (indicated by blue points on the plot), and the final image shows one affected by the presence of a previous machining in its vicinity (indicated by a the red point on the plot).

Chapter 6

Control of excitons by laser machining

This chapter contains the findings from the absorption microspectroscopy (setup described in Sec. 4.2 and analysis in Sec. 3.2) which reveal the effects of laser machining on the optical properties of the excitons. Both the yellow exciton series (n=3 to 6) and the 1s-orthoelectron were analysed using this method. Errors calculated for each of the fit parameters for all machining sites can be found in Appendix B.

6.1 Yellow Rydberg series

The main results considered in this section are taken from the sample AF00. This was the only sample that was thin enough for there to be sufficient transmission at the wavelengths around the yellow Rydberg series of excitons (spectrum shown in Fig. 6.1), whilst also being thick enough to enable laser machining in the middle of the sample, not just on the surfaces. The results come in the form of greyscale maps over a machined region of the sample where the black-white value relates to one of the fit parameters of one of the peaks in the aforementioned Rydberg series. An example of one of these fits for the $n = 5$ peak is shown in Fig. 6.2; this is for the site A on AF00. As outlined in Sec. 3.2, these parameters are: offset (O), peak energy (ν_0), FWHM (Γ), amplitude (A), and differential amplitude (δ_L).

Fig. 6.3 shows the maps resulting from this analysis of site AF00/A for excitons of n=3 to 6. The maps show that the effect of laser machining was similar for the different n. This is especially true for the ν_0 plots where shifting in the peak energies appears to be constant. δ_L varied the most between the different absorption peaks both in its initial value, and how the value changed due to machining. Without any machining, for the $n = 3$ peak, δ_L was -0.49 which decreased in magnitude with n and it was just -0.28 for the $n = 6$ peak. Both increases and decreases in this value were seen due to laser machining thereby increasing the range of values of δ_L in the region of the sample surrounding each machining. This range, R, was dependent on the n following the dependence $R = 2^{n-1}/100$.

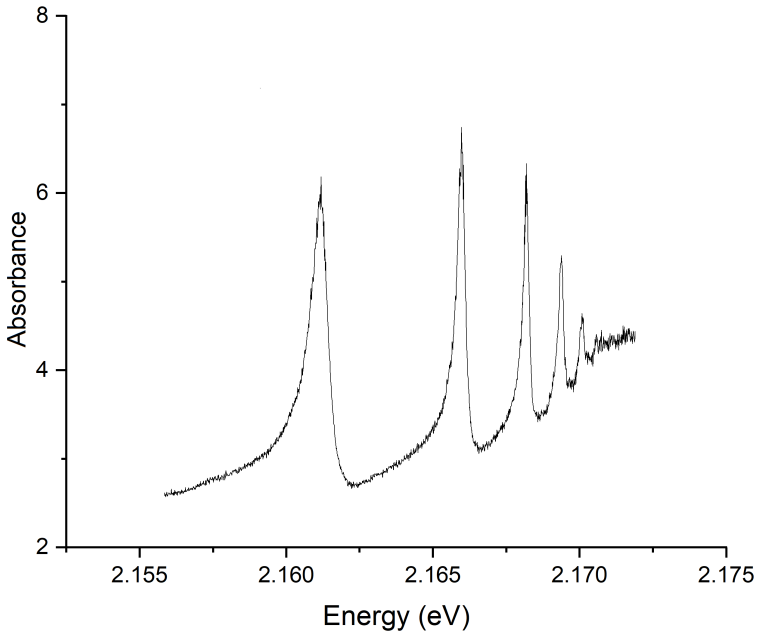

Figure 6.1: An example spectrum of the yellow Rydberg series for AF00 from the $n = 3$ peak upwards.

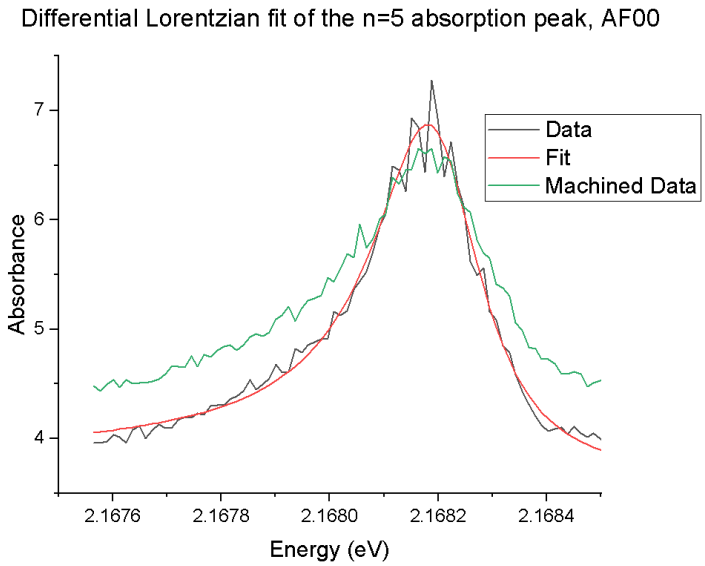

Figure 6.2: An example of a fit (red line) to the measured absorbance (black line) calculated using Eq. 3.4 close to the $n = 5$ exciton, using a differential Lorentzian curve (see Eq. 3.6) with the parameters: $O = 3.80, \nu_0 = 2.168201\,\text{eV}$, $\Gamma = 0.24\,\text{meV}$, $A = 6.38$, and $\delta_L = -0.65$. An example of an absorption peak at a machined part of the same site (AF00/3f) is also shown.

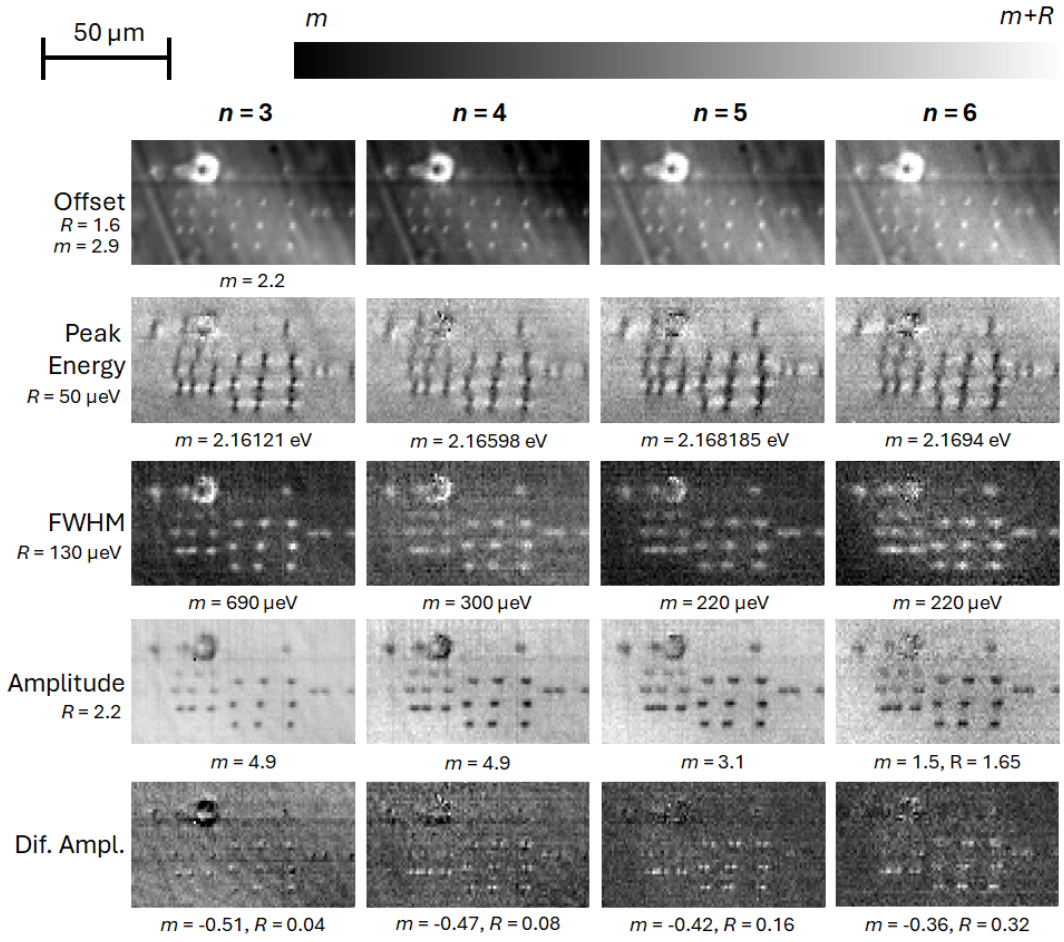

Figure 6.3: Maps, across site AF00/A, of the five curve fit parameters for the absorption peaks of the excitons with quantum numbers n =3,4,5. Black and white in these maps correspond to a minimum (m) and maximum ($m + R$), R being the range. For ease of comparison, the scales are kept for different n where suitable. Values of m or R deviating from the defaults given on the left are shown below each map.

6.1.1 Peak centre maps

Fig. 6.4 contains the maps of peak centres for the three machining sites for spectral imaging in the plane of the middle of the sample. For the three sites shown, different peaks were fitted depending on which peak showed the clearest effect on the parameters. These were the peaks associated with exciton $n = 3$ for sites A, B, and C respectively. In the maps of the 5 parameters, the ν_0 map shows the largest effects spatially and they are the most clearly anisotropic with both positive and negative shifts in its value. Much like with the patterns seen in the qDIC images in Figs. 5.2 and 5.3, there are 'light' and 'dark' axes perpendicular to the polarization direction of the laser during machining along which an increase or decrease in ν_0 are seen respectively. Furthermore, these patterns are only seen for machinings in the middle of the sample, not merely on the surface just as with DIC. Unlike qDIC, however, there appears to be a link to laser polarization. In the images of sites A and B in Fig. 6.4, the increase in ν_0 is extended in the horizontal. All laser machining at these two sites was performed with a vertically polarized laser. On the other hand, machinings AF00/C-1a-f and AF00/C-2a-d all used horizontally polarized lasers whilst the rest used vertical polarization (see Fig. 4.5). For the instances in which a horizontally polarized laser pulse was used, there is a decrease in ν_0 for horizontal displacements relative to the machining. Furthermore, machinings AF00/C-3c,d show an increased ν_0 between them (having been machined using vertically polarized lasers). An alternative explanation for the patterns' orientation was mentioned in Ch. 5 which is that orientation is determined by the orientation of one of the crystallographic axes.

Results from qDIC analysis (see Sec. 5.1) do not show any change in the pattern seen due to laser polarization, but the similar pattern for mid-sample laser machining and the fact that both a ν_0 shift and birefringence can be explained by a strain field suggest that these two things may indeed be connected. It should also be noted that, despite not being due to laser polarization, changes in the orientation of the anisotropic birefringence patterns were seen in qDIC images but such changes were related to the depth of the machining. In the case of the ν_0 map of site C in Fig. 6.4, the machinings 2c-f and 3c-f included effects on the front surface of the sample while the others all affected the back suggesting the there could also be a difference in depth at play here providing an alternative cause for the changing pattern between different machinings (although this cause itself is not well understood). Fig. 6.4 also shows qDIC analysis of the same site of machinings performed early in this project. Note that there is a phase difference between the machinings on the top row which is aligned with that seen in the peak centre map. It is known from further qDIC analysis that the shear direction has to be aligned with this pattern in order for it to be seen properly which could explain why it is so weak in this case. Further qDIC including sample rotation has unfortunately not yet been possible as the sample AF00 was badly damaged during FIB-SEM analysis.

A further comparison to draw between the findings of the peak centre maps and qDIC images is the area over which there is an effect. For other maps in this chapter (e.g. offset, see Fig. 6.4) the affected area is quite small and distinct

from other machinings, whereas the ν_0 maps see the pattern extend between the machinings - a distance of up to 15 µm. Again, this similarity supports the idea that the patterns seen in both qDIC images and ν_0 plots are a result of the uniaxial strain field at each machining location.

6.1.2 Other fit parameters

The offset parameter maps are also shown in Fig. 6.4. The most distinguishing feature of these maps is the small size of the area over which O was affected compared to the other maps. Both the largest and smallest seen are in site B which shows features on the top row measuring roughly 3 µm across and features on the bottom row only 1.5 µm across. Whilst the top row was created with higher pulse energies than the bottom, the pulses were still weaker than those used to create the array of machinings seen in the first image so this alone does not explain their increased size. The main difference between the larger effects and the other machining effects was that they also had a significant effect on the surface (see SEM images in Fig. 5.10). These surface effects are the same size as the effect seen on the O maps suggesting that the larger spots are out-of-plane effects from the surface. This could be an increased absorption, but could also be due to incident light at these surface effects being diffracted from their normal path since the surface features are not flat. As for the rest of the small effects, including those in the first image where there was not visible surface machining, they are compatible with findings from qDIC and FIB-SEM in that the machinings appear to consist of a small, highly absorbing central damage which results in a strain field surrounding it which has further effects on properties such as the band gap.

The maps of Γ and A are also shown in Fig. 6.4. In both cases the area over which the parameter was affected by laser machining is larger than for O - roughly 3 µm. For Γ, the effect is an increase due to laser machining, whilst for A a decrease is observed. Transmission imaging up to this point has all shown an increased absorption due to laser machining so it may seem odd at first that A should be seen to decrease. However, most of that additional absorption is accounted for by O which represents a background absorption across a broader range of wavelengths. This could also go some way to explain the decrease in A too. A broad absorption occurrs instead of the specific exciton absorption but, in the first and third images specifically, the sizes of the affected areas are not the same for both O and A and thus the change in O alone is not sufficient to explain the change in A. As mentioned above, however, the areas are similar to those in the Γ map. This suggests that the exciton resonances surrounding the laser machining are being shifted due to strain such that material that would previously have absorbed at the unshifted exciton energy - which would have contributed to the amplitude of the absorption peak - is absorbing at slightly different energies resulting in both a broadening and shortening of the absorption peak. If this were the only factor involved, the total oscillator strength of each peak would be unchanged. This was often found to be the case, but not invariably (see Appendix F). For some sites, particularly for peaks

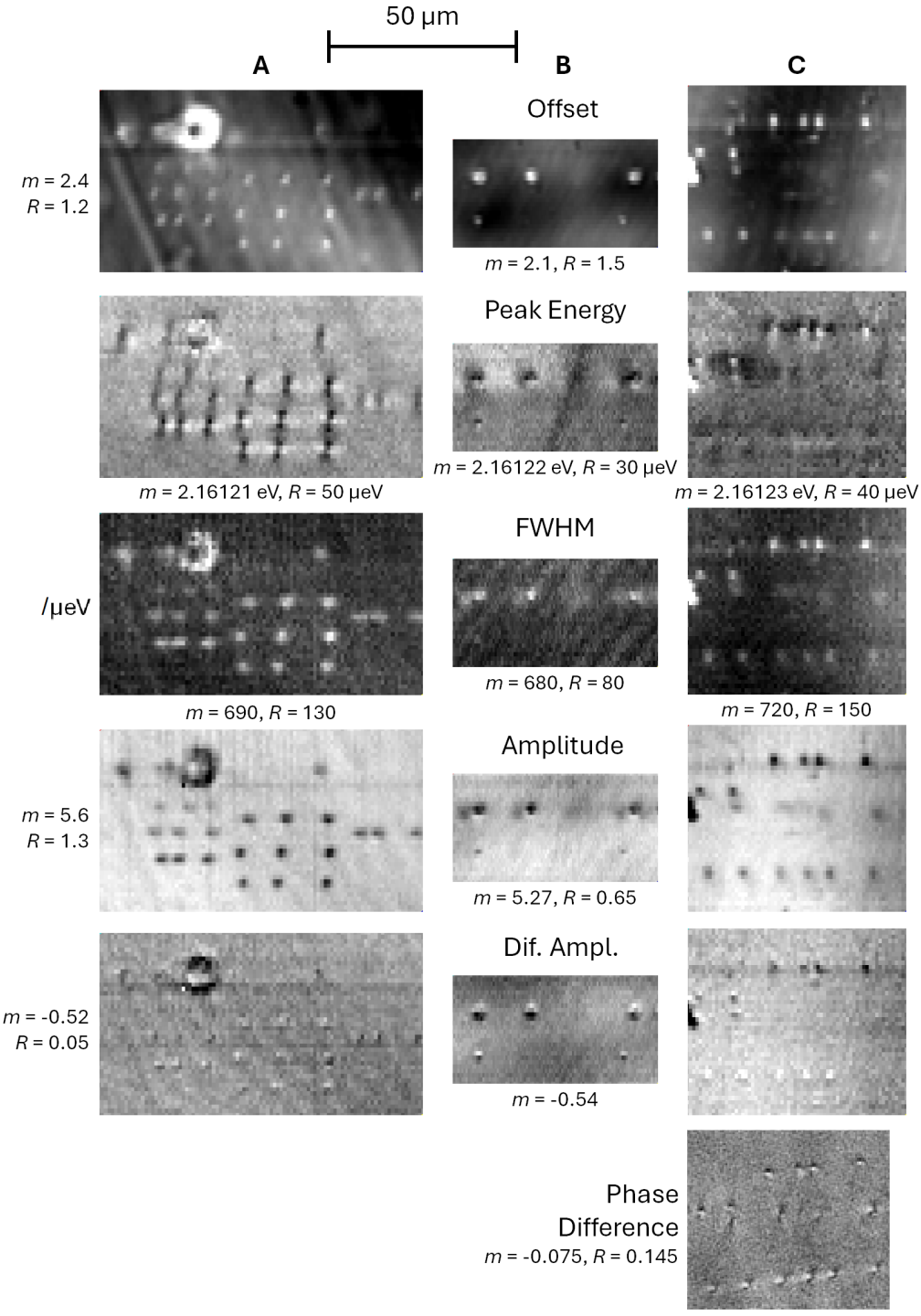

Figure 6.4: Maps of the differential Lorentzian fit parameters for machining sites AF00/A,B,C for the $n = 3$ exciton peak. Greyscale ranges are given as in Fig. 6.3. A phase difference image is also included from qDIC analysis of site C.

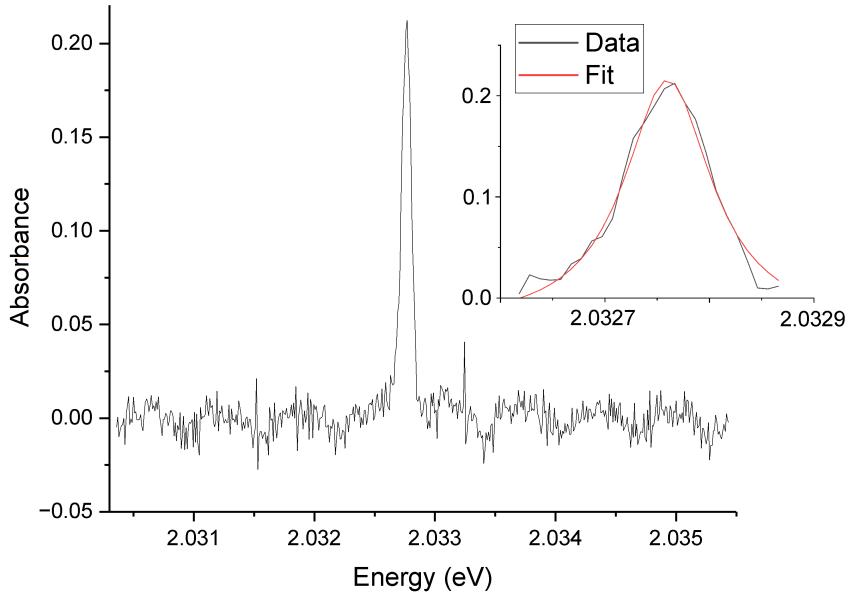

Figure 6.5: An example of an absorption peak for the 1s-orthoexciton (after a background subtraction) for AG15. The Lorentzian curve used to fit this is shown in the inset along with the data that was fitted.

with $n > 3$, the oscillator strength would be unchanged, but for others, laser machining resulted in a decrease in oscillator strength suggesting an additional factor affecting the amplitude (such as background absorption as mentioned above).

δ_L was discussed briefly above due to its strong dependence on which absorption peak was fitted. As can be seen in the maps in Fig. 6.4, it is also the only other fit parameter where there was consistently both a positive and negative change in value due to laser machining and often displayed anisotropic patterns. Despite the above similarities, both the shape and the clarity of the laser machinings in these maps was not consistent across the three machining locations with the second site showing a top-bottom positive-negative asymmetry, and the effects being weak, but also showing opposing effects for different machinings on the final site. In most cases, the overall effect on δ_L was to decrease its magnitude which is compatible with the Γ findings - a peak which broadens tends to become more symmetrical.

6.2 1s-orthoexciton

In order to investigate the effect of machinings on excitons in thicker samples, they were measured at a transparent wavelength range of the s-orthoexciton around 608.5 nm. This would result in a single absorption peak which could be fitted as before, only with a symmetric Lorentzian peak (i.e. without the δ_L parameter). As mentioned in Sec. 3.2, fitting this peak was more difficult than the Rydberg peaks due to the absorption peak splitting into its three states due to the linewidth being smaller than the energy shifts for the 1s exciton.

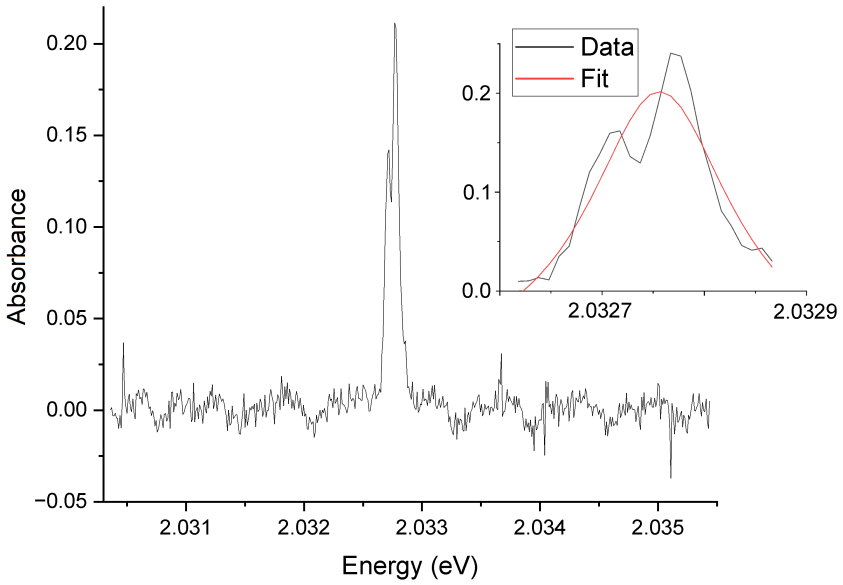

Figure 6.6: As in Fig. 6.5 but for where peak splitting has occurred.

Examples of these fits for AG15 are shown in Figs. 6.5 and 6.6 for instances of an accurate fit, and a fit where peak splitting has occurred. Fig. 6.7 includes examples of some of the clearest maps resulting from these fits, but even these are often unclear and show regions of very sharply delineated properties where the fit would flip between considering all the peaks as one degenerate state, or just one or two of them independently of the other/s (see the left side of the AG15 ν_0 map and the right side of the second AF00 maps for both ν_0 and Γ.) The first column in Fig. 6.7 is the AF00/B site described in Sec. 3.1.1 also shown in Fig. 6.4 though it has been flipped in the y-direction. The middle column shows the AG15 site described in the same chapter with qDIC and Raman in Ch. 5. The final column contains maps for the row of high pulse energy test-machinings in AF00. These were much larger and were performed over a larger area so a different scale bar is used here compared to the other two.

The effects seen are largely comparable to the fits from the Rydberg series of excitons. O increases due to laser machining, albeit only by a small amount. Similarly, A decreases significantly. The slightly larger area over which A is affected is evident only in the first column. This is also the case with Γ which, as with the previous fits, increases due to laser machining. Finally, ν_0 appears predominantly to decrease due to laser machining, but the maps of AF00 also show a slight increase too. In the first set, the pattern formed is not clear, but in the high pulse energy machinings, the same pattern seen in Fig. 6.4 is evident though they appear to be at an oblique angle to the laser polarization. This shows that both the 1s-orthoexciton and the yellow rydberg excitons appear to undergo comparable energy shifts due to the strain field formed from laser machining, although this effect is far clearer for the p-exciton series fits. This is likely due to the lifting of the degeneracy being less obvious for these excitons where the spectral linewidth of the states was greater than the energy shift in

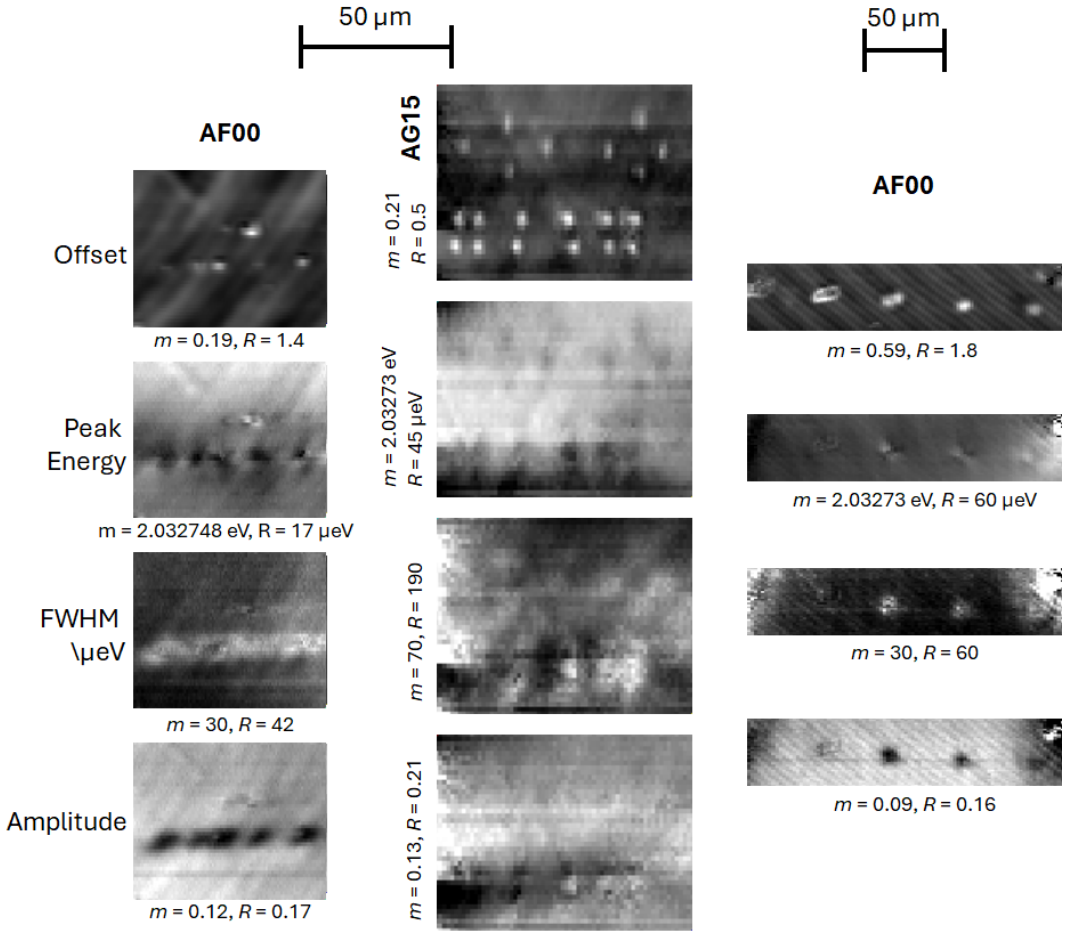

Figure 6.7: Maps for the parameter fits of the 1s-orthoexciton peak: O, ν_0, Γ, and A for laser machining sites AF00/B, AG15, and AF00/X. The first scale bar applies to the first two sites and the second only to the final site. The greyscale values m and R are used in the same way as Fig. 6.3.

the state splitting. The main difference between these maps and their Rydberg counterparts is that shifts in the parameter values occur in between machinings for both Γ and A, not just for ν_0 as seen previously (see the bottom two rows of machinings in AG15 in Fig. 6.7). For A specifically, there are bright regions between the two rows showing an increase in absorption in an area that was not machined, but would most likely be strained compared to the rest of the sample. Alternatively, this could represent increased peak splitting as the peaks shift in energy compared to one another (see fit in Fig. 6.6).

Chapter 7

Conclusion

The aim of this project was to confirm two-photon laser machining in Cu_2O and to determine the effects that such machining has on the crystal's optical properties, particularly those of its Rydberg excitons such that their local confinement might be achieved. Such analysis included: absorption microspectroscopy, focusing on excitonic properties; transmission imaging; Raman spectroscopy, to investigate structural and chemical changes; focused ion beam - scanning electron microscopy (FIB-SEM), to produce high magnification images of the machinings both on and below the sample surface; and quantitative differential interference contrast (qDIC), which is used to show birefringence in a sample. All of these techniques were valuable in showing certain effects of laser machining.

Before any of these analysis techniques were employed, laser machining in Cu_2O first had to be shown to be feasible. Such machining was governed by a nonlinear, two-photon absorption mechanism in which single 30 ps pulses of a 1064 nm laser with photon-energies below the bandgap of Cu_2O was used. The machining was performed at cryogenic temperatures and analysed in situ. The lower pulse energy meant that the crystal was transparent for light at this wavelength, but at very high intensities, two photons could be absorbed simultaneously by electrons in the valence band which had enough energy to overcome the bandgap when combined. The electrons liberated in this process could then become involved in a linear absorption which dominates the absorbed energy leading to subsequent local damage/modification. This type of laser machining is fairly common for other semiconductors [36] [37] [33] [34], but was carried out for the first time on Cu_2O in this project. Such machining was successful, although repeatability of machining exclusively within the sample was challenging. This was not entirely unexpected as the threshold power for picosecond laser machining is known to fluctuate much more than that of femtosecond laser machining [33] and picosecond machining is also more susceptible to defects [62]. Other fluctuations (such as laser focal depth and machining success/failure) in this project were attributed to inhomogeneous defect concentrations on the surfaces of the crystal where it was found that surface absorption occurred much more readily than for the middle of the sample.

Absorption microspectroscopy was then performed in situ on the sites of the samples where laser machining was carried out and the exciton peaks of the resulting absorption spectra were fitted as a differential Lorentzian curve added to a background absorption. This could be defined by 5 parameters: an offset value for the background, and four parameters for the peak itself - peak energy, FWHM, amplitude, and differential amplitude (an asymmetry factor). The result of machining included an increase in the offset and FWHM - or an increase in the background absorption and a broadening of the peak. There was also a decrease in the amplitude of the absorption peak. A decrease in the magnitude of the differential amplitude showed that the peaks became more symmetrical as a result of laser machining, although the opposite effect was also present at the very centre of the machinings. Both positive and negative changes were also present in fits of the peak energy where a biaxial pattern was evident with the peak energies along one axis increased, and along the other, decreased by some tens of micro-electron volts. The orientation of these patterns are thought to be related either to the laser polarization, or the crystal orientation. This effect was also evident over areas roughly 20 µm across, a much larger area than both the damaged one and also areas over which other parameters were affected suggesting a strong dependence on the crystal strain.

Transmission imaging was performed by recording videos of the sample as the machining was performed and averaging the frames before and after the pulses to get before- and after-pulse images of the sample. These were then used to calculate the absorption cross section of the machinings at visible wavelengths. This assumed that the dominant effect of machining was an increase in absorption. To confirm this, the calculations were adjusted to include any change in transmission due to laser machining, This was an integral of the absolute transmission change which showed refractive index contrast - a value referred to as the transmission change cross section (σ_{TC}). Whilst the overall effect of machining was almost always an increase in absorption, the value of σ_{TC} was considerably larger than that of the absorption cross section showing that the most significant change in transmission due to laser machining was not the increase in absorption, but phase effects from variation in the refractive index due to strain.

Raman confocal microspectroscopy was used to acquire Raman spectra over a 3D array of points surrounding a machining at room temperature and hyperspectral analysis software was then used to produce spectra related to both the un-machined and machined parts of the sample. The laser used in Raman spectroscopy can also act as a source of excitation and thus this analysis provided data on both the changes in the vibrational Raman modes of the crystal, and also its photoluminescence (PL). Changes in both the Raman and PL regime both indicated the formation of Cu_3O_2/V_{Cu}^{split}defects, both of which represent the same physical change. This was present in the area surrounding the centre of the machining.

High magnification images of the effect of laser machining both on the surface, and within a sample was accomplished using FIB-SEM. Both beams

were used to image the sample's surface, but the FIB was also used at a higher current in order to mill parts of the sample. The axis of the electron beam was at a 54° angle to the FIB so the SEM could subsequently be used to image what had been revealed of the machinings below the surface. Scans of the surface showed what appeared to be small amounts of melted and re-solidifed material. This has been shown to occur for picosecond machining in previous findings [37] and the required energy for melting such a volume of Cu_2O was shown to be far below the pulse energy of the laser used for machining. Damage below the surface took the form of long, thin structures with widths of the order of tens of nanometres consistent with damage caused by a laser filament. Laser filamentation is caused by the nonlinear, self-focusing phenomenon where a laser beam of sufficiently high power will increase the refractive index of the medium that it's travelling through resulting in the beam collapsing in on itself by refraction. Furthermore, one of the factors that arrests such a collapse is multiphoton absorption [67] which is the mechanism by which the laser is absorbed by a transparent medium (such as an infrared laser in Cu_2O). Self-focusing occurs at a critical laser power where an increase in the refractive index of an optical medium dominates over the effects of diffraction. This critical power was found to be well below the powers used in laser machining.

Cu_2O is typically an optically isotropic material, but can become birefringent when strained such as in the areas surrounding laser machining. Birefringence in a sample can be measured using qDIC transmission microscopy. To achieve this, the incident light is first split into two orthogonally polarized beams and separated by a small shear distance. They then pass through the sample where they will take on some phase shift relative to the other if the sample is birefringent. They are then recombined and the intensity of the resulting recombination due to constructive or destructive interference can be used to calculate the phase shift between the two beams. This was represented as greyscale images where the values of each pixel in the image represented the phase shift at that point in the sample. Biaxial patterns similar to those seen in the peak energy maps from the absorption peak fits in the absorption microspectroscopy analysis were evident for machinings within the sample (as opposed to surface-only machining). The pattern itself reflects a uniaxial strain field where a tensile strain along one axis results in a compressive strain in the perpendicular axes and vice versa, although it is unclear why this might be the case. It is possible that the orientation of this pattern is determined by the crystal structure, but such an explanation is not well-developed at this time.

Whilst picosecond laser machining was certainly achieved, any future attempts at this sort of two-photon absorption laser machining would likely benefit from the use of femtosecond pulses as predicted in the literature. One of the most critical factors for both laser machining in the middle of the sample and the subsequent absorption microspectroscopy was the sample thickness. The first sample that underwent laser machining, AF00, turned out to be the only sample where both of the above processes were viable. Given a similar setup to the one used in this project (see Ch. 4) further preparation of the samples should also be carried out in future to include polishing to a thick-

ness of roughly 100 µm. Conversely, laser machining could be carried out on thicker samples such as AF13 and AG15 and then polished or even FIB-milled afterwards. All analysis techniques employed after laser machining, except FIB-SEM, involved light propagating along the same axis as the machining laser, but if the sample could be made into a cubic form, the laser machinings could also be investigated from other angles in order to form a better picture of the effects with respect to depth.

In regards to exciton confinement by the creation of localized strain traps, it was indeed possible to create both local increases and decreases in exciton energy levels due to the presence of a strain field created by laser machining. However, energy-shifted regions tend to follow the shape of the filament-like damage that causes them which is larger than the few-micron scale required for the confinement of even very high-n excitons. Superposition of multiple strain fields may be a solution to this. This was investigated in some samples using the cross-like structure wherein 4 machinings might all contribute to an increased strain in the area that they enclosed, but this was never shown to be the case. However, if the energy-shifted regions are related not to the laser polarization, but to the crystal orientation, such a structure would cause the strains to cancel out in the centre. Structures consisting of two nearby machinings with superposing strain fields may therefore be preferred. Confirmation that the strain fields are aligned with the crystal axes could also be accomplished with Laue images of the samples used. In this project, the axis of laser machining was kept constant (normal to the flat surfaces of the samples), but laser pulses delivered at orthogonal angles, if their contributions to strain could be superposed, would be capable of creating localized strain traps for high-n excitons. This could even be done in the form of arrays, or in conjunction with other confinement methods. If viable, this would be a vital step towards the practical integration of Rydberg physics-based functionalities with solid state,semiconductor technologies.

Bibliography

[1] Walter H Brattain. The copper oxide rectifier. *Reviews of Modern Physics*, 23(3):203, 1951.

[2] Haibin Zhang, Shane M Eaton, and Peter R Herman. Low-loss type ii waveguide writing in fused silica with single picosecond laser pulses. *Optics Express*, 14(11):4826–4834, 2006.

[3] Changqiong Zhu and Matthew J Panzer. Etching of electrodeposited cu 2 o films using ammonia solution for photovoltaic applications. *Physical Chemistry Chemical Physics*, 18(9):6722–6728, 2016.

[4] Richard N Briskman. A study of electrodeposited cuprous oxide photovoltaic cells. *Solar Energy Materials and Solar Cells*, 27(4):361–368, 1992.

[5] BP Rai. Cu2o solar cells: a review. *Solar cells*, 25(3):265–272, 1988.

[6] Xiaolong Deng, Qiang Zhang, E Zhou, Changjian Ji, Jinzhao Huang, Minghui Shao, Meng Ding, and Xijin Xu. Morphology transformation of cu2o sub-microstructures by sn doping for enhanced photocatalytic properties. *Journal of Alloys and Compounds*, 649:1124–1129, 2015.

[7] Wenzhe Niu, Thomas Moehl, Pardis Adams, Xi Zhang, Robin Lefèvre, Aluizio M Cruz, Peng Zeng, Karsten Kunze, Wooseok Yang, and S David Tilley. Crystal orientation-dependent etching and trapping in thermally-oxidised cu 2 o photocathodes for water splitting. *Energy & Environmental Science*, 15(5):2002–2010, 2022.

[8] Jia Ling Lin and JP Wolfe. Bose-einstein condensation of paraexcitons in stressed cu 2 o. *Physical review letters*, 71(8):1222, 1993.

[9] David Snoke and GM Kavoulakis. Bose–einstein condensation of excitons in cu2o: progress over 30 years. *Reports on Progress in Physics*, 77(11):116501, 2014.

[10] Iacopo Carusotto and Cristiano Ciuti. Quantum fluids of light. *Reviews of Modern Physics*, 85(1):299–366, 2013.

[11] Ofer Firstenberg, Charles S Adams, and Sebastian Hofferberth. Nonlinear quantum optics mediated by rydberg interactions. *Journal of Physics B: Atomic, Molecular and Optical Physics*, 49(15):152003, 2016.

[12] Darrick E Chang, Vladan Vuletić, and Mikhail D Lukin. Quantum nonlinear optics–photon by photon. *Nature Photonics*, 8(9):685–694, 2014.

[13] Mikhail D Lukin, Michael Fleischhauer, Robin Cote, LuMing Duan, Dieter Jaksch, J Ignacio Cirac, and Peter Zoller. Dipole blockade and quantum information processing in mesoscopic atomic ensembles. *Physical review letters*, 87(3):037901, 2001.

[14] Valentin Walther, Robert Johne, and Thomas Pohl. Giant optical nonlinearities from rydberg excitons in semiconductor microcavities. *Nature communications*, 9(1):1309, 2018.

[15] J Heckötter, M Aßmann, and M Bayer. Rydberg excitons and quantum sensing. *MRS Bulletin*, 49(9):948–957, 2024.

[16] Callum Murray and Thomas Pohl. Quantum and nonlinear optics in strongly interacting atomic ensembles. In *Advances in Atomic, Molecular, and Optical Physics*, volume 65, pages 321–372. Elsevier, 2016.

[17] Lucy A. Downes, Andrew R. MacKellar, Daniel J. Whiting, Cyril Bourgenot, Charles S. Adams, and Kevin J. Weatherill. Full-field terahertz imaging at kilohertz frame rates using atomic vapor. *Phys. Rev. X*, 10:011027, Feb 2020.

[18] Christopher G Wade, Nikola Šibalić, Natalia R De Melo, Jorge M Kondo, Charles S Adams, and Kevin J Weatherill. Real-time near-field terahertz imaging with atomic optical fluorescence. *Nature Photonics*, 11(1):40–43, 2017.

[19] Jonathon A Sedlacek, Arne Schwettmann, Harald Kübler, Robert Löw, Tilman Pfau, and James P Shaffer. Microwave electrometry with rydberg atoms in a vapour cell using bright atomic resonances. *Nature physics*, 8(11):819–824, 2012.

[20] Michael Fleischhauer, Atac Imamoglu, and Jonathan P Marangos. Electromagnetically induced transparency: Optics in coherent media. *Reviews of modern physics*, 77(2):633–673, 2005.

[21] Masakazu Hayashi and Kiichiro Katsuki. Absorption spectrum of cuprous oxide. *Journal of the Physical Society of Japan*, 5(5):380B–381, 1950.

[22] Masakazu Hayashi and Kiichirô Katsuki. Hydrogen-like absorption spectrum of cuprous oxide. *Journal of the Physical Society of Japan*, 7(6):599–603, 1952.

[23] EF Gross. Optical spectrum of excitons in the crystal lattice. *Il Nuovo Cimento (1955-1965)*, 3(Suppl 4):672–701, 1956.

[24] C Weisbuch, H Benisty, and R Houdré. Overview of fundamentals and applications of electrons, excitons and photons in confined structures. *Journal of Luminescence*, 85(4):271–293, 2000.

[25] Marijn AM Versteegh, Stephan Steinhauer, Josip Bajo, Thomas Lettner, Ariadna Soro, Alena Romanova, Samuel Gyger, Lucas Schweickert, André Mysyrowicz, and Val Zwiller. Giant rydberg excitons in cu 2 o probed by photoluminescence excitation spectroscopy. *Physical Review B*, 104(24):245206, 2021.

[26] Annika Konzelmann, Bettina Frank, and Harald Giessen. Quantum confined rydberg excitons in reduced dimensions. *Journal of Physics B: Atomic, Molecular and Optical Physics*, 53(2):024001, 2019.

[27] Anindya Sundar Paul, Sai Kiran Rajendran, David Ziemkiewicz, Thomas Volz, and Hamid Ohadi. Local tuning of rydberg exciton energies in nanofabricated cu2o pillars. *Communications Materials*, 5(1):43, 2024.

[28] Konstantinos Orfanakis, Sai Kiran Rajendran, Hamid Ohadi, Sylwia Zielińska-Raczyńska, Gerard Czajkowski, Karol Karpiński, and David Ziemkiewicz. Quantum confined rydberg excitons in cu 2 o nanoparticles. *Physical Review B*, 103(24):245426, 2021.

[29] Min Young Lee, Soo-Hyun Kim, and Il-Kyu Park. Cu2o quantum dots emitting visible light grown by atomic layer deposition. *Physica B: Condensed Matter*, 500:4–8, 2016.

[30] Stephan Steinhauer, Marijn AM Versteegh, Samuel Gyger, Ali W Elshaari, Birgit Kunert, André Mysyrowicz, and Val Zwiller. Rydberg excitons in cu2o microcrystals grown on a silicon platform. *Communications Materials*, 1(1):11, 2020.

[31] Jingnan Cai, Yasuhiko Ishikawa, and Kazumi Wada. Strain induced bandgap and refractive index variation of silicon. *Optics express*, 21(6):7162–7170, 2013.

[32] Liangliang Yang, Jiangtao Wei, Zhe Ma, Peishuai Song, Jing Ma, Yongqiang Zhao, Zhen Huang, Mingliang Zhang, Fuhua Yang, and Xiaodong Wang. The fabrication of micro/nano structures by laser machining. *Nanomaterials*, 9(12):1789, 2019.

[33] TV Kononenko, Matthias Meier, MS Komlenok, SM Pimenov, Valerio Romano, VP Pashinin, and VI Konov. Microstructuring of diamond bulk by ir femtosecond laser pulses. *Applied Physics A*, 90:645–651, 2008.

[34] Rafael R Gattass and Eric Mazur. Femtosecond laser micromachining in transparent materials. *Nature photonics*, 2(4):219–225, 2008.

[35] Narendra B Dahotre and Sandip Harimkar. *Laser fabrication and machining of materials*. Springer Science & Business Media, 2008.

[36] Lionel Sudrie, M Franco, Bernard Prade, and André Mysyrowicz. Study of damage in fused silica induced by ultra-short ir laser pulses. *Optics Communications*, 191(3-6):333–339, 2001.

[37] Lionel Sudrie, Arnaud Couairon, Michel Franco, Brigitte Lamouroux, Bernard Prade, Stellios Tzortzakis, and André Mysyrowicz. Femtosecond laser-induced damage and filamentary propagation in fused silica. *Physical Review Letters*, 89(18):186601, 2002.

[38] Yasuhiko Shimotsuma, Peter G Kazansky, Jiarong Qiu, and Kazuoki Hirao. Self-organized nanogratings in glass irradiated by ultrashort light pulses. *Physical review letters*, 91(24):247405, 2003.

[39] Xiaozhu Xie, Caixia Zhou, Xin Wei, Wei Hu, and Qinglei Ren. Laser machining of transparent brittle materials: from machining strategies to applications. *Opto-Electronic Advances*, 2(1):180017–1, 2019.

[40] Takayuki Ito, Hiroyuki Yamaguchi, Katsuya Okabe, and Taizo Masumi. Single-crystal growth and characterization of cu2o and cuo. *Journal of materials science*, 33:3555–3566, 1998.

[41] Stephen A Lynch, Chris Hodges, Soumen Mandal, Wolfgang Langbein, Ravi P Singh, Liam AP Gallagher, Jon D Pritchett, Danielle Pizzey, Joshua P Rogers, Charles S Adams, et al. Rydberg excitons in synthetic cuprous oxide cu 2 o. *Physical Review Materials*, 5(8):084602, 2021.

[42] Bruno K. Meyer, Angelika Polity, Daniel Reppin, Martin Becker, Philipp Hering, Benedikt Kramm, Peter J. Klar, Thomas Sander, Christian Reindl, Christian Heiliger, Markus Heinemann, Christian Müller, and Carsten Ronning. Chapter six - the physics of copper oxide (cu2o). In Bengt G. Svensson, Stephen J. Pearton, and Chennupati Jagadish, editors, *Oxide Semiconductors*, volume 88 of *Semiconductors and Semimetals*, pages 201–226. Elsevier, 2013.

[43] Jacob DeLange, Kinjol Barua, Val Zwiller, Stephan Steinhauer, and Hadiseh Alaeian. Highly-excited rydberg excitons in synthetic thin-film cuprous oxide, 2022.

[44] Marc Aßmann and Manfred Bayer. Semiconductor rydberg physics. *Advanced Quantum Technologies*, 3(11):1900134, 2020.

[45] Joshua P Rogers, Liam AP Gallagher, Danielle Pizzey, Jon D Pritchett, Charles S Adams, Matthew PA Jones, Chris Hodges, Wolfgang Langbein, and Stephen A Lynch. High-resolution nanosecond spectroscopy of even-parity rydberg excitons in cu 2 o. *Physical Review B*, 105(11):115206, 2022.

[46] M Jörger, T Fleck, C Klingshirn, and R Von Baltz. Midinfrared properties of cuprous oxide: High-order lattice vibrations and intraexcitonic transitions of the 1 s paraexciton. *Physical Review B-Condensed Matter and Materials Physics*, 71(23):235210, 2005.

[47] JW Hodby, TE Jenkins, Cl Schwab, H Tamura, and D Trivich. Cyclotron resonance of electrons and of holes in cuprous oxide, cu2o. *Journal of Physics C: Solid State Physics*, 9(8):1429, 1976.

[48] Michael O'Keeffe. Infrared optical properties of cuprous oxide. *The Journal of Chemical Physics*, 39(7):1789–1793, 1963.

[49] C Carabatos, A Diffiné, and M Sieskind. Contribution à l'étude des bandes fondamentales de vibration du réseau de la cuprite (cu2o). *Journal de Physique*, 29(5-6):529–533, 1968.

[50] T González Sánchez, JE Velazquez Perez, PM Gutierrez Conde, and D Pardo Collantes. Five-valley model for the study of electron transport properties at very high electric fields in gaas. *Semiconductor science and technology*, 6(9):862, 1991.

[51] K Saito, M Hasuo, T Hatano, and N Nagasawa. Band gap energy and binding energies of z3-excitions in cucl. *Solid state communications*, 94(1):33–35, 1995.

[52] A Jolk and CF Klingshirn. Linear and nonlinear excitonic absorption and photoluminescence spectra in cu2o: line shape analysis and exciton drift. *physica status solidi (b)*, 206(2):841–850, 1998.

[53] Florian Schöne, Heinrich Stolz, and Nobuko Naka. Phonon-assisted absorption of excitons in cu 2 o. *Physical Review B*, 96(11):115207, 2017.

[54] T Sander, CT Reindl, M Giar, B Eifert, M Heinemann, C Heiliger, and PJ Klar. Correlation of intrinsic point defects and the raman modes of cuprous oxide. *Physical Review B*, 90(4):045203, 2014.

[55] Thomas Sander, Christian T Reindl, and Peter J Klar. Breaking of raman selection rules in cu2o by intrinsic point defects. *MRS Online Proceedings Library (OPL)*, 1633:81–86, 2014.

[56] Marcel Giar, Markus Heinemann, and Christian Heiliger. Phonon properties of copper oxide phases from first principles. *Physical Review B*, 96(7):075202, 2017.

[57] Klaus-Peter Bohnen, Rolf Heid, Lothar Pintschovius, Aloysius Soon, and Catherine Stampfl. Ab initio lattice dynamics and thermal expansion of cu 2 o. *Physical Review B - Condensed Matter and Materials Physics*, 80(13):134304, 2009.

[58] Barbara Lafuente, Robert T Downs, Hexiong Yang, Nate Stone, Thomas Armbruster, Rosa Micaela Danisi, et al. The power of databases: the rruff project. *Highlights in mineralogical crystallography*, 1:25, 2015.

[59] A Compaan and HZ Cummins. Raman scattering, luminescence, and exciton-phonon coupling in cu 2 o. *Physical Review B*, 6(12):4753, 1972.

[60] MM Beg and SM Shapiro. Study of phonon dispersion relations in cuprous oxide by inelastic neutron scattering. *Physical Review B*, 13(4):1728, 1976.

[61] J Reydellet, M Balkanski, and D Trivich. Light scattering and infrared absorption in cuprous oxide. *physica status solidi (b)*, 52(1):175–185, 1972.

[62] Costantino Corbari, Audrey Champion, Mindaugas Gecevičius, Martynas Beresna, Yves Bellouard, and Peter G Kazansky. Femtosecond versus picosecond laser machining of nano-gratings and micro-channels in silica glass. *Optics Express*, 21(4):3946–3958, 2013.

[63] Stellios Tzortzakis, Lionel Sudrie, Michel Franco, Bernard Prade, André Mysyrowicz, Arnaud Couairon, and Luc Bergé. Self-guided propagation of ultrashort ir laser pulses in fused silica. *Physical review letters*, 87(21):213902, 2001.

[64] BC Stuart, MD Feit, AM Rubenchik, BW Shore, and MD Perry. Laser-induced damage in dielectrics with nanosecond to subpicosecond pulses. *Physical review letters*, 74(12):2248, 1995.

[65] X Liu, D Du, and Gé Mourou. Laser ablation and micromachining with ultrashort laser pulses. *IEEE journal of quantum electronics*, 33(10):1706–1716, 1997.

[66] Saulius Juodkazis, Hiroaki Misawa, and Igor Maksimov. Thermal accumulation effect in three-dimensional recording by picosecond pulses. *Applied Physics Letters*, 85(22):5239–5241, 2004.

[67] Arnaud Couairon and André Mysyrowicz. Femtosecond filamentation in transparent media. *Physics reports*, 441(2-4):47–189, 2007.

[68] Eli Yablonovitch and N Bloembergen. Avalanche ionization and the limiting diameter of filaments induced by light pulses in transparent media. *Physical Review Letters*, 29(14):907, 1972.

[69] Claudia Malerba, Francesco Biccari, Cristy Leonor Azanza Ricardo, Mirco D'Incau, Paolo Scardi, and Alberto Mittiga. Absorption coefficient of bulk and thin film cu2o. *Solar energy materials and solar cells*, 95(10):2848–2854, 2011.

[70] J Serna, E Rueda, and H García. Nonlinear optical properties of bulk cuprous oxide using single beam z-scan at 790 nm. *Applied Physics Letters*, 105(19), 2014.

[71] Liam AP Gallagher, Joshua P Rogers, Jon D Pritchett, Rajan A Mistry, Danielle Pizzey, Charles S Adams, Matthew PA Jones, Peter Grünwald, Valentin Walther, Chris Hodges, et al. Microwave-optical coupling via rydberg excitons in cuprous oxide. *Physical Review Research*, 4(1):013031, 2022.

[72] Julian Heckötter, Valentin Walther, Stefan Scheel, Manfred Bayer, Thomas Pohl, and Marc Aßmann. Asymmetric rydberg blockade of giant excitons in cuprous oxide. *Nature communications*, 12(1):3556, 2021.

[73] Ugo Fano. Effects of configuration interaction on intensities and phase shifts. *Physical review*, 124(6):1866, 1961.

[74] Yutaka Toyozawa. Interband effect of lattice vibrations in the exciton absorption spectra. *Journal of Physics and Chemistry of Solids*, 25(1):59–71, 1964.

[75] G Dasbach, D Fröhlich, R Klieber, D Suter, M Bayer, and H Stolz. Wave-vector-dependent exchange interaction and its relevance for the effective exciton mass in cu 2 o. *Physical Review B - Condesnsed Matter and Material Physics*, 70(4):045206, 2004.

[76] HORIBA Scientific, Kyoto Close - Moulton Park, NN3 6FL. *LabRAM HR Evolution User Manual*, 2019.

[77] HORIBA Scientific, Kyoto Close - Moulton Park, NN3 6FL. *LabSpec 6 Spectroscopy Suite Reference Manual*, 2019.

[78] X Mathew, NR Mathews, and PJ Sebastian. Temperature dependence of the optical transitions in electrodeposited cu2o thin films. *Solar energy materials and solar cells*, 70(3):277–286, 2001.

[79] Francesco Masia, Arnica Karuna, Paola Borri, and Wolfgang Langbein. Hyperspectral image analysis for cars, srs, and raman data. *Journal of raman spectroscopy*, 46(8):727–734, 2015.

[80] Francesco Masia, Adam Glen, Phil Stephens, Paola Borri, and Wolfgang Langbein. Quantitative chemical imaging and unsupervised analysis using hyperspectral coherent anti-stokes raman scattering microscopy. *Analytical Chemistry*, 85(22):10820–10828, 2013.

[81] Koichi Kanaya, Susumu Ono, and Fumiko Ishigaki. Secondary electron emission from insulators. *Journal of Physics D: Applied Physics*, 11(17):2425, 1978.

[82] A Hussain, LH Yang, YB Zou, SF Mao, B Da, HM Li, and ZJ Ding. Theoretical calculations of the mean escape depth of secondary electron emission from compound semiconductor materials. *Journal of Applied Physics*, 127(12), 2020.

[83] CI McPhee, G Zoriniants, W Langbein, and Paola Borri. Measuring the lamellarity of giant lipid vesicles with differential interference contrast microscopy. *Biophysical journal*, 105(6):1414–1420, 2013.

[84] Samuel Hamilton, David Regan, Lukas Payne, Wolfgang Langbein, and Paola Borri. Sizing individual dielectric nanoparticles with quantitative

differential interference contrast microscopy. *Analyst*, 147(8):1567–1580, 2022.

[85] David Regan, Joseph Williams, Paola Borri, and Wolfgang Langbein. Lipid bilayer thickness measured by quantitative dic reveals phase transitions and effects of substrate hydrophilicity. *Langmuir*, 35(43):13805–13814, 2019. PMID: 31483674.

[86] Timothy Ostler, Wolfgang Langbein, Paola Borri, Emily Lewis, Yisu Wang, Karl Swann, Thomas E Woolley, and Katerina Kaouri. Differential dynamic microscopy can be applied to differential interference contrast images despite shadowing effects. *arXiv preprint arXiv:2212.11827*, 2022.

[87] LIAM GALLAGHER and PATRICK ANDREW. *Optical and microwave spectroscopy of Rydberg excitons in Cu _2 O*. PhD thesis, Durham University, 2022.

[88] B Lefez, K Kartouni, M Lenglet, Daniel Rönnow, and CG Ribbing. Application of reflectance spectrophotometry to the study of copper (i) oxides (cu2o and cu3o2) on metallic substrate. *Surface and interface analysis*, 22(1-12):451–455, 1994.

[89] Robert Schennach and Andreas Gupper. Copper oxidation studied by in situ raman spectroscopy. *MRS Online Proceedings Library (OPL)*, 766:E3–2, 2003.

[90] W M Haynes, editor. *CRC Handbook of Chemistry and Physics*. Taylor and Francis Group, 6000 Broken Sound Parkway NW, Suite 300, Boca Raton, FL, 2014.

[91] Mitsuyoshi Takahata and Nobuko Naka. Photoluminescence properties of the entire excitonic series in cu 2 o. *Physical Review B*, 98(19):195205, 2018.

Appendix A

Chemical Etching

Laser machining was found to preferentially affect the surfaces of the samples even when the laser was focused in the middle. One possible explanation for this was that the surface of the sample contained a greater concentration of defects which were more absorbing - specifically, this was thought to be an oxidation to cupric oxide (CuO). Chemically etching the sample surfaces could remove this (oxidised) layer. The procedure for this was developed in advance of machining on the natural sample AL01. High-quality natural samples such as this are valuable in research so two other samples, AH and AF01, were tested before etching was carried out on AL01.

The etching procedure used was taken from Takahata and Naka [91] and involved immersion in 2 M HCl for 10 s followed by 13 M aqueous NH_3 for 10 s. Immersion in a reservoir of deionised water after the NH_3 was added to procedure also. The samples used by Takahata and Naka were around 10× thicker than AL01 and presumably larger in their other dimensions too and immersion in the chemicals for AL01 would not be straightforward. The solution for this was to use 3D-printed, chlorinated polyethylene (CPE) cages with small holes in them to house the sample to be etched (see Fig. A.1). The entire cage could then be submerged in the chemicals by holding onto it with plastic tweezers so that the chemicals flow through the holes in order to expose the sample inside to the them without applying such a force to it that may damage it. The entire procedure was performed in a fume cupboard.

AH was tested first. The purpose of this was to ensure that the reaction between Cu_2O and HCl would not be a violent one. It was etched in HCl and no violent reaction was observed, so it was immediately rinsed in the DI water reservoir. Images of AH before and after etching are shown in Fig. A.2. The sample surface appeared to remain smooth, although it did taken on a silvery colour. The synthetic sample AF01 was tested next. This had much more similar dimensions to AL01 and the exact procedure to be used with AL01 was followed for it. Images before and after etching are shown in Fig. A.3. In this case, the surface of the sample became very rough. Black spots seen on the surface are believed to be inclusions that were previously inside the sample now brought to the surface by the removal of material. Due to the roughness there was a lot more scattering at the surface and much less light

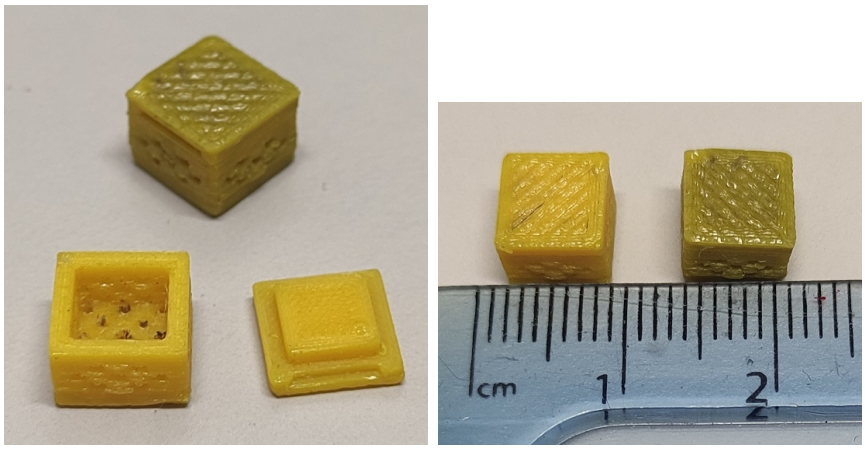

Figure A.1: Images of CPE cages that were 3D-printed to hold the samples during etching.

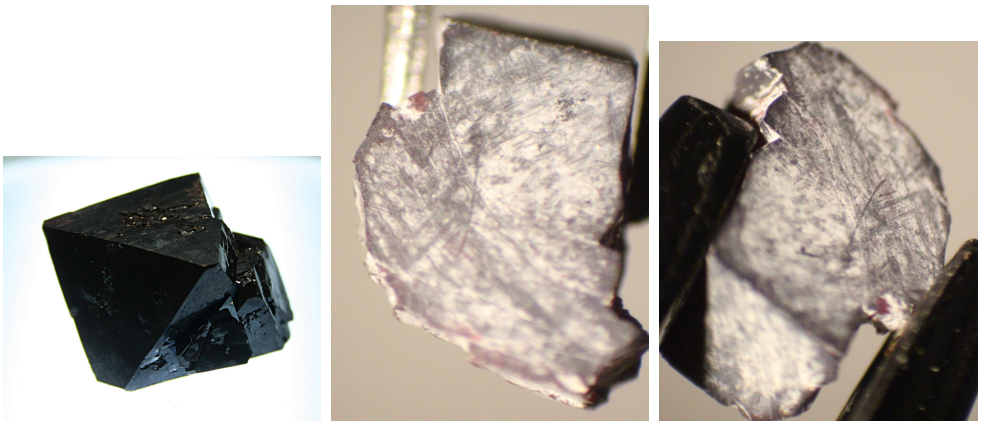

Figure A.2: A photograph of the sample AH before submersion in HCl, and two photographs of it afterwards.

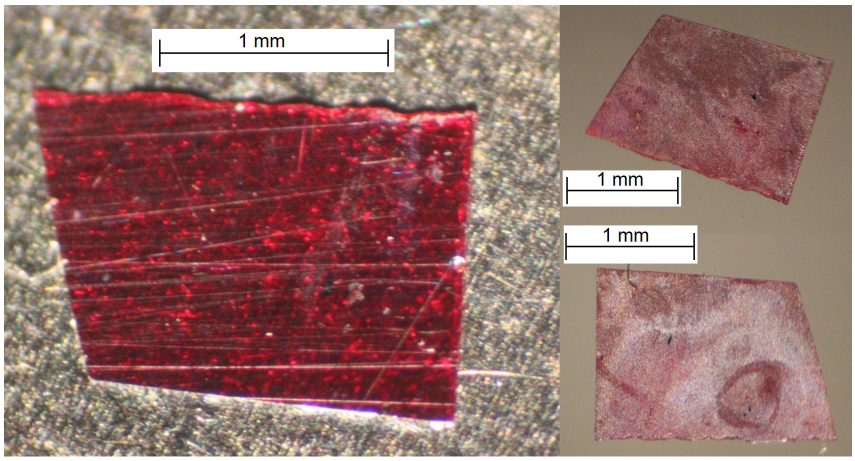

Figure A.3: A photograph AF01 before chemical etching (left) and two of it afterwards, one of each surface (right).

was transmitted through the sample compared to before it was etched. Finally, the procedure was carried out for AL01 but this resulted in no clear visible effect. Furthermore, when it underwent laser machining shortly after this, no significant change in ease or difficulty in machining was observed. Images of AL01 alongside un-etched samples are shown in Fig. A.4. The smallest fragment here is also from AL01 (referred to as AL01b) and can be compared to AL01a (the second largest in the images). In the first image there appears to be very little difference between AL01a (the second largest fragment in the images) and AL01. In the second image, however, the surface of the etched sample appears to be much clearer than the un-etched one. However, the similarities betwen AL01a and AL01b in the first image suggest that the difference seen in the second image could be due to a tilt in on of the samples or perhaps features on the CaF_2 windows. The clarity of AL01a in the second image is comparable to that of AM01 suggesting that even if the etching did improve the sample surface, this improvement is no better than what can be achieved with standard cleaning and polishing. Compared to AF01, the visible effect of etching AL01, if any, was far less

The two main differences between AF01 and AL01 are that AF01 is a synthetic sample and AL01 is natural, and that AL01 is oriented in the (111) crystal direction. Niu et al. [7] investigated the effects of concentrated ammonia etching on cuprous oxide, including for different crystal orientations. They found that for etching of a surface with (111) orientation, the surface remained mostly flat and etching was much less effective. In fact, of all of the orientations tried, surfaces with (111) showed th smallest effect due to etching. An effect was seen nonetheless, though ammonia exposure times used by Niu et al. were significantly longer - up to 1 hour.

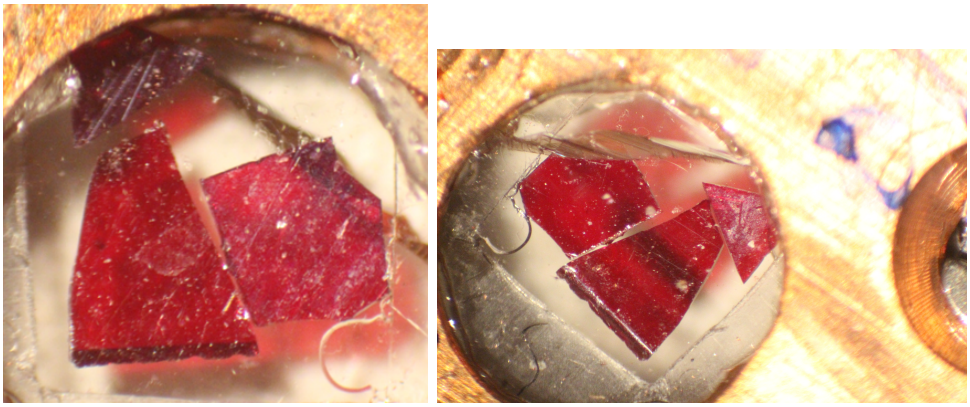

Figure A.4: Photographs of AL01 and AM01 after AL01 had been etched. In order of size the fragments are AM01, AL01a, and AL01b. AL01a was the etched fragment.

Appendix B

Exciton Peak Fits

Spatial resolution in y-direction for all maps included was 1.16 µm/pixel. The x-resolution scans of sites A, B, and C was 0.900 µm/pixel, 0.548 µm/pixel, and 0.861 µm/pixel respectively. Scans at the 1s-orthoexciton range covered a slightly different distance in the x-direction. The spatial resolution of the resulting maps was 0.613 µm/pixel for AF00/B, 1.269 µm/pixel for AG15, and 2.129 µm/pixel for AF00/X. Errors associated with the fit parameters were calculated using the spread of data in a homogeneous region of the map and are given for all peaks in Table B.1.

		Errors				
Site	Peak	O	ν_0/µeV	Γ/µeV	A	δ_L
AF00/A	$n = 3$	0.02	4	12	0.04	4×10^{-3}
	$n = 4$	0.05	3	14	0.11	0.012
	$n = 5$	0.05	4	12	0.14	0.012
	$n = 6$	0.04	5	12	0.14	0.03
AF00/B	$n = 3$	0.03	3	9	0.04	3×10^{-3}
	ortho	0.04	0.4	2	6×10^{-3}	n/a
AF00/C	$n = 3$	0.02	3	9	0.04	3×10^{-3}
AG15	ortho	0.02	1	8	8×10^{-3}	n/a
AF00/X	ortho	0.06	0.7	0.4	7×10^{-3}	n/a

Table B.1: Errors associated with all of the fit parameters for all of the exciton absorption peak fits calculated using the spread of data in homogeneous regions of the maps. Note that there is no δ_L parameter for the orthoexciton fits since symmetrical Lorentzian curves were using to model these absorption peaks.

Appendix C

Raman Spectroscopy

C.1 Metadata

This subsection contains metadata on the collection and analysis of data from confocal Raman imaging.

Scans of AG15 were performed over an area 26.3×50.4 µm covered by 11×19 points, this was 5 depths at z-intervals of 3 µm which corresponds to a depth of 8.7 µwhen accounting for the refractive index $n = 2.9$ at $\lambda = 660$ nm [69]. Each point used the following settings: acquisition time = 0.04 s, diffraction grating = 300 l/mm, wavelength range detected = 660-1000 nm, laser operated at 50% of maximum power, confocal hole size = 50 µm.

A 7 × 5 grid of points separated by 1 µm was used in the scans of AF00. The stage was moved by z-intervals of 2 µwhich corresponds to 5.8 µm. Each point used the following settings: acquisition time = 0.5 s, diffraction grating = 300 l/mm, wavelength range detected = 660-1050 nm, laser operated at 25% of maximum power, confocal hole size = 50 µm.

Metadata for FSC^3 analysis is given in Fig. C.1.

C.2 CuO impurities

Fig. C.2 shows the Raman spectra of some Cu_2O samples that were acquired prior to any laser machining while the procedure for the use of the Raman spectrometer was being developed. All three samples show activity at around 298 cm^{-1} which is not uncommon in other samples in the literature [42, 54, 55, 59]. Generally, this is attributed to the A_{2u} mode, although this mode tends to appear at around 350 cm^{-1} in some sources. The CuO Raman spectrum is also included in Fig. C.2 which is dominated by a well-defined peak at the same Raman shift. The presence of such a peak in a spectrum of Cu_2O (such as in AP00, in particular) may therefore suggest the presence of CuO impurities rather than be due to Cu_2O phonon modes.

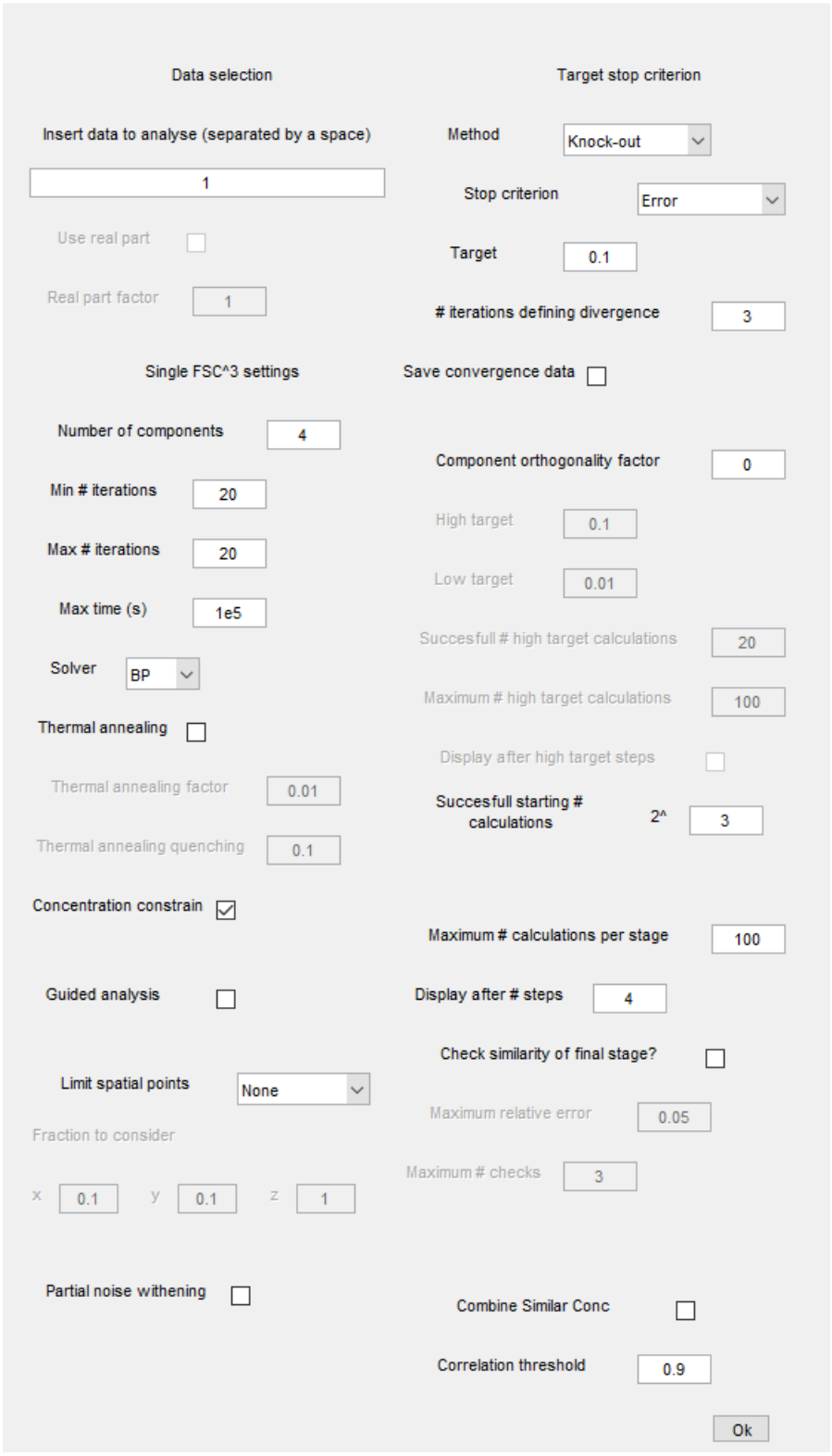

Figure C.1: Setting used for FSC_3 analysis. The number of components was altered but most data shown used 2.

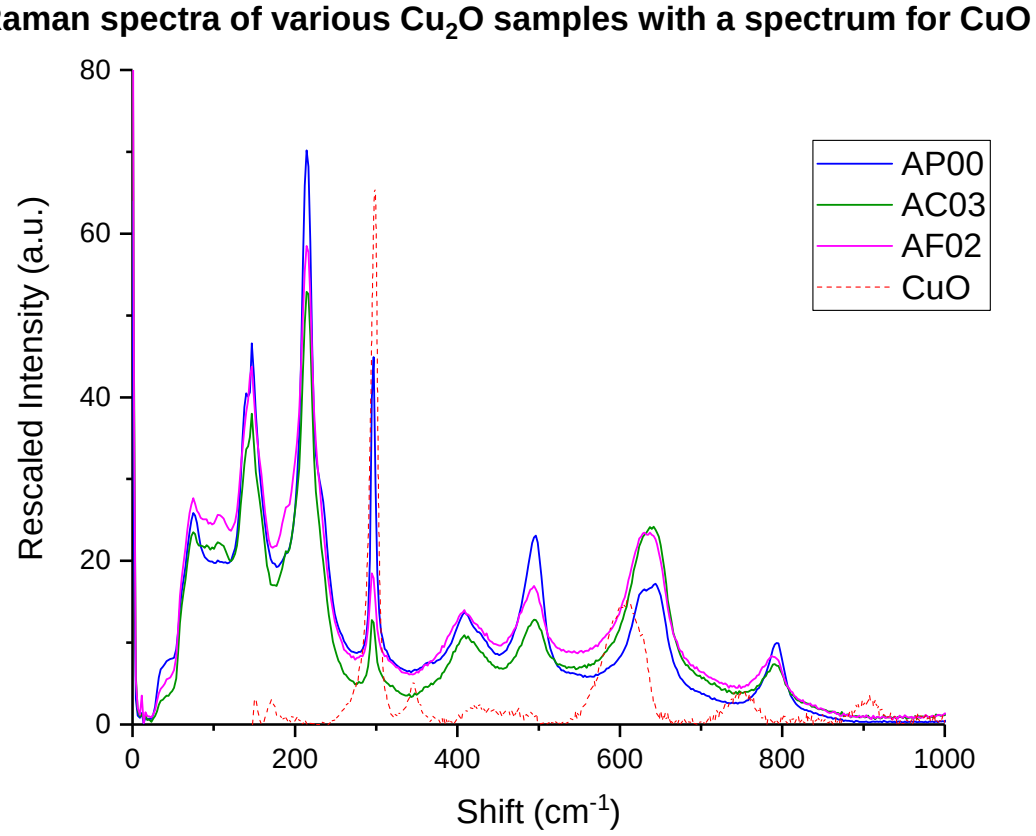

Figure C.2: Raman spectra for a collection of Cu_2O samples; AC03 is a natural sample and the other two are synthetic. Also included is a typical CuO Raman spectrum. Alignment of the dominant CuO peak suggest CuO impurities in the Cu_2O samples.

Appendix D

FIB-SEM

SEM images of machinings are shown with plots of their widths with depth.

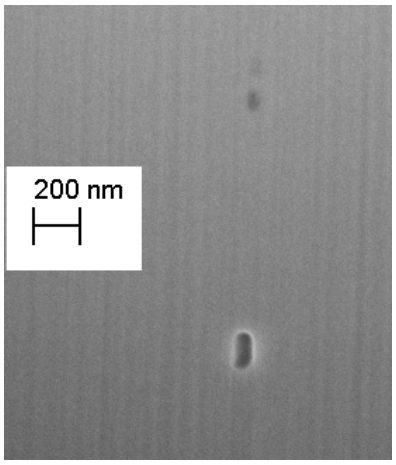

(a)

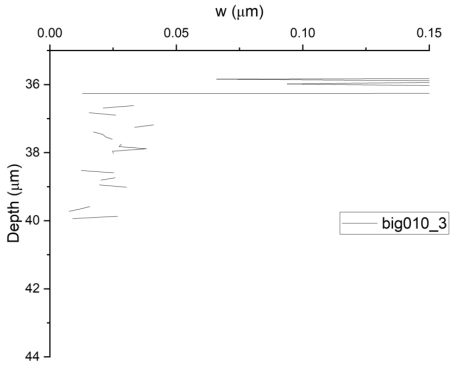

(b)

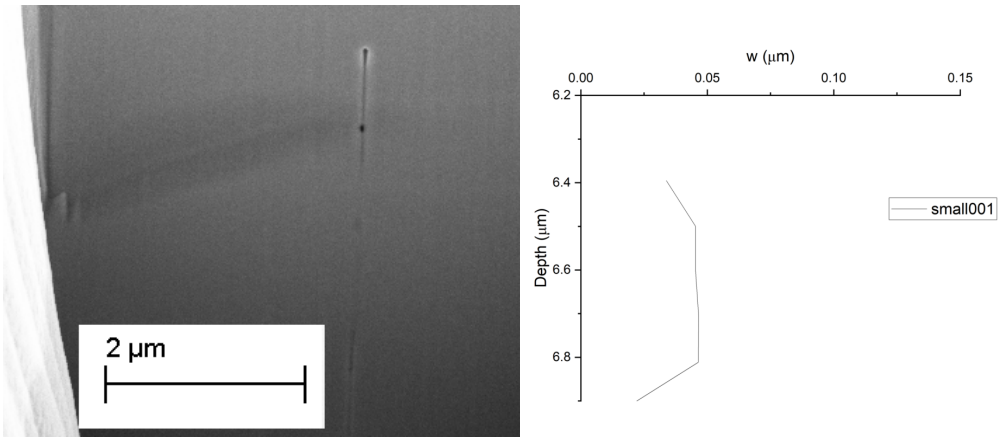
2 µm
w (µm)
0.00
0.05
0.10
0.15
6.2
6.4
6.6
6.8
Depth (µm)
small001

(a) **(b)**

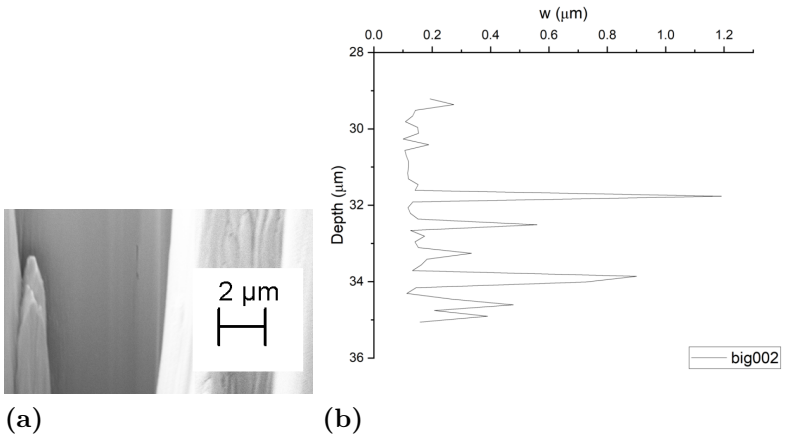
2 µm
w (µm)
0.0
0.2
0.4
0.6
0.8
1.0
1.2
28
30
32
34
36
Depth (µm)
big002

(a) **(b)**

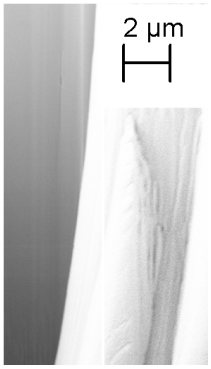
2 µm

(a)

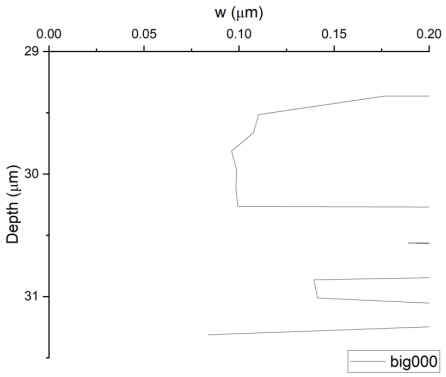
w (µm)
0.00
0.05
0.10
0.15
0.20
29
30
31
Depth (µm)
big000

(b)

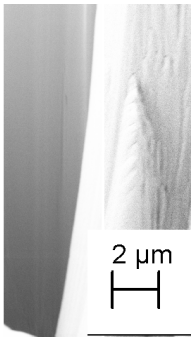
2 µm

(a)

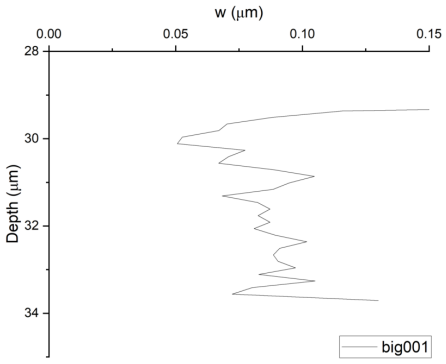
w (µm)
0.00
0.05
0.10
0.15
28
30
32
34
Depth (µm)
big001

(b)

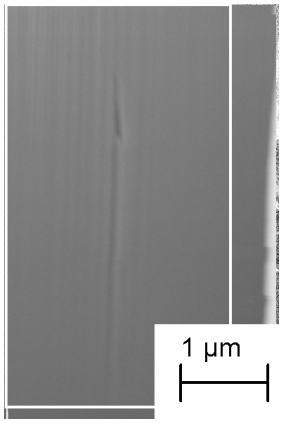
1 µm

(a)

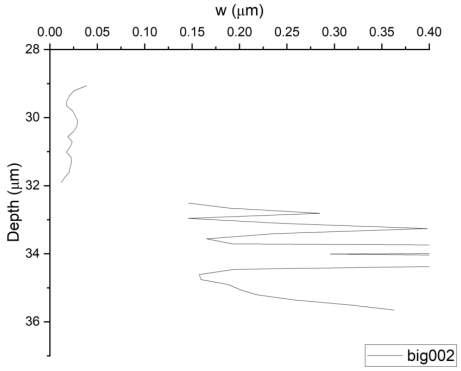
w (µm)
0.00
0.05
0.10
0.15
0.20
0.25
0.30
0.35
0.40
28
30
32
34
36
Depth (µm)
big002

(b)


2 µm

(a)

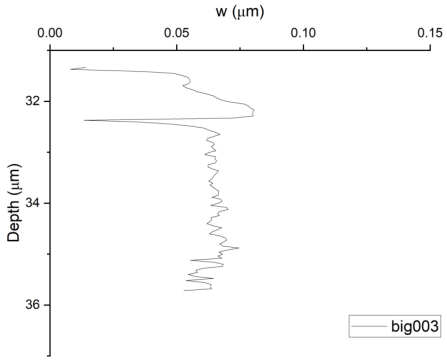
w (µm)
0.00
0.05
0.10
0.15
32
34
36
Depth (µm)
big003

(b)

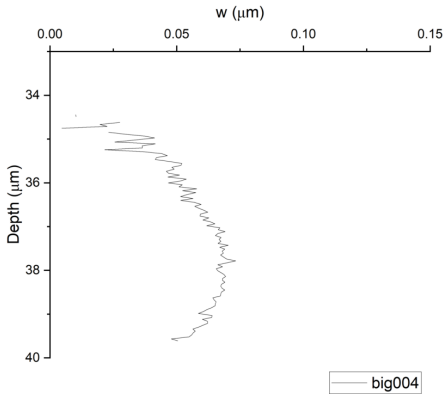
w (µm)
0.00
0.05
0.10
0.15
34
36
38
40
Depth (µm)
big004

(c)

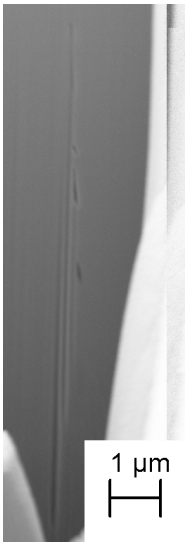
1 µm

(a)

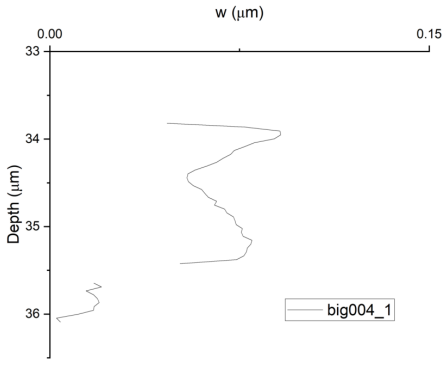
w (µm)
0.00
0.15
33
34
35
36
Depth (µm)
big004_1

(b)

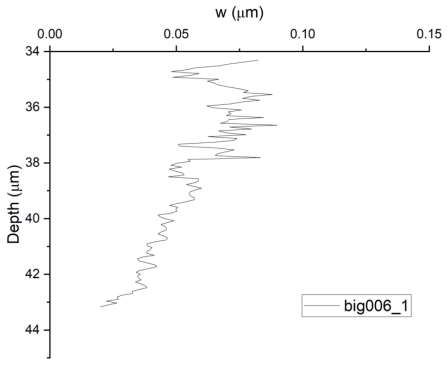
w (µm)
0.00
0.05
0.10
0.15
34
36
38
40
42
44
Depth (µm)
big006_1

(c)

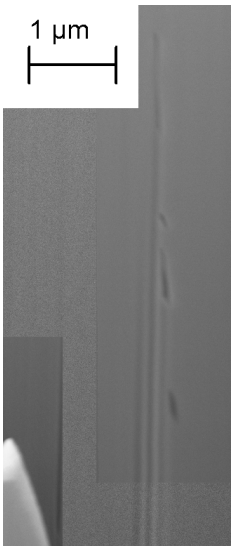
1 µm

(a)

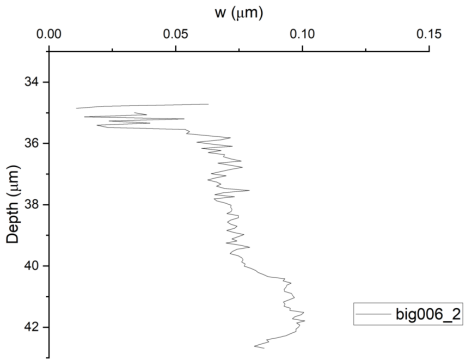
w (µm)
0.00
0.05
0.10
0.15
34
36
38
40
42
Depth (µm)
big006_2

(b)

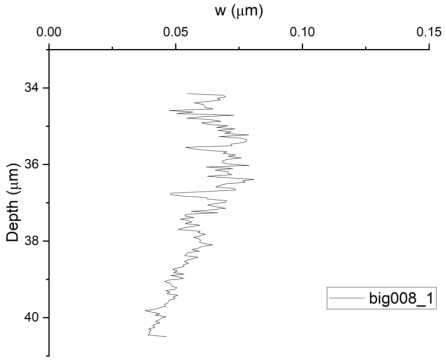
w (µm)
0.00
0.05
0.10
0.15
34
36
38
40
Depth (µm)
big008_1

(c)

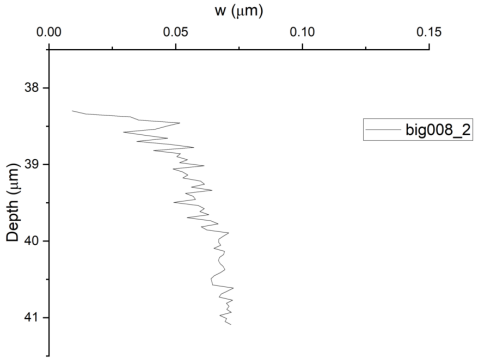
w (µm)
0.00
0.05
0.10
0.15
38
39
40
41
Depth (µm)
big008_2

(d)

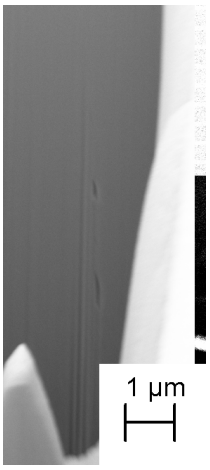
1 µm

(a)

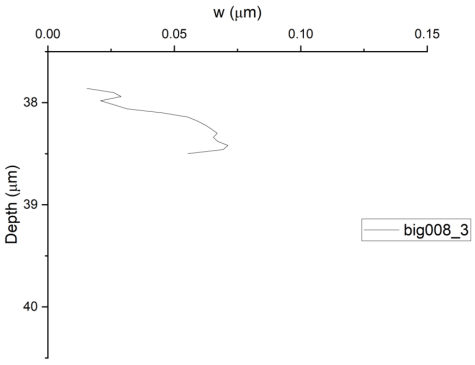
w (µm)
0.00
0.05
0.10
0.15
38
39
40
Depth (µm)
big008_3

(b)

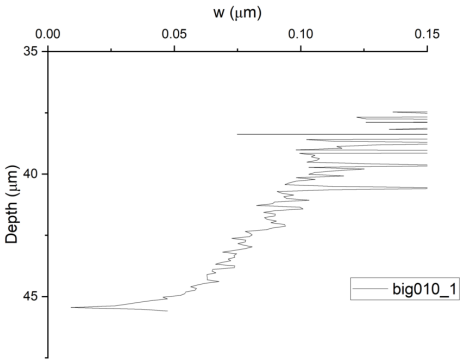
w (µm)
0.00
0.05
0.10
0.15
35
40
45
Depth (µm)
big010_1

(c)

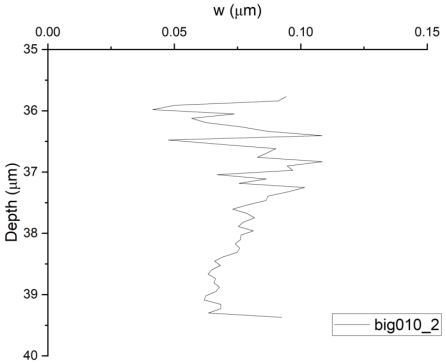
w (µm)
0.00
0.05
0.10
0.15
35
36
37
38
39
40
Depth (µm)
big010_2

(d)

Appendix E

Laser Machining Settings

The following table contains machining parameters for the machinings in samples AF00, AG15, and AF13. Samples AL01 and AM01 were also machined but analysis of these samples is limited to cross section calculations so they are not included in the table. Around 200 machinings were created in AL01 with pulse energies ranging from 0.35 to 1.7 µJ with a few additional pulses used as markers up to 3 µJ. AM01 had about 140 machinings from pulses between 0.16 to 1.5 µJ with marker shots using pulses up to 2.9 µJ.

Machining	Polarization/°	Pulse Energy (µJ)	Depth (µm)
AF00/A-1d	0	4.2	0.3
AF00/A-1e	0	1.7	-11.5
AF00/A-1g	0	23	-4.5
AF00/A-1h	0	4.2	-2.1
AF00/A-1i	0	10.4	-1.7
AF00/A-2d	0	4.2	-4.2
AF00/A-2e	0	4.2	-4.2
AF00/A-2f	0	4.2	-4.2
AF00/A-2g	0	4.2	-2.5
AF00/A-2h	0	4.2	-2.5
AF00/A-2i	0	4.2	-2.5
AF00/A-3a	0	4.2	-3.4
AF00/A-3b	0	4.2	-3.4
AF00/A-3c	0	4.2	-3.4
AF00/A-3d	0	4.2	-6.5
AF00/A-3e	0	4.2	-6.5
AF00/A-3f	0	4.2	-6.5
AF00/A-3g	0	4.2	-3.6
AF00/A-3h	0	4.2	-3.6
AF00/A-3i	0	4.2	-3.6
AF00/A-4d	0	4.2	-4.5
AF00/A-4e	0	4.2	-4.5
AF00/A-4f	0	4.2	-4.5
AF00/A-4g	0	4.2	-4
AF00/A-4h	0	4.2	-4
AF00/A-4i	0	4.2	-4

Machining	Polarization/°	Pulse Energy (µJ)	Depth (µm)
AF00/B-1a	0	2.06	-4
AF00/B-1b	0	1.94	-3.1
AF00/B-1c	0	2.15	0
AF00/B-1d	0	2.18	-1.1
AF00/B-1e	0	1.97	-0.5
AF00/B-1f	0	no data	-0.3
AF00/B-2a	0	0.84	-0.3
AF00/B-2b	0	0.81	-0.1
AF00/B-2c	0	0.92	0.1
AF00/B-2d	0	0.88	0.3
AF00/C-1a	90	2.00	-1.5
AF00/C-1b	90	2.15	-1.6
AF00/C-1c	90	2.04	-1.6
AF00/C-1d	90	1.99	-4
AF00/C-1e	90	2.17	-4
AF00/C-1f	90	2.12	-4.1
AF00/C-2a	90	1.69	0.7
AF00/C-2b	90	1.92	0.8
AF00/C-2c	90	2.04	0.8
AF00/C-2d	90	1.95	0
AF00/C-2e	0	2.15	0
AF00/C-2f	0	2.08	0.1
AF00/C-3a	0	2.22	-4.7
AF00/C-3b	0	2.22	-4.7
AF00/C-3c	0	2.19	-4.5
AF00/C-3d	0	4.63	-4.7
AF00/C-3e	0	2.73	-4.7
AF00/C-3f	0	3.05	-4.7

Machining	Polarization/°	Pulse Energy (µJ)	Depth (µm)
AG15-1c	0	4.74	15
AG15-1f	90	5.20	15
AG15-2b	90	4.65	15
AG15-2d	90	4.53	15
AG15-2e	0	4.70	15
AG15-2g	0	5.12	15
AG15-3a	0	4.97	15
AG15-3c	0	4.78	15
AG15-3f	90	4.78	15
AG15-4a	0	11.80	15
AG15-4b	0	11.42	15
AG15-4c	0	11.68	15
AG15-4d	90	11.40	15
AG15-4e	90	11.79	15
AG15-4f	90	11.86	15
AG15-5a	0	10.11	15
AG15-5b	0	10.28	15
AG15-5c	0	10.77	15
AG15-5d	0	9.89	15
AG15-5e	0	10.89	15
AG15-5f	90	10.95	15

Machining	Polarization/°	Pulse Energy (µJ)	Depth (µm)
AF13-1g	90	1.76	-11
AF13-1h	90	1.89	-11
AF13-1i	90	1.83	-11
AF13-1j	90	1.25	-11
AF13-1k	90	1.31	-11
AF13-1l	90	1.17	-11
AF13-1m	90	3.14	-13
AF13-2a	90	1.32	11
AF13-2b	90	1.28	9
AF13-2c	90	1.38	7
AF13-2d	90	1.3	5
AF13-2e	90	1.11	3
AF13-2f	90	1.18	1
AF13-2g	90	1.06	-1
AF13-2h	90	1.24	-3
AF13-2i	90	1.13	-5
AF13-2j	90	1.10	-7
AF13-2k	90	1.20	-9
AF13-2l	90	1.23	-11
AF13-3b	90	0.92	5
AF13-3c	90	0.90	5
AF13-3d	90	0.89	5
AF13-3e	90	1.07	5
AF13-3f	90	1.15	5
AF13-3g	90	1.04	5
AF13-3h	90	1.15	5
AF13-3i	90	1.20	5
AF13-3j	90	1.01	4
AF13-3k	90	0.97	-3
AF13-3l	90	High	-3
AF13-3m	90	1.27	0

Table E.1: Parameters used in laser machining for the machinings shown in all analysis except cross-section calculations.

Appendix F

Oscillator Strengths

Maps of relative oscillator strength changes due to the machining were calculated from the absorption (in turn calculated as $\log 1/T$ where T is the transmission) peak fits by multiplying the amplitudes (A) and full width half maxima (Γ). The results are maps of the machining sites on AF00 where the greyscale represents the relative oscillator strength of each peak. The oscillator strengths without machining were obtained from the background of these images (referred to as background oscillator strength) and the range of the greyscale was determined by this value where black and white represent a reduction of 20% and an increase of 10% of this background value, respectively. This is shown in Fig F.1.

For site AF00/A, most machinings showed a decrease in oscillator strength due to laser machining suggesting that strain-shifted resonances alone are not responsible for the decrease in amplitude of the absorption peaks. However, for sites AF00/B and C, for peaks $n > 3$, and indeed some machinings in at AF00/A, there is little-to-no change in oscillator strength due to machining meaning that the decrease in amplitude is fully accounted for by a commensurate broadening of the peak due to strain-induced shifts in resonance.

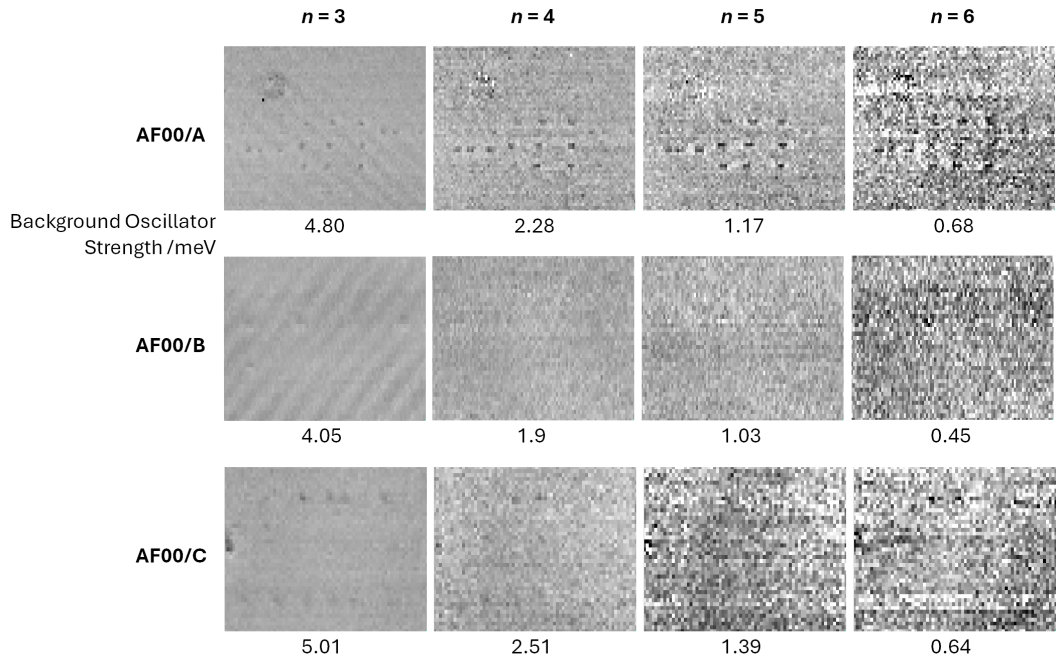

Figure F.1: The relative change of oscillator strengths of the Rydberg peaks $n = 3$ to 6. The ranges in each map are from -20% to +10% of the background value of the relative oscillator strength given underneath each map.